Electron and Nuclear Spin Dynamics and Coupling in InGaAs

by

Christopher J. Trowbridge

A dissertation submitted in partial fulfillment
of the requirements for the degree of
Doctor of Philosophy
(Applied Physics)
in The University of Michigan
2015

Doctoral Committee:

Associate Professor Vanessa Sih, Chair
Assistant Professor Hui Deng
Professor Rachel S. Goldman
Professor Cagliyan Kurdak
Professor Duncan G. Steel

TABLE OF CONTENTS

LIST OF FIGURES

Figure

LIST OF TABLES

Table

ABSTRACT

Electron and Nuclear Spin Dynamics and Coupling in InGaAs

by

Christopher J. Trowbridge

Chair: Vanessa Sih

The profound economic, societal, and scientific advances that have accompanied the development of electronic devices for the processing and transmission of information provide a compelling interest in advancing the state of the art in these fields. Presently, fundamental limits on the miniaturization of integrated circuit components are being approached, motivating a search for fundamentally new techniques for continued improvement. Devices which take advantage of electron spin – commonly known as spintronics devices – may provide a way forward. This dissertation focuses on the development of an understanding of electron spin transport, dynamics, and coupling to the nuclear spin system in gallium arsenide (GaAs), as well as the measurement techniques brought to bear in their investigation.

Current-induced electron spin polarization is shown to produce nuclear hyperpolarization through dynamic nuclear polarization. Saturated nuclear magnetic fields of several millitesla are generated upon the application of electric field over a timescale of minutes in indium gallium arsenide (InGaAs) epilayers and measured using optical Larmor magnetometry. We show that, in contrast to previous demonstrations of current-induced dynamic nuclear polarization, the direction of the current relative to the crystal axes and external magnetic field allows for control over the magnitude and direction of the saturation nuclear field. An

asymmetry in saturated nuclear magnetic field for anti-parallel currents is found, and ascribed to competing electron spin alignment mechanisms which lead to nuclear polarization which is current-direction independent. The behavior of the saturated nuclear field with temperature, electric field strength, and external magnetic field strength is measured. An unexpected asymmetry in measurements of the change in nuclear field from polarization and depolarization transitions is found and determined to be the result of an unexpected phase shift in Larmor magnetometric measurements due to previous pulses. Implications for the measurements of nuclear magnetic fields resulting from the phase shift are discussed.

Time-resolved Faraday rotation (TRFR) measurements, which have proved transformative in the investigation of spin dynamics in semiconductors, are used to study nuclear polarization. We find that, in materials with spin lifetimes which are on the order of, or greater than, the laser repetition time, the collective effect of spin polarization due to the whole pump pulse train becomes important. A relative phase shift in TRFR measurements is identified which results from these spins. A closed-form expression which describes this phase shift is derived and experimentally validated. Numerical methods are used to characterize this phase shift throughout parameter space. A spin lifetime measurement based on this phase shift is described, and situations in which the model used must be augmented are discussed.

CHAPTER I

Introduction, motivation, and organization

Since the development of the transistor in the 1940's and '50s, semiconductor devices have come to dominate electronics. The development of the integrated circuit in the late '50s paved the way for the development of computers based on solid state circuits. Since then, computers have advanced at an astounding rate. This rapid advancement has played a large part in driving the global economy, sparked a social revolution, and changed the way we communicate, store, and access information. Relatively inexpensive and fast computers have also lead to a paradigm shift in how science is done. Computer modeling and simulations allow us a glimpse at the solutions to problems that are analytically intractable, and have made possible experiments that require the generation and analysis of vast quantities of data, such as high energy particle physics experiments and astronomical observations.

In 1965, Intel co-founder Gordon Moore posited in an article written for Electronics Magazine that the number of components on an integrated circuit was on pace to roughly double every 18 months. 'Moore's law', as it was dubbed, has remained remarkably prescient to this day, even 50 years later. At the time, integrated circuits could be constructed which consisted of approximately 1000 components. Today, consumer-level chips are mass-produced that contain over 1 billion transistors. But as we continue to shrink components to squeeze more transistors into a given area, we are approaching fundamental limits of the CMOS field effect transistor. This motivates the study of new ways of encoding, moving, and processing

information.

A promising candidate for next-generation information technology exists in Spintronics [1]. These devices will take advantage of electron spin as a means for moving, storing, and processing information. In principle, spin-based circuits have the potential to operate faster than charge-based circuits, while simultaneously dissipating significantly less power [2]. Recently, magnetic random access memory (MRAM) has come onto the scene. MRAM is based on giant magnetoresistance, which results from spin-dependent scattering of electrons when entering a ferromagnetic material. The 2007 Nobel prize in physics was awarded to Fert and Grünberg for their discovery of giant magnetoresistance [3, 4]. Spin-based field effect transistors, first proposed by Datta and Das in 1990 [5], and very recently demonstrated in InGaAs 2-dimensional electron gases using quantum point contacts to inject and detect spin polarization [6], would provide an ideal interface between magnetic storage technologies and computational devices. Beyond conventional spintronics, spins offer an ideal two-level system with which to implement a truly quantum computer.

Spintronics and quantum computation using electron spins in solid state devices will both require a profound understanding of spin dynamics in semiconductors. In this dissertation, various aspects of spin dynamics, transport, and coupling to the nuclear spin system in GaAs and the ternary alloy InGaAs will be investigated. In Chapter II, the most relevant physical, electronic, and optical properties of the materials used are presented and discussed. In Chapter III, details of the experimental apparatus and methodologies are developed. The coupling between the electron and nuclear spin systems is explored in Chapter IV. Finally, corrections to commonly used time-resolved Faraday rotation measurements resulting from previous pulses are presented in Chapter. V.

CHAPTER II

Electronic and optical properties of GaAs and InGaAs

Though the vast majority of integrated circuits are fabricated on silicon today, the III-V semiconductor gallium arsenide has many advantages over silicon. GaAs has a higher electron mobility and saturated electron velocity, meaning that transistors built in GaAs can operate at a higher frequency than the corresponding transistor in silicon. Its wider band gap also means that thermal excitation of electrons to the conduction band is less of a concern at typical operating temperatures. GaAs has a direct band gap, which means that it is much more efficient at absorbing and emitting light, as transitions from the band minimum do not require interactions with a phonon to conserve momentum. The optical selection rules also support straight-forward optical injection and detection of conduction band electron spin polarization. However, except for in niche applications, GaAs cannot compete with the low price of silicon-based electronics due to the lack of economies of scale and relatively high cost of raw materials. Additionally, GaAs does not possess a native oxide, complicating design considerations for chips built on GaAs.

GaAs has zincblende crystal structure, which means all bonds are tetrahedral, and each gallium atom bonds with four arsenic atoms and vice versa. This structure can also be described as two inter-penetrating face-centered cubic (FCC) lattices, one of gallium and another of arsenic. The unit cell is also face-centered cubic, which means that the reciprocal lattice is body-centered cubic [7]. The unit cell is shown in Fig. 2.1. In this chapter, the most

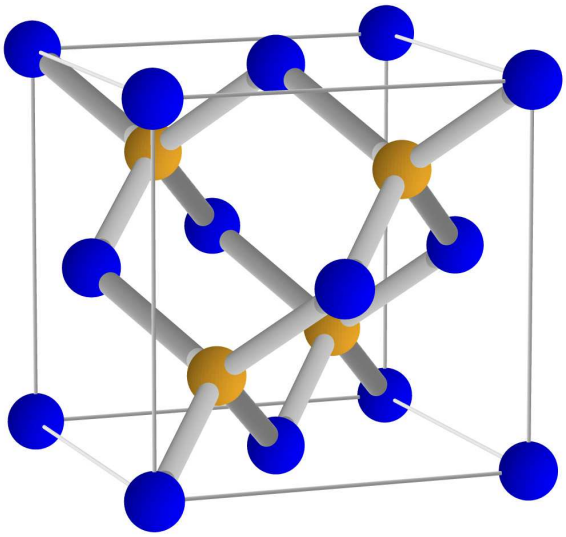

Figure 2.1: Unit cell of the zincblende crystal structure. Each gallium atom (yellow) is bonded to four arsenic atoms (blue) and vice versa. The unit cell contains 8 atoms total, including four of each species. Figure adapted from Ref. [8] with permission.

salient physical, electronic, and optical properties of GaAs to the experiments and results presented in later chapters will be introduced.

2.1 GaAs band structure

For the purposes of understanding the physical basis upon which our measurements rest, it is sufficient to use the nearly-free electron and mean field approximations when describing the effects of the GaAs lattice on the electrons within the material. With the modest electric fields and low doping densities we will encounter in this work, the bands may be approximated as parabolic, with band dispersions calculated using first-order perturbation theory due to the $\mathbf{k} \cdot \mathbf{p}$ term in the Hamiltonian. In this section, the chief result will be outlined; primarily, that the effect of the lattice can be included by introducing an effective mass for the electrons which differs from its vacuum value.

We start with the mean field approximation. The assumption here is that all electrons experience the same average potential, which is periodic and matches the symmetries of the crystal. Neglecting electron-electron interactions, all electron states are solutions of the

following single-electron Hamiltonian:

$$\mathscr{H}_{1e}\Psi(\mathbf{r}) = \left(\frac{p^2}{2m} + V(\mathbf{r})\right)\Psi(\mathbf{r}) = E_n\Psi(\mathbf{r}) \tag{2.1}$$

We now make use of the fact that in a periodic potential, the single electron states Ψ can be written as Bloch states, of the form:

$$\Psi_{n\mathbf{k}} = e^{i\mathbf{k}\cdot\mathbf{r}}u_{n\mathbf{k}}(\mathbf{r}) \tag{2.2}$$

where $\mathbf{k}$ is the electron wave vector in the first Brillouin zone[1], n is the band index, and $u_{n\mathbf{k}}$ is a function which has the same periodicity as the lattice [9]. Plugging this form for the single-electron states into the Hamiltonian in Eqn. 2.1, we arrive at the following expression, whose solution generates the periodic functions $u_{n\mathbf{k}}$:

$$\left(\frac{p^2}{2m} + \frac{\hbar\mathbf{k}\cdot\mathbf{p}}{m} + \frac{\hbar^2k^2}{2m} + V\right)u_{n\mathbf{k}} = E_{n\mathbf{k}}u_{n\mathbf{k}} \tag{2.3}$$

The strategy employed in the perturbative approach in the $\mathbf{k}\cdot\mathbf{p}$ method is to solve Eqn. 2.3 for $\mathbf{k} = 0$, and then treat the case of non-zero $\mathbf{k}$ as a perturbation to the solution found at $\mathbf{k} = 0$. With $\mathbf{k} = 0$, Eqn. 2.3 becomes:

$$\left(\frac{p^2}{2m} + V\right)u_{n\mathbf{k}} = E_{n\mathbf{0}}u_{n\mathbf{0}} \tag{2.4}$$

Since the functions $u_{n\mathbf{0}}$ form a complete orthonormal basis, we can calculate the perturbed Bloch functions in terms of the unperturbed solution:

$$u_{n\mathbf{k}} = u_{n\mathbf{0}} + \frac{\hbar}{m}\sum_{n'\neq n}\frac{\langle u_{n\mathbf{0}}|\mathbf{k}\cdot\mathbf{p}|u_{n'\mathbf{0}}\rangle}{E_{n\mathbf{0}} - E_{n'\mathbf{0}}}u_{n'\mathbf{0}} \tag{2.5}$$

[1]The first Brillouin zone is understood to be the Wigner-Seitz unit cell of the reciprocal lattice, whose lattice vectors are defined by $\mathbf{b_i} = 2\pi\frac{(\mathbf{a}_j\times\mathbf{a}_k)}{(\mathbf{a}_1\times\mathbf{a}_2)\cdot\mathbf{a}_3}$ and cyclic permutations of the indices i, j, and k, where the vectors $\mathbf{a}$ are the lattice vectors in real space. The term in the denominator is the volume of the primitive cell in real space.

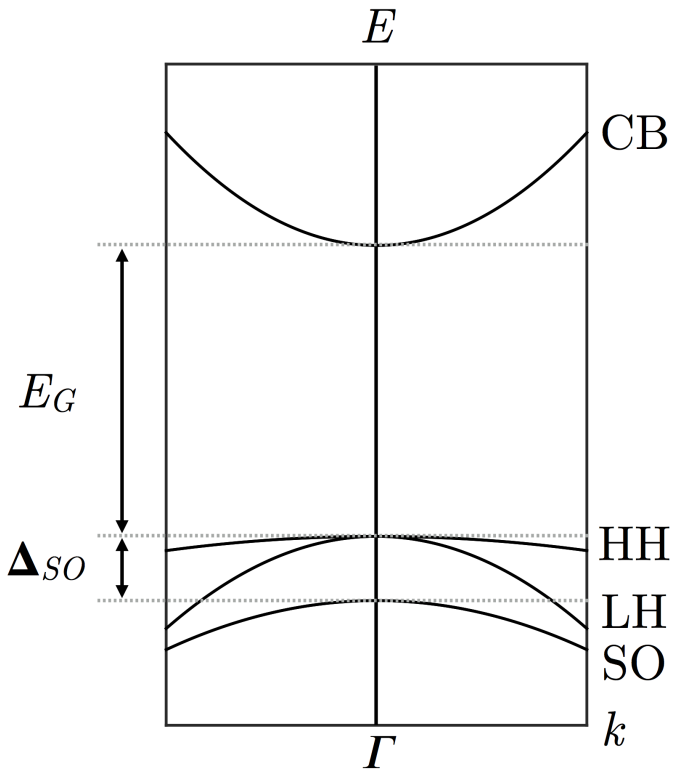

Figure 2.2: GaAs band structure near the Γ point. Three valance band states are present; the heavy hole (HH) and light hole (LH) bands are degenerate at $\mathbf{k} = 0$, while the split-off (SO) band lies below the HH and LH bands by $\Delta_{SO} = 0.341$ eV. GaAs has a direct band gap of 1.519 eV. Splittings and effective masses ($m^* \propto (d^2E/dk^2)^{-1}$) are plotted to scale.

These perturbed solutions will have associated with them an energy $E_{n\mathbf{k}}$ given by:

$$E_{n\mathbf{k}} = E_{n\mathbf{0}} + \frac{\hbar^2 k^2}{2m} + \frac{\hbar^2}{m^2} \sum_{n' \neq n} \frac{|\langle u_{n\mathbf{0}} | \mathbf{k} \cdot \mathbf{p} | u_{n'\mathbf{0}} \rangle|^2}{E_{n\mathbf{0}} - E_{n'\mathbf{0}}} \tag{2.6}$$

The key result is that this dispersion relation can be rewritten as a simple parabolic dispersion with an effective electron mass that differs from its vacuum value. Written in this form, the energy is given by:

$$E_{n\mathbf{k}} = E_{n\mathbf{0}} + \frac{\hbar^2 k^2}{2m^*} \tag{2.7}$$

where m^* is the effective mass, defined by:

$$\frac{1}{m^*} = \frac{1}{m} + \frac{2}{k^2 m^2} \sum_{n' \neq n} \frac{|\langle u_{n\mathbf{0}} | \mathbf{k} \cdot \mathbf{p} | u_{n'\mathbf{0}} \rangle|^2}{E_{n\mathbf{0}} - E_{n'\mathbf{0}}} \tag{2.8}$$

The process of calculating the effective mass for electrons in the valence band is largely similar, however degenerate perturbation theory must be used as the heavy and light hole states are degenerate at the Γ point. The valence band is characterized by p-like Bloch functions with orbital angular momentum $l = 1$, which, when combined with the spin, gives a total angular momentum $j = l + s = 3/2$. A third valance band exists, known as the split-off band, which sits below the heavy and light hole bands at the Γ point by an energy $\Delta_{SO} = 0.341$ eV. Due to the large detuning from the heavy and light hole states, we will neglect the split-off band states. Additionally, it should be noted that the effective mass for valence band hole states is found to be negative; that is, energy is maximized at $\mathbf{k} = 0$, so that holes tend to accumulate at the top of the valence band near the Γ point. The approximate band structure near the Γ point arrived at through first-order $\mathbf{k} \cdot \mathbf{p}$ is shown in Fig. 2.2.

Parameter	GaAs	$In_{0.04}Ga_{0.96}As$	InAs	C
E_G	1.519	1.457	0.417	0.477
a	5.6533 Å	5.6695 Å	6.0583 Å	0
m_c^*b	0.067	0.065	0.026	0.0091
m_{LH}^*	0.090	0.087	0.027	0.0202
m_{HH}^*	0.35	0.35	0.33	-0.145

Table 2.1: Band Gap, lattice constant, effective masses, and bowing parameter C for GaAs, InAs, and the ternary alloy $In_{0.04}Ga_{0.96}As$ used in measurements of dynamic nuclear polarization presented in Chapter IV [10].

2.2 InGaAs ternary alloy

For many of the experiments presented here, we use a dilute ternary alloy of $In_xGa_{1-x}As$ with $x = 4\%$ which is grown by molecular beam epitaxy atop a semi-insulating substrate. There are two primary considerations that motivate the use of this material. First, the band gap of the alloy is smaller than that in GaAs, so that the substrate appears transparent to the optical beams used to inject and detect spin polarizations. Second, the differing lattice constants between the GaAs substrate and InGaAs grown on top of it leads to biaxial strain. This strain leads to a **k**-dependent effective magnetic field which couples to the electron spin.

The physical properties of ternary alloys can be approximated as linear interpolations between the two binary materials which make up the alloy with a 'bowing parameter' which can be considered a first-order correction to errors in this linear interpolation [10]. For some physical parameter P with value P_A in material A and P_B in material B, the value of P in material A_xB_{1-x} is given by:

$$P_{A_xB_{1-x}} = xP_A + (1-x)P_B + x(1-x)C \tag{2.9}$$

where C is the bowing parameter. Table 2.1 includes values of important material parameters for GaAs, InAs, and $In_xGa_{1-x}As$ with $x = 4\%$.

2.3 Spin-orbit coupling

When electrons move throughout the crystal, lattice potential gradients in the lab frame are seen partially as magnetic fields in the electron rest frame due to the Lorentz transformation of the fields. The magnetic field in the electron frame $\mathbf{B}'$ due to an electric field in the lab frame $\mathbf{E}$ can be calculated from [11]:

$$\mathbf{B}' = -\frac{\gamma}{mc^2}\mathbf{p} \times \mathbf{E} \tag{2.10}$$

where γ is the Lorentz factor given by:

$$\gamma = \frac{1}{\sqrt{1 - (\frac{v}{c})^2}} \tag{2.11}$$

This magnetic field is coupled to the electron spin, giving rise to the following term in the Hamiltonian:

$$\mathscr{H}_{SOC} = \frac{\hbar^2}{4m^{*2}c^2}\left(\nabla V \times \mathbf{k}\right) \cdot \sigma \tag{2.12}$$

The presence of a spin-orbit field can be understood as a result of the breaking of a spatial inversion symmetry. In situations where the system is invariant under spatial inversion, it is clear that it must also be the case that the energy for electrons with wavevector $\mathbf{k}$ is the same as that for electrons with wavevector $-\mathbf{k}$, or $E(\mathbf{k}) = E(-\mathbf{k})$. Kramer's degeneracy states that energies should always be invariant under time reversal [12]. Including the spin of the electrons, which are flipped under time reversal, this means that $E(\mathbf{k}, \uparrow) = E(-\mathbf{k}, \downarrow)$. Taken together, these two symmetries imply that $E(\mathbf{k}, \uparrow) = E(\mathbf{k}, \downarrow)$. Breaking of inversion symmetry, however, means that this equality does not hold away from $\mathbf{k} = 0$. In such a situation, there exists a $\mathbf{k}$-dependent splitting between the spin states. This splitting

appears in the Hamiltonian as if it were a $\mathbf{k}$-dependent effective magnetic field:

$$\mathbf{B}_{\text{eff}} = -\frac{\hbar^3}{4g^* m^{*2} c^2 \mu_B} (\nabla V \times \mathbf{k}) \tag{2.13}$$

$$\mathscr{H}_{SOC} = -\boldsymbol{\mu}_e \cdot \mathbf{B}_{\text{eff}} \tag{2.14}$$

In the following sections, the spin-orbit field resulting from various types of inversion symmetry breaking are discussed.

2.3.1 Dresselhaus field

In GaAs, and indeed all materials with zincblende crystal structure, there exists a bulk inversion asymmetry in the material. This asymmetry can be understood as resulting from a breaking of inversion symmetry at the point along a bond midway between a Ga and As nucleus. At this point, there is clearly a breaking of inversion symmetry, as an electron moving along the bond sees a Ga nucleus if it's traveling in one direction and an As nucleus if it's traveling in the opposite direction. This bulk inversion asymmetry, first discussed in detail in Ref. [13], gives rise to the so-called Dresselhaus field. This field can be estimated using the perturbative $\mathbf{k} \cdot \mathbf{p}$ method, and to lowest order, is found to be[2]:

$$\mathbf{B}_D = \gamma[k_x(k_y^2 - k_z^2)\hat{\mathbf{x}} + k_y(k_z^2 - k_x^2)\hat{\mathbf{y}} + k_z(k_x^2 - k_y^2)\hat{\mathbf{z}}] \tag{2.15}$$

where γ is the cubic Dresselhaus coefficient, a material-specific parameter.

For our purposes, the electrons are confined within the InGaAs epilayer, so that the average electron momentum along $\hat{\mathbf{z}}$, $\langle k_z \rangle$, is zero. Averaging over all electrons, then, for electron motion in the sample plane, we have:

$$\mathbf{B}_D = \gamma[k_x k_y^2 \hat{\mathbf{x}} - k_y k_x^2 \hat{\mathbf{y}}] \tag{2.16}$$

[2]Here, $\hat{\mathbf{x}}$, $\hat{\mathbf{y}}$, and $\hat{\mathbf{z}}$ are defined to be parallel to [100], [010], and [001], respectively

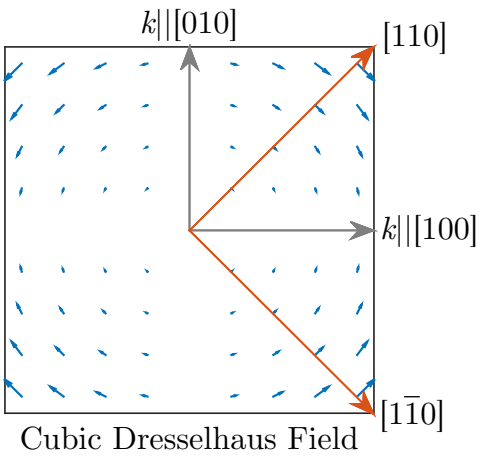

Figure 2.3: Cubic Dresselhaus field resulting from bulk inversion asymmetry in GaAs plotted in momentum space. Arrows show the direction and relative strength of the spin orbit field for electrons with momentum corresponding to the location of the arrow.

This field is plotted in Fig. 2.3. Of particular importance in future sections is the field for electrons moving along [110] and [1$\bar{1}$0]. In both directions, the field is perpendicular to the electron momentum.

2.3.2 Bychkov-Rashba field

Next, we consider so-called structural inversion asymmetry. This is understood to result from asymmetry due to heterojunctions in the growth axis. These will result in built-in electric fields along the growth direction. When these electric fields are transformed into the electron rest frame, they result in the Bychkov-Rashba field, which is frequently referred to as the Rashba field [14]. This field can be tuned by applying an out-of-plane voltage across the sample. This technique was proposed as a potential gating mechanism for use in the Datta-Das spin modulator [5].

The Rashba field is isotropic for in-plane momenta, following the cylindrical symmetry of the electric fields from which it originates. It can be written as:

$$\mathbf{B}_R = \alpha[k_y\hat{\mathbf{x}} - k_x\hat{\mathbf{y}}] \tag{2.17}$$

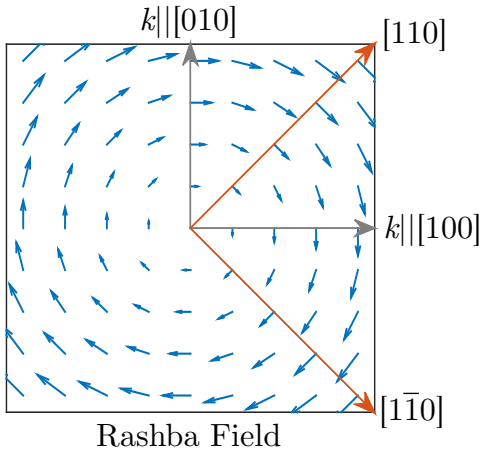

Figure 2.4: Rashba spin orbit field resulting from structural inversion asymmetry plotted in momentum space.

where α is the Rashba coefficient. The field is plotted in Fig. 2.4. Again, we find that for electrons with momentum along [110] or [1$\bar{1}$0], the Rashba field is perpendicular to the direction of electron momentum.

2.3.3 Strain-induced spin-orbit coupling

The presence of strain in the material leads to further spin-orbit coupling [15, 16, 17]. Strain within the material is characterized by the strain tensor $\overleftrightarrow{\varepsilon}$, defined by:

$$\varepsilon_{ij} = \frac{1}{2}\left(\frac{\partial u_i}{\partial r_j} + \frac{\partial u_j}{\partial r_i}\right) \tag{2.18}$$

The InGaAs material discussed in this dissertation is strained due to the fact that there is a small lattice mismatch with the GaAs substrate on which it is grown. Since the lattice constant for the InGaAs is slightly larger than the lattice constant for GaAs, the InGaAs will be under compressive strain in the sample plane. This compressive strain results in an elongating of the lattice in the vertical direction, leading to biaxial strain. This will contribute a spin-orbit coupling term to the Hamiltonian of the form:

$$\mathscr{H}_{\text{biaxial}} = D\left[(\varepsilon_{yy} - \varepsilon_{zz})k_x\sigma_x + (\varepsilon_{zz} - \varepsilon_{xx})k_y\sigma_y + (\varepsilon_{xx} - \varepsilon_{yy})k_z\sigma_z\right] \tag{2.19}$$

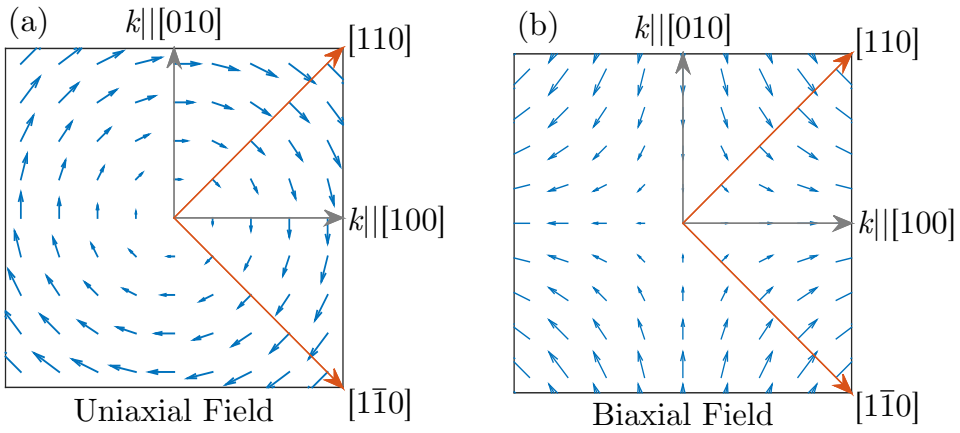

Figure 2.5: Plots showing the **k**-dependent effective magnetic fields arising from uniaxial (a) and biaxial (b) strain. The uniaxial strain spin-orbit field is identical in form to the Rashba field. The biaxial field shares the same symmetry as the cubic Dresselhaus field, but differs in magnitude and direction. Both spin-orbit fields are perpendicular to the electron momentum for motion along [110] and [1$\bar{1}$0].

where D is a material parameter. The compressive strain in the sample plane will be the same along the $\hat{\mathbf{x}}$ and $\hat{\mathbf{y}}$ axes, so that $\varepsilon_{xx} = \varepsilon_{yy}$. Any uniaxial strain in the material adds another term to the Hamiltonian as well, given by:

$$\mathscr{H}_{\text{uniaxial}} = \frac{C_3}{2}\left[(\varepsilon_{zx}k_z - \varepsilon_{xy}k_y)\sigma_x + (\varepsilon_{xy}k_x - \varepsilon_{yz}k_z)\sigma_y + (\varepsilon_{yz}k_y - \varepsilon_{zx}k_z)\sigma_z\right] \tag{2.20}$$

We again work under the assumption that $\langle k_z \rangle = 0$, so that these terms lead to the following spin-orbit fields for in-plane momentum:

$$\mathbf{B}_{\text{biaxial}} = \beta(k_x\hat{\mathbf{x}} - k_y\hat{\mathbf{y}}) \tag{2.21}$$

$$\mathbf{B}_{\text{uniaxial}} = \delta(k_y\hat{\mathbf{x}} - k_x\hat{\mathbf{y}}) \tag{2.22}$$

The uniaxial and biaxial strain spin orbit fields are plotted in Fig. 2.5, panels (a) and (b), respectively.

We may now combine all the spin-orbit fields discussed. These fields have two principle directional dependencies, corresponding to Rashba and Dresselhaus forms. The total spin-

orbit field is given by:

$$\mathbf{B}_{SOC}(\mathbf{k}) = \big((\alpha+\delta)k_y + (\beta+k_y^2)k_x\big)\hat{\mathbf{x}} - \big((\alpha+\delta)k_x + (\beta+\gamma k_x^2)k_y\big)\hat{\mathbf{y}} \tag{2.23}$$

Because of the modest electric fields and low doping levels, we will assume that $\mathbf{k}$ is small, so that the cubic Dresselhaus field may be neglected and γ is taken to be 0. It should also be noted that for all the sources of spin-orbit coupling presented here, the spin orbit field will be perpendicular to the electron momentum when electrons are traveling along the [110] and $[1\bar{1}0]$ axes. For the remainder of this dissertation, we will restrict ourselves to considering electron motion along those directions.

2.4 Optical properties of GaAs

2.4.1 Selection rules

In the dipole approximation, transition rates from a valence band state $|\psi_{vb}\rangle$ to a conduction band state $|\psi_{cb}\rangle$ are connected by the electric dipole operator, and given by Fermi's golden rule [18]:

$$w_{vb\to cb} = \frac{2\pi}{\hbar}\left|\langle\psi_{cb}| - e\vec{r}\cdot\vec{E}|\psi_{vb}\rangle\right|^2 \delta(E_g - \hbar\omega) \tag{2.24}$$

It is convenient here to use symmetry arguments and invoke the well-developed methods of atomic physics. In the case of hydrogen, the Coulomb potential with which the electron interacts is spherically symmetric. At first glance, the presence of the crystal in a semiconductor breaks spherical symmetry. Fortunately, while we can no longer enforce that our solutions behave as members of the continuous rotational symmetry group, we can still appeal to a softer form of symmetry where solutions must possess the same symmetries as the crystal. We again express electron energy eigenstates in the periodic lattice potential as Bloch states [7]:

$$\Psi_{n,m,\mathbf{k}}(\mathbf{r}) = e^{i\mathbf{k}\cdot\mathbf{r}} u_{n,m,\mathbf{k}}(\mathbf{r}) \tag{2.25}$$

where $\mathbf{k}$ is the quasimomentum, n the band index, and u will be invariant under all the crystal symmetry operations. We have now added m, the projection of the spin of the electron onto the z axis, to the notation for u. While care is required, discrete symmetry allows many methods developed in the context of atomic physics to be brought to bear in crystals as well.

For conduction band states, we may approximate u as consisting of the spin and orbital angular momentum parts separately [15]

$$u_{\frac{1}{2}}(\vec{r}) = S\uparrow, \qquad u_{-\frac{1}{2}}(\vec{r}) = S\downarrow \tag{2.26}$$

Since the conduction band orbitals have $L = 0$, S above will have the same symmetry as the lowest order spherical harmonic, Y_{00} [19]. The valence band states have $L = 1$, and are thus complicated by the nontrivial spin-orbit coupling term, $H_{so} = \lambda\vec{L}\cdot\vec{S}$. Therefore, l and s are no longer good quantum numbers and instead j, the total angular momentum, must be used. The Clebsch-Gordon coefficients can be used to express the eigenstates as combinations of l and s states [18]. Since $L = 1$ and $S = \frac{1}{2}$, J will will take on the values $L+S, L+S-1, \ldots, |L-S|$ while $m_j = -J, -J+1, \ldots, J-1, J$. The following states are arrived at from tables of Clebsch-Gordon coefficients [20]:

$$\text{Heavy and Light Hole Bands:} \quad u_{3/2}^{m_j} = \begin{cases} |\frac{3}{2},\frac{3}{2}\rangle = |1,1\rangle\uparrow \\ |\frac{3}{2},\frac{1}{2}\rangle = \frac{1}{\sqrt{3}}\left[|1,-1\rangle\downarrow + \sqrt{2}|1,0\rangle\uparrow\right] \\ |\frac{3}{2},-\frac{1}{2}\rangle = \frac{1}{\sqrt{3}}\left[|1,-1\rangle\uparrow + \sqrt{2}|1,0\rangle\downarrow\right] \\ |\frac{3}{2},-\frac{3}{2}\rangle = |1,-1\rangle\downarrow \end{cases}$$

$$\text{Split-off Holes} \quad u_{1/2}^{m_j} = \begin{cases} |1/2,1/2\rangle = \frac{1}{\sqrt{3}}\left[|1,0\rangle\uparrow - \sqrt{2}|1,1\rangle\downarrow\right] \\ |1/2,-1/2\rangle = \frac{1}{\sqrt{3}}\left[|1,0\rangle\downarrow - \sqrt{2}|1,-1\rangle\uparrow\right] \end{cases}$$

These expressions offer a convenient avenue for calculating transition matrix elements. We

are interested only in the relative transition strengths here, so common constants will be dropped. Circularly polarized light tuned to the band gap energy ($\omega_g = E_g/\hbar$) is incident upon the sample causing interband transitions to the conduction band. It is assumed that Δ_{so}, as defined above, is large compared to the incident light linewidth so that we may neglect transitions from the split-off band. Starting with right-circularly polarized light (σ^+), the electric field polarization vector is $\hat{e} = \frac{1}{\sqrt{2}}(\hat{\mathbf{x}} + i\hat{\mathbf{y}})$ and the position unit vector is $\hat{r} = \sin\theta\cos\phi\hat{\mathbf{x}} + \sin\theta\sin\phi\hat{\mathbf{y}} + \cos\theta\hat{\mathbf{z}}$, so that:

$$\begin{aligned} -e\vec{r}\cdot\vec{E} &= -erE\left[(\sin\theta\cos\phi\hat{\mathbf{x}} + \sin\theta\sin\phi\hat{\mathbf{y}} + \cos\theta\hat{\mathbf{z}})\cdot(\frac{1}{\sqrt{2}}(\hat{\mathbf{x}} \pm i\hat{\mathbf{y}})\right] \\ &= \frac{-erE}{\sqrt{2}}(\sin\theta\cos\phi \pm i\sin\theta\sin\phi) \\ &\sim \mp reE\ Y_1^{\pm 1} \end{aligned}$$

Expressing the spherical harmonics as:

$$\begin{aligned} |1,\pm 1\rangle &\sim \mp\sin(\theta)exp(\pm i\phi) \\ |1,0\rangle &\sim \cos(\theta) \end{aligned}$$

and restricting ourselves to σ^+ light, we may now directly calculate transition matrix elements. Starting with the $|3/2,3/2\rangle_{vb} \rightarrow |1/2,1/2>_{cb}$ transition, we seek to calculate:

$$\begin{aligned} \langle 0,0|\langle\uparrow| - eEr\ Y_1^1|1,1\rangle|\uparrow\rangle &= -erE\ \langle 0,0|Y_1^1|1,1\rangle\langle\uparrow|\uparrow\rangle \\ &= \int_0^{2\pi} d\phi \int_0^{\pi} \sin\theta\ d\theta\ Y_0^0\ Y_1^1\ Y_1^1 \\ &= 0 \end{aligned}$$

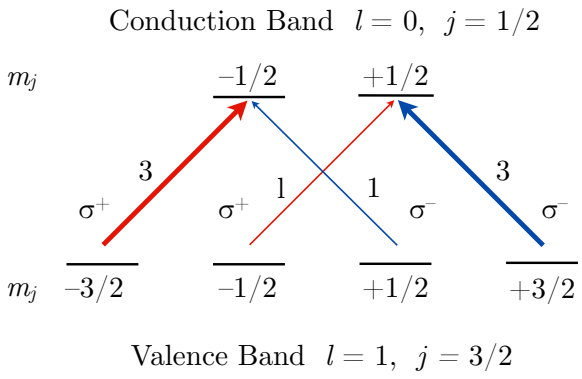

Figure 2.6: Selection rules for $\sigma^{\pm}$ light in GaAs, showing dipole-allowed transitions and their relative transition strengths.

Computing other matrix elements, the following values are found:

$$\langle S\uparrow|Y_1^1|3/2,3/2\rangle = 0 \quad ; \quad \langle S\uparrow|Y_1^1|3/2,1/2\rangle = 0$$
$$\langle S\uparrow|Y_1^1|3/2,-1/2\rangle = \alpha \quad ; \quad \langle S\uparrow|Y_1^1|3/2,-3/2\rangle = 0$$
$$\langle S\downarrow|Y_1^1|3/2,3/2\rangle = 0 \quad ; \quad \langle S\downarrow|Y_1^1|3/2,1/2\rangle = 0$$
$$\langle S\downarrow|Y_1^1|3/2,-1/2\rangle = 0 \quad ; \quad \langle S\downarrow|Y_1^1|3/2,-3/2\rangle = \sqrt{3}\alpha$$

where α is a constant. For left-circularly polarized light σ^- the matrix elements are calculated as:

$$\langle S\uparrow|Y_1^{-1}|3/2,3/2\rangle = -\sqrt{3}\alpha \quad ; \quad \langle S\uparrow|Y_1^{-1}|3/2,1/2\rangle = 0$$
$$\langle S\uparrow|Y_1^{-1}|3/2,-1/2\rangle = 0 \quad ; \quad \langle S\uparrow|Y_1^{-1}|3/2,-3/2\rangle = 0$$
$$\langle S\downarrow|Y_1^{-1}|3/2,3/2\rangle = 0 \quad ; \quad \langle S\downarrow|Y_1^{-1}|3/2,1/2\rangle = -\alpha$$
$$\langle S\downarrow|Y_1^{-1}|3/2,-1/2\rangle = 0 \quad ; \quad \langle S\downarrow|Y_1^{-1}|3/2,-3/2\rangle = 0$$

The possible transitions and their relative strengths (which are proportional to the square of the matrix element) for $\sigma^{\pm}$ light are depicted in Fig. 2.6.

2.4.2 Optical injection

Consider the case of σ^+ illumination in undoped GaAs. At zero temperature, all valence band states will be filled while all conduction band states will be empty. Because the transition $|3/2,-3/2\rangle_{vb} \rightarrow |1/2,-1/2\rangle_{cb}$ is three times more likely to occur than $|3/2,-1/2\rangle_{vb} \rightarrow |1/2,1/2\rangle_{vb}$, the electrons excited to the conduction band will have a degree of spin polarization of -1/2 with the axis of quantization defined by the photon wave vector, as defined by:

$$P = \frac{n_\uparrow - n_\downarrow}{n_\uparrow + n_\downarrow} \tag{2.27}$$

Due to spin orbit interactions, the hole spin lifetime is short ($\sim$ 1 ps)[15]. Once the holes have depolarized, residual spin polarization will be due to conduction band electrons. With no doping, the spin lifetime will be limited to the electron-hole recombination time. Measurements of the contribution to the total spin polarization resulting from the optical carriers in GaAs presented in Chapter V give a recombination time of 78 ps at 10 K, and the recombination time is assumed to be on the same order for the materials and experimental parameters used in this dissertation.

The introduction of n-type dopants into the material allows polarization of conduction band electrons to exceed the recombination time, but decreases the degree of polarization of conduction band electrons immediately after absorption. If the conduction band electrons are assumed to be unpolarized before the arrival of a circularly polarized pump pulse, then after absorption the number density of electrons in each spin state becomes:

$$n_\uparrow = \frac{n_D}{2} + \frac{n_O}{4} \qquad n_\downarrow = \frac{n_D}{2} + \frac{3n_O}{4} \tag{2.28}$$

where n_D is the doping density and n_O is the density of optically generated carriers. This leads to a degree of polarization of:

$$P = \frac{(\frac{n_D}{2} + \frac{n_O}{4}) - (\frac{n_D}{2} + \frac{3n_O}{4})}{n_O + n_D} = -\frac{1}{2}\frac{n_O}{(n_O + n_D)} \tag{2.29}$$

Since the hole spin lifetime is much shorter than the radiative recombination time, it is a reasonable assumption that recombination of each spin species occurs at a rate which is proportional to the number of electrons in each state (that is, the holes recombine randomly). This means that the degree of polarization remains after recombination, but the total carrier density returns to the doping density. After this process, we are left with a spin-polarization in the conduction band.

2.5 Optical spin detection

There exist two commonly used optical methods for detecting spin polarization of conduction band electrons. The first of these relies on the detection of the degree of circular polarization of emitted light, which will be proportional to the spin polarization along the wave vector of the emitted light. This method was first demonstrated in GaSb by Parsons in 1969 [21], and shortly thereafter in GaAs by Ekimov and Safarov [22].

After excitation, hole spins rapidly dephase due to spin orbit interactions. Any remaining polarization after that time therefore resides in electron spins. The selection rules discussed above may be used again to show that photoluminescence will have a net circular polarization. Written in terms of the spin state population of the conduction band, the relative transition strengths for the available transitions result in emitted intensities of:

$$\begin{aligned} I_{\sigma^+} &= n_+ + 3n_- \\ I_{\sigma^-} &= 3n_+ + n_- \end{aligned}$$

By measuring the relative intensities of σ^+ and σ^- photoluminescence, it is possible to measure spin polarization in the direction parallel to the propagation of the light. This technique can be used in concert with streak cameras to yield time-resolved measurements of spin-polarized recombination.

When a magnetic field transverse to the direction in which photoluminescence is collected

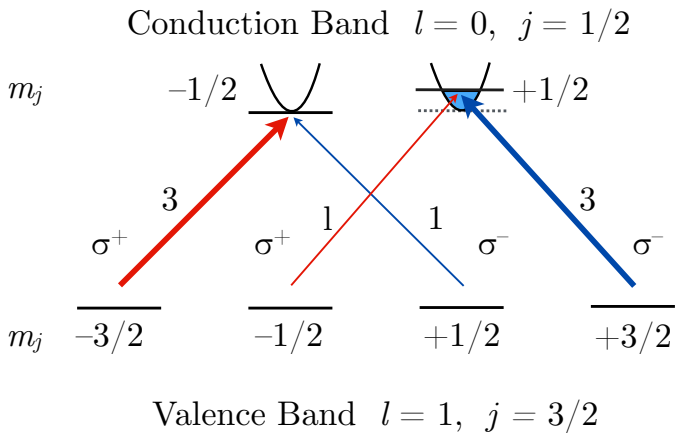

Figure 2.7: Selection rules in the case of spin-polarized conduction band electrons. The absorption edge for transitions to the conduction band with $m_j = +1/2$ is shifted to higher energy due to state filling at the bottom of the band.

is applied, spins will precess about the magnetic field, which leads to a diminishing of the degree of polarization of the emitted light. This is known as the Hanlé effect, which was first discovered in emission spectra of polarized atoms in 1924 [23]. The change in photoluminescence polarization with magnetic field can be used to measure the product of the spin lifetime and the precession frequency.

2.5.1 Faraday and Kerr rotation

Measurements of photoluminescence polarization are limited by the fact that the spin is measurable only when carriers recombine. With the introduction of ultra-fast optical techniques, new measurements based upon Faraday or Kerr rotation have afforded a new window into rapid dynamical spin processes. The Faraday effect, discovered in 1845 by Michael Faraday [24], is the rotation of a linearly polarized beam in a material with a magnetic field parallel to the direction of light propagation. If the rotation takes place upon reflection from a material instead of transmission through it, it is typically referred to as Kerr rotation, though the mechanism is the same in each case.

Faraday rotation which occurs near the absorption edge when the conduction band electrons are spin polarized can be understood as a result of differing Fermi energies for each

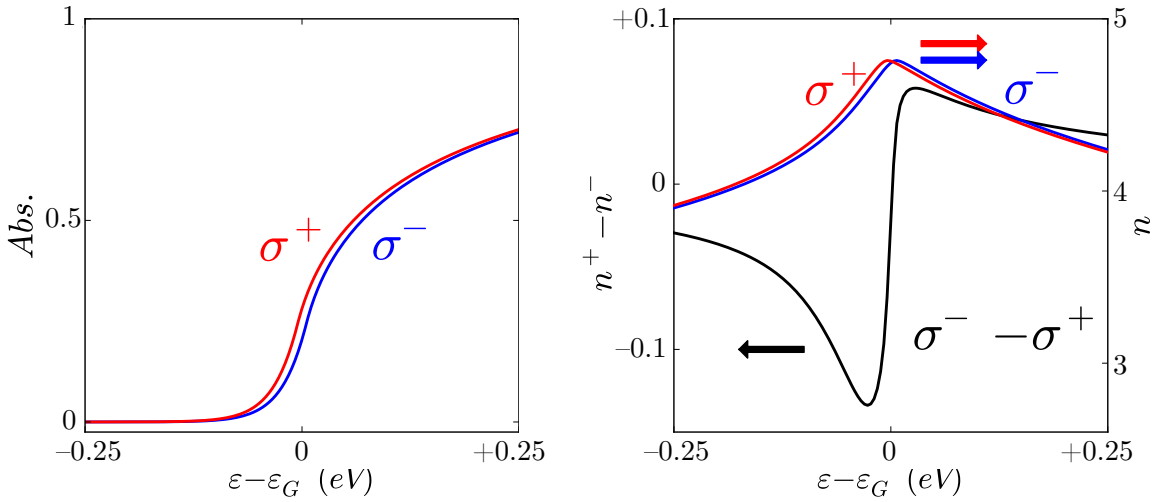

Figure 2.8: A difference in absorption for opposite circular polarizations (left) leads to a difference in their indices of refraction (right). This circular birefringence will rotate the polarization of a linearly polarized beam as it travels through the material. Figure adapted from Ref. [17] with permission.

conduction band spin state. State filling in the spin sub-band with higher occupation means that interband transitions which excite an electron to that state require a higher photon energy than for the low-occupation sub-band. This is shown diagramatically in Fig. 2.7. Here, state filling in the spin up state shifts the absorption edge for interband transitions resulting in a spin-up electron in the conduction band to higher photon energy. Near the band edge, this results in a circular dichroism; that is, one circular polarization is absorbed more readily than the other. The left panel in Fig. 2.8 shows such a situation. Here, the absorption at and above the band gap is assumed to follow the density of states, which is proportional to $\sqrt{E - E_g}$, while absorption below the band gap results from the Urbach tail [25], dropping off exponentially away from the band edge.

In systems which obey causality, the Kramers-Kronig relations establish a relationship between the real part part of the permittivity (which is the square of the index of refraction) and the imaginary part (which is related to absorption in the material) [11, 26, 27]. The

relationship between the real and imaginary parts of the permittivity are as follows:

$$\epsilon_1(\omega) = 1 + \frac{1}{\pi}\mathscr{P}\int_{-\infty}^{\infty}\frac{\epsilon_2(\omega')\ d\omega'}{\omega' - \omega}$$

$$\epsilon_2(\omega) = \frac{-1}{\pi}\mathscr{P}\int_{-\infty}^{\infty}\frac{\epsilon_1(\omega') - 1}{\omega' - \omega}d\omega'$$

Here, $\mathscr{P}$ indicates that the principal part of the integrals should be taken. As a result of these constraints, the circular dichroism will lead to a circular birefringence. The calculated index of refraction for each circular polarization is plotted in the right panel of Fig. 2.8. The energy-dependent circular birefringence, which is the difference in indices of refraction, is plotted in black.

To understand the result of the circular dichroism and birefringence on a linearly polarized beam, we make use of the following definitions:

$$\begin{aligned}\sigma^+ &= \frac{\hat{\mathbf{x}} + i\hat{\mathbf{y}}}{\sqrt{2}} \\ \sigma^- &= \frac{\hat{\mathbf{x}} - i\hat{\mathbf{y}}}{\sqrt{2}}\end{aligned} \quad \Longleftrightarrow \quad \begin{aligned}\hat{\mathbf{x}} &= \frac{\sigma^+ + \sigma^-}{\sqrt{2}} \\ \hat{\mathbf{y}} &= \frac{\sigma^+ - \sigma^-}{i\sqrt{2}}\end{aligned} \tag{2.30}$$

Light which is polarized along $\hat{\mathbf{x}}$ can be written as an equal admixture of counter-rotating circularly polarized beams. After passing through a material exhibiting circular dichroism, there will be an unequal amount of each circularly polarized component remaining. This leads to a non-zero ellipticity in the transmitted or reflected beam, which can be used directly as a measure of the conduction band electron spin polarization along $\hat{z}$. Similarly, in the case of circularly birefringence, there will be a phase difference between the two circular polarization components of a linearly polarized beam:

$$\hat{\mathbf{x}} = \frac{\sigma^+ + \sigma^-}{\sqrt{2}} \Longrightarrow \frac{e^{i\phi/2}\sigma^+ + e^{-i\phi/2}\sigma^-}{\sqrt{2}} = \frac{\cos(\phi/2)\hat{x} + \sin(\phi/2)\hat{y}}{\sqrt{2}} \tag{2.31}$$

This relative phase shift between the σ^+ and σ^- components rotates the linearly polarized

beam. The angle of rotation is half the total phase shift ϕ, which in turn depends on the magnitude of the $\hat{k}$-parallel spin polarization. It is this rotation of the linear polarization of an incident beam that will be used to measure spin polarization in the following chapters.

2.6 Spin dynamics in GaAs

2.6.1 Free electrons

When a magnetic dipole is subjected to an external magnetic field, a torque is generated on the dipole, given by $\boldsymbol{\tau} = \boldsymbol{\mu} \times \mathbf{B}$. Since the electron spin moment is tied to the intrinsic spin angular momentum, this torque leads to a precession governed by $\boldsymbol{\tau} = d\mathbf{L}/dt$ where $\mathbf{L}$ is the spin angular momentum. Since work must be done to rotate the dipole around an axis perpendicular to the external magnetic field, there is a mechanical energy associated with the relative alignment of the two:

$$U = -\boldsymbol{\mu} \cdot \mathbf{B} \tag{2.32}$$

In quantum theory, this mechanical energy becomes a term in the Hamiltonian given by:

$$\mathscr{H}_Z = g\mu_B \mathbf{s} \cdot \mathbf{B} \tag{2.33}$$

where g is the Landé g-factor and μ_B is the Bohr magneton. In matrix form, the spin operator $\mathbf{s}$ can be expressed in terms of the Pauli matrices as $\mathbf{s} = \boldsymbol{\sigma}/2$, with:

$$\sigma_x = \begin{pmatrix} 0 & 1 \\ 1 & 0 \end{pmatrix} \quad \sigma_y = \begin{pmatrix} 0 & -i \\ i & 0 \end{pmatrix} \quad \sigma_z = \begin{pmatrix} 1 & 0 \\ 0 & -1 \end{pmatrix} \tag{2.34}$$

which act on a vector whose components are the energy eigenstates. These eigenstates

correspond to spin up and spin down states:

$$|\uparrow\rangle = \begin{pmatrix} 1 \\ 0 \end{pmatrix} \quad |\downarrow\rangle = \begin{pmatrix} 0 \\ 1 \end{pmatrix} \tag{2.35}$$

We now consider the effect of a magnetic field $\mathbf{B} = B\hat{\mathbf{z}}$. s_z operates on the spin-up and down states as follows:

$$\hat{s_z}|\uparrow\rangle = \frac{1}{2}|\uparrow\rangle \tag{2.36}$$

$$\hat{s_z}|\downarrow\rangle = -\frac{1}{2}|\downarrow\rangle \tag{2.37}$$

Since s_z commutes with H, spin eigenstates will also be energy eigenstates [18]. Consider a spin state which is initially along $\hat{\mathbf{x}}$:

$$|\psi(t=0)\rangle = \frac{1}{\sqrt{2}} \begin{pmatrix} 1 \\ 1 \end{pmatrix} \tag{2.38}$$

This corresponds to an eigenstate of the $\hat{s_x}$ operator, where $\hat{s_x} = \hat{\sigma_x}/2$ Using the time evolution operator, the time dependence of the state is calculated as follows:

$$\begin{aligned} |\psi(t)\rangle &= \exp(-iHt/\hbar)|\psi(t=0)\rangle \\ &= \frac{1}{\sqrt{2}} \begin{pmatrix} \exp(-i\Omega t/2) \\ \exp(i\Omega t/2) \end{pmatrix} \end{aligned}$$

where $\Omega = g\mu_B B/\hbar$, which is known as the Larmor precession frequency. Expectation values

for s_x and s_y may then be calculated as:

$$\begin{aligned}
\langle s_x \rangle &= \langle \psi(t) | s_x | \psi(t) \rangle \\
&= \frac{1}{2} \cos \Omega t \\
\langle s_y \rangle &= \langle \psi(t) | s_y | \psi(t) \rangle \\
&= \frac{1}{2} \sin \Omega t
\end{aligned}$$

We see that spins that are aligned perpendicular to the magnetic field will precess around it at a rate proportional to the field strength and the Landé g factor. In free space, the g factor is found to be $g_0 = 2.002319314$. In much the same way that the presence of the lattice can be accounted for in the nearly-free electron model by the introduction of an effective mass, the presence of the lattice on the Zeeman splitting can be incorporated by the introduction of an effective g factor. This fact is discussed in detail in Ref. [28].

The above analysis can be repeated for arbitrary initial states and magnetic fields. We find in this case that the spin vector $\mathbf{s}(t)$ can be found by solving:

$$\frac{d\mathbf{s}}{dt} = \mathbf{\Omega} \times \mathbf{s} \tag{2.39}$$

Of course, this is precisely the classical equation, which is what Ehrenfest's theorem prescribes [18]. Though this has been derived for a single spin, this will also be the time evolution of the macroscopic magnetization of an ensemble of identical non-interacting spins.

2.6.2 Bloch equations

When there is relaxation in the system, the time evolution of the magnetization must be modified to reflect this. Though they are an approximation, the phenomenological equations proposed by Bloch provide intuition in the absence of a fully rigorous treatment of the specific nature of relaxation in the system. The Bloch equations add two new terms to the

time evolution equation for the expectation values of the spin operators found in Eqn. 2.39. First, the component of the initial magnetization which is parallel to the external magnetic field will relax towards its thermodynamic equilibrium value with a lifetime T_1, known as the longitudinal relaxation time. Here, it is assumed that the equilibrium value is that prescribed by the Maxwell-Boltzmann distribution when the spin system is in contact with a reservoir at temperature T[3]. The Bloch equations also include a term which results in a relaxation of the magnetization perpendicular to the external magnitude with a lifetime T_2, known as the transverse relaxation time. With these two terms, the vectorial form of the phenomenological Bloch equation becomes:

$$\frac{d\mathbf{s}}{dt} = \mathbf{\Omega} \times \mathbf{s} - \frac{(s_z - s_0)\hat{\mathbf{z}}}{T_1} - \frac{s_x\hat{\mathbf{x}} + s_y\hat{\mathbf{y}}}{T_2} \tag{2.40}$$

In anticipation of upcoming sections, it is useful to express the depolarization terms in tensor notation, so that the Bloch equation becomes:

$$\frac{d\mathbf{s}}{dt} = \mathbf{\Omega} \times \mathbf{s} - \overleftrightarrow{\Gamma} \cdot \mathbf{s} + \frac{s_0}{T_1}\hat{\mathbf{z}} \tag{2.41}$$

with the depolarization tensor $\overleftrightarrow{\Gamma}$ given by:

$$\overleftrightarrow{\Gamma} = \begin{pmatrix} \frac{1}{T_2} & 0 & 0 \\ 0 & \frac{1}{T_2} & 0 \\ 0 & 0 & \frac{1}{T_1} \end{pmatrix} \tag{2.42}$$

If the ensemble spins are not identical, but have some distribution of precession frequencies due to the presence of local fields, the transverse magnetization will decay more rapidly. In this case, the transverse lifetime is referred to as T_2^*, the inhomogeneous dephasing time. This type of dephasing is not irreversible, and can be reversed using a train of pulses which are resonant with the electron spin splitting [27]. Additionally, as we will see shortly, the

[3]For more details, see Sec. 4.2.3, and for a properly rigorous discussion, see Chapter 3 of Ref. [26]

decay mechanisms need not be isotropic. In the following sections, the two principle sources of depolarization of electron spins in the experiments contained within this dissertation are discussed.

2.6.3 D'yakonov-Perel relaxation

Due to the presence of the **k**-dependent effective magnetic fields, as electrons with non-zero **k** travel through the material, they will undergo precession about the internal fields. As the electrons scatter, their **k** vectors will be randomized, and so will their axes and frequencies of precession. This results in depolarization of the electron spins [29]. Figure 2.9 panel (a) shows this process diagramatically for a single electron which moves randomly. This mechanism, referred to as the D'yakonov-Perel (DP) relaxation, results in the most efficient depolarization when the momentum scattering time is long, as electrons will undergo more precession between scattering events. The DP mechanism will therefore be most efficient at low temperatures, when scattering times are longer.

In general, relaxation resulting from the DP mechanism is anisotropic [15] due to the anisotropic nature of the internal fields. In its most general form, the relaxation rate, expressed in the basis defined by [100], [010], and [001] is found to be [15, 17]

$$\overleftrightarrow{\Gamma} = \Gamma_0(v_d) \begin{pmatrix} 1+\left(\frac{\alpha}{\beta}\right)^2 & 2\frac{\alpha}{\beta} & 0 \\ 2\frac{\alpha}{\beta} & 1+\left(\frac{\alpha}{\beta}\right)^2 & 0 \\ 0 & 0 & 2\left(1+\left(\frac{\alpha}{\beta}\right)^2\right) \end{pmatrix} \tag{2.43}$$

where Γ_0 is a constant which depends on the electron drift velocity, and α and β are the Rashba and linear Dresselhaus spin-orbit field coefficients, respectively. This tensor is diagonalized by a rotation into the basis defined by [110], [1$\bar{1}$0], and [001], where it becomes:

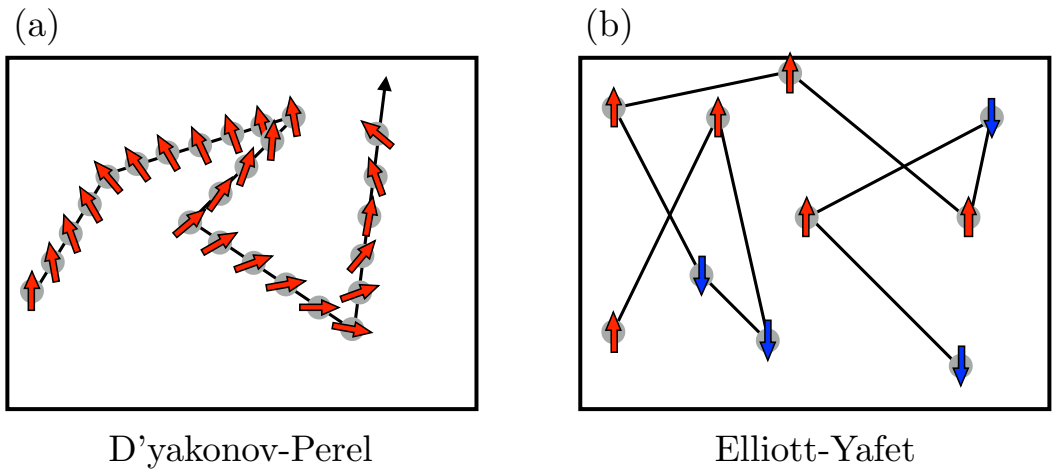

Figure 2.9: Diagramatic representations of the D'yakonov-Perel (left) and Elliott-Yafet relaxation mechanisms. Figures based on those found in Ref. [30].

$$\overleftrightarrow{\Gamma} = \Gamma_0(v_d) \begin{pmatrix} (1+\frac{\alpha}{\beta})^2 & 0 & 0 \\ 0 & (1-\frac{\alpha}{\beta})^2 & 0 \\ 0 & 0 & 2\left(1+\left(\frac{\alpha}{\beta}\right)^2\right) \end{pmatrix} \tag{2.44}$$

While the fact that the decay is anisotropic is easily handled by the tensor notation used here, it significantly complicates the analysis and typically precludes analytical solutions to Eqn. 2.41 except in simple situations. Of particular importance is that, even in the absence of precession, an initial polarization which does not lie along one of the principle axes of the decay tensor will end up rotating as it decays. It therefore significantly simplifies the analysis if the spin polarization always lies along these principle axes.

2.6.4 Elliot-Yafet relaxation

Because of the spin-orbit coupling within these samples, the energy eigenstates will no longer be precisely $|\uparrow\rangle$ and $|\downarrow\rangle$, but will instead consist of admixtures of these states which are coupled to the orbital state of the electron. The spin states therefore must instead be considered to be pseudo-spin states. Because of the spin state mixing, there is a non-zero probability that the electron spin will flip at a scattering event. This is the Elliott-Yafet (EY)

mechanism, named after its discoverer Elliott [31] and Yafet, who calculated its temperature dependence [32]. This process is shown in Fig. 2.9 panel (b).

The spin flip probability is expected to be independent of the momentum relaxation time and initial and final electron momenta. As a result, the more frequently scattering events occur, the faster depolarization occurs. That is, the depolarization time scales directly with the momentum scattering time. This stands in contradiction to the DP mechanism, whose depolarization time scales as the inverse of the momentum scattering time. Additionally, the EY relaxation leads to isotropic depolarization which does not require the tensor formalism. Since the mobility is related to the momentum scattering time, generally speaking materials with high mobility will have spin relaxation which is dominated by the DP mechanism, while low mobility samples will have relaxation dominated by the EY mechanism. Measurements suggest that the transition from DP to EY mechanisms in GaAs occurs at a doping density of about 2×10^{16} cm^{-3}. In the InGaAs samples used here, which are doped at 3×10^{16} cm^{-3}, we expect both mechanisms to contribute. Measurements first published in Ref. [8] suggest that there is a component of electron spin polarization which is anisotropic, indicating that the DP mechanism is indeed present.

2.7 Current-induced spin polarization

In 2004, Kato *et al.* showed that driving a current in InGaAs results in a dynamical polarization of conduction band electrons [33]. A current along [110] and [1$\bar{1}$0] was shown to result in the generation of an in-plane spin polarization parallel to the internal fields on a time-scale of picoseconds. These spins were then rotated out of the plane by the application of an external magnetic field in the Voigt geometry, and the steady state out-of-plane current-induced spin polarization(CISP) was detected via Faraday rotation. In the following years, experiments would demonstrate CISP in other non-magnetic semiconductors, including ZnSe [34] and GaN [35]. The spin Hall effect and CISP were later mapped in a 2DEG [36]

The fact that the spins align along the internal magnetic fields and not the vector sum of

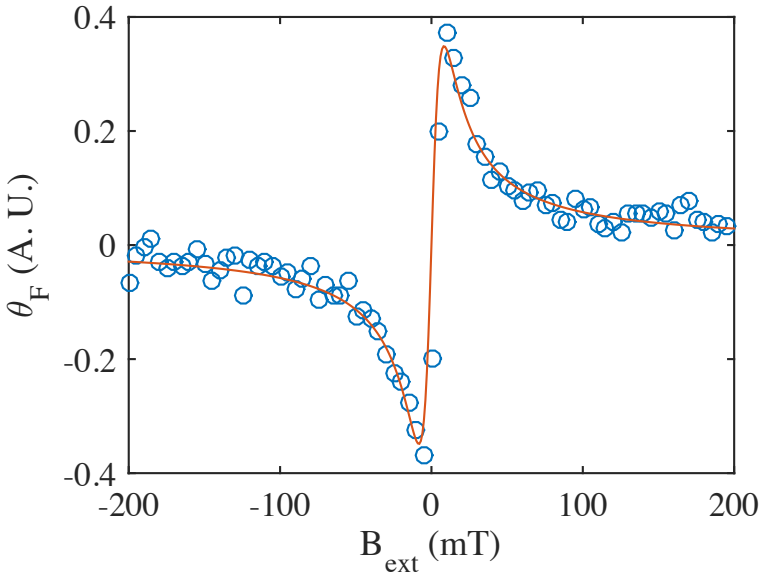

Figure 2.10: Faraday rotation angle θ_f measured as a function of the external magnetic field strength (blue circles) and a fit to Eqn. 2.45 (red trace). A constant offset has been subtracted for clarity.

the internal and external magnetic fields indicates that CISP must result from a dynamical process. The results of theoretical work suggested CISP should be directly related to the strength of the internal magnetic fields [37, 38]. Surprisingly, recent measurements have shown this to be incorrect in the case of InGaAs [8, 17]. In fact, in all cases, a negative differential relationship was observed between the strength of the internal fields and the CISP efficiency as the current direction is rotated at a single location on the sample.

A typical measurement demonstrating CISP is shown in Fig. 2.10. Here, there is no optical pumping of spin polarization. As the magnetic field is scanned, the Faraday rotation generates an odd Lorentzian lineshape. This behavior can be understood as resulting from a continual alignment of spins in the plane perpendicular to the external magnetic field which then precess at the Larmor frequency Ω_L and decay with a lifetime T_2^*. The total steady-state $\hat{\mathbf{z}}$ component of the spin polarization s_z is then given by an integral over all time of

the resulting signal:

$$s_z = \int_0^\infty \gamma \exp(-t/T_2^*) \sin(\Omega_L t) dt = \theta_{el} \frac{\Omega_L T_2^*}{1 + (\Omega_L T_2^*)^2} \tag{2.45}$$

where γ is the alignment rate and θ_{el} is the steady-state in-plane polarization resulting from CISP absent an external magnetic field, given by γT_2^*. A fit to this equation is included in Fig. 2.10 (red trace). Data were taken on sample 050331B2-N at 30 K with an in-plane electric field of 35 V/cm. The spin alignment rate γ for a particular sample and current orientation is found to scale linearly with the electron drift velocity, and the constant of proportionality η, defined by $\gamma = \eta v_D$, is used as a measure of the strength of CISP [8, 33].

Further measurements of CISP found in [8] indicate that, while the alignment of electrons by CISP is always parallel to the internal magnetic fields, the steady state polarization in the presence of anisotropic decay need not be. If CISP is generated along one of the principle axes of the decay tensor, however, the steady-state polarization will be parallel to the alignment vector. As previously discussed, the decay tensor is diagonalized in the basis defined by [110], [1$\bar{1}$0], and [001]. Rather conveniently, along these axes it is also the case that the sum of the internal fields for current along [110] will be parallel or antiparallel to [1$\bar{1}$0] and vice versa. This fortunate fact significantly simplifies the interpretation of measurements of DNP resulting from CISP found in Chapter IV.

The presence of CISP can be modeled phenomenologically with the Bloch equations by the addition of a driving term $\boldsymbol{\gamma}$, which has units of spins per unit time. With the addition of this term, we have now completed the Bloch equations which govern electron spin dynamics observed in the experiments presented here:

$$\frac{d\mathbf{s}}{dt} = \boldsymbol{\Omega} \times \mathbf{s} - \overleftrightarrow{\Gamma} \cdot \mathbf{s} + \frac{s_0}{T_1} \hat{\mathbf{z}} + \boldsymbol{\gamma} \tag{2.46}$$

2.8 Integrated photonic devices based on CISP and TRFR

As fiber optics and integrated photonic devices proliferate, a perennial challenge has been the implementation of integrated non-reciprocal elements such as isolators and circulators [39, 40, 41, 42, 43, 44, 45, 46]. The challenge exists in the fact that these non-reciprocal devices must break time reversal symmetry of the propagation of light. This typically means magneto-optic effects are required. In Ref. [47], we propose to use the Faraday rotation generated by CISP in integrated photonic devices. In a single-mode waveguide, Faraday rotation results in a non-reciprocal coupling between the TE and TM modes. By controlling the strength of Faraday rotation, the coupling strength can be controlled. Control over the propagation mode can be used in conjunction with, for instance, integrated mode-dependent couplers or various interferometric techniques to form isolators, circulators, and modulators. Faraday rotation resulting from CISP has the advantage that it can be controlled electrically and does not require an external magnetic field.

There are two primary challenges to designing devices based on this operating principle. The first of these challenges is that the Faraday rotation resulting from a spin polarized conduction band occurs, by necessity, near the absorption edge. Accordingly, material absorption is of concern. A figure of merit, defined by the ratio of the amount of Faraday rotation that occurs per unit length divided by the absorption per unit length, is used as a measure. This figure of merit was measured for Faraday rotation generated by CISP as a function of wavelength near the band gap using the Faraday rotation techniques discussed above. First, the Faraday rotation angle resulting from CISP per applied electric field is measured and fit to extract θ_{el}, which is plotted versus laser wavelength in Fig. 2.11. Then, material absorption is measured by comparing the power transmitted through the InGaAs epilayer and substrate to the transmission through the substrate alone. The sample design used is shown in Figs. 4.2 and 4.3, the details of which will be discussed there. Here, samples of the "L" design are used, with current driven along the $[1\bar{1}0]$ direction.

At the highest applied voltages used, the figure of merit was found to have a maximum

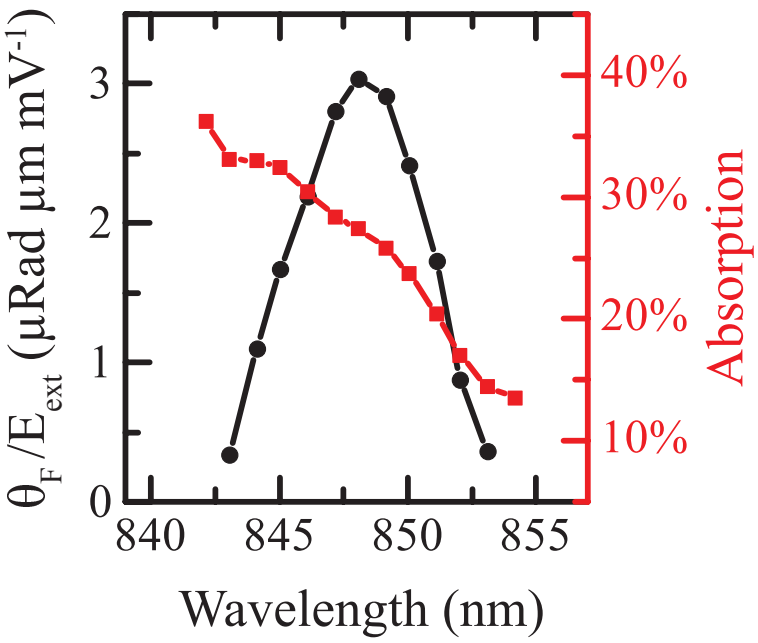

Figure 2.11: Absorption (red) and Faraday rotation per applied electric field (black) versus wavelength measured in transmission mode at 30 K.

value of 7.73×10^{-6}. This low value is far below that achieved using other means, but does have the advantage that it can be electrically controlled. Recent work on Faraday rotation in microcavities [48] and ring resonators [49] suggest that this problem might be avoided by tuning the laser further below the absorption edge and relying on high quality factor cavities to boost the Faraday rotation angle.

The second challenge lies in the fact that for successful mode conversion in a waveguide, the TE and TM modes must have degenerate phase velocities [50]. Accordingly, the waveguide structure must be carefully engineered so that these phase velocities match. In the presence of birefringence, the normalized intensity of light I in an undriven mode which is coupled to a driven mode with initial intensity I_0 is given by:

$$\frac{I}{I_0} = \frac{4}{4 + (\Delta/k)^2} \sin^2 \left(\frac{1}{2} [4 + \{\Delta/k\}^2]^{1/2} kz \right) \tag{2.47}$$

where k is the mode coupling constant, Δ is the mismatch in phase velocities, $k_{TE} - k_{TM}$, and z is the position along the waveguide in the direction of propagation. The maximum

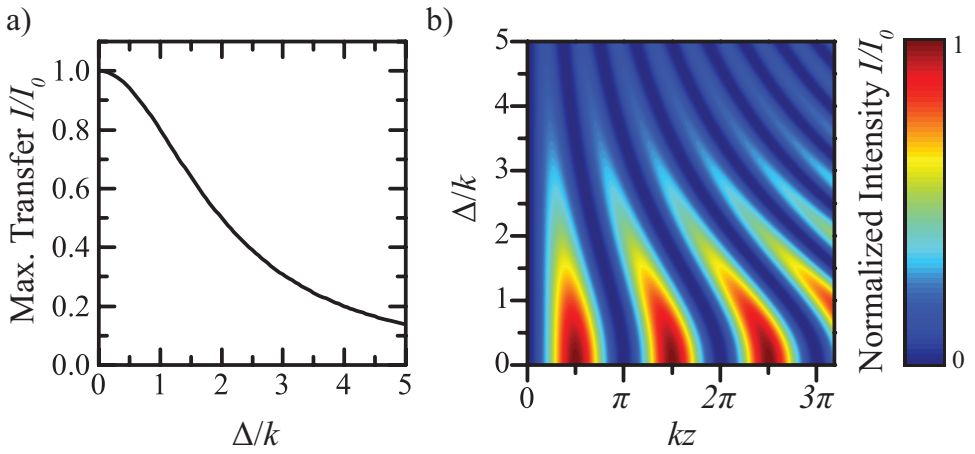

Figure 2.12: a) Maximum normalized power transfer between modes as a function of Δ/k. A power transfer of 95% requires $\Delta/k < 0.459$. b) Intensity in an undriven mode coupled to a driven mode at rate k, with phase velocity splitting Δ, plotted as a function of dimensionless parameters Δ/k and kz, where z is the position along the waveguide.

achievable fractional power transfer is plotted in Fig. 2.12 a) as a function of Δ/k. Fig. 2.12 b) shows Eq. 2.47 plotted as a function of the dimensionless parameters kz and Δ/k.

CHAPTER III

Time-resolved Faraday/Kerr rotation measurements

In this chapter, time-resolved Faraday rotation (TRFR) measurement techniques which are used throughout the following chapters are presented. TRFR is a pump-probe measurement technique that allows spin dynamics to be investigated with a temporal resolution of a few picoseconds. This level of resolution is achieved by controlling differences in optical path length, so that the shortest resolvable time step is set by the precision with which a mechanical delay line can be positioned. In the following sections, the optical apparatus, laser system, modulation and signal processing scheme, as well as other crucial systems for performing TRFR measurements will be discussed.

3.1 TRFR measurement apparatus

Figure 3.1 shows an overview of the optical system used in TRFR measurements. In this section, the beam path will be described and the important components along the way are discussed. Labels in Fig. 3.1 are referred to throughout the following section when discussing the beam path.

The sample is placed in a Janis ST-300 (transmission) or ST-500 (reflection) helium flow cryostat which maintains a constant temperature within the range of 5 K to room temperature. A thermocouple is used to monitor the sample temperature, which is maintained at a constant value by way of an ohmic heater and PID controller. The cryostat is placed

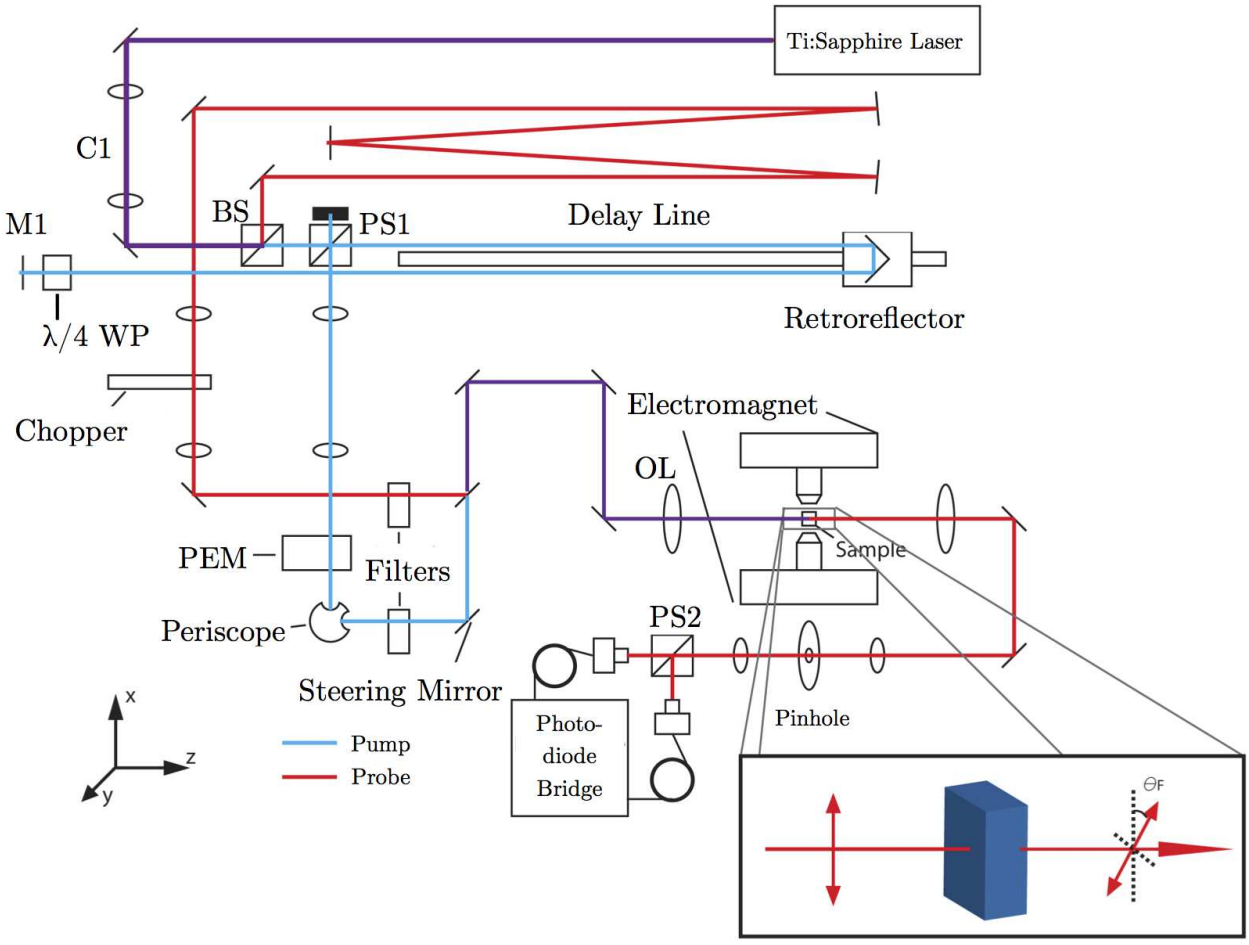

Figure 3.1: Overview of the optical beam path used in TRFR measurements.

between the poles of an electromagnet which, with the addition of a chilled liquid cooling system, can sustain a field strength of 300 mT at ambient temperature and full duty cycle. Current is driven by a Kepco voltage-controlled current source capable of driving 8 A at up to 40 V, and the set voltage is generated by an auxiliary DAC channel on one of the lock-in amplifiers used in these experiments.

3.1.1 Laser system

We start with the laser system. Optical pulses with a duration of a few picoseconds are generated by means of mode-locking using a Coherent MIRA 900 titanium sapphire laser. The exceptionally wide gain bandwidth (spanning approximately 700-1000 nm) provided by the Ti:sapphire crystal allows for a very large number of simultaneous cavity modes. Mode-locking is achieved by enforcing a phase relationship between some subset of these modes which leads to brief intense pulses when all modes constructively interfere followed by a (relatively) long period during which the modes destructively interfere and no light is emitted. When this phase relationship between the modes is established, the laser is said to be mode-locked. The laser uses a combination of passive Kerr lensing in the Ti:Sapphire crystal and a sophisticated servo loop to initiate and maintain mode locking and control group velocity dispersion in the cavity. In the best-case scenario, the minimum achievable pulse duration is limited by the bandwidth of cavity modes which are successfully mode-locked. In practice, the pulse times are rather longer than the linewidth would suggest, usually due to dispersion in the optical setup. The repetition rate of the laser is set by the total cavity length, which in our case leads to a repetition time of 13.158 ns, or a pulse frequency of 76 Mhz. The MIRA system used here can operate in two modes, somewhat deceptively labeled picosecond mode and femtosecond mode. In picosecond mode, pulse times are approximately 5 picoseconds, while in femtosecond mode pulses of approximately 150 femtoseconds are possible if the laser is well calibrated. The Ti:sapphire crystal in the MIRA 900 is optically pumped by a 10 watt 532 nm beam generated by a Coherent Verdi

V10 laser system. A diode laser emitting at 1064 nm is frequency-doubled to 532 nm in a non-linear crystal composed of lithium triborate to generate the pump beam. When the laser is operating optimally, an average output power of around 2 watts is possible when the pulse center frequency is tuned within the range of 830–850 nm.

3.1.2 Optical beam path

With our optical pulses successfully formed, the beam first passes through a lens pair, labeled C1 in Fig. 3.1, which collimates the beam. It then travels to a beam splitter (BS) which splits the beam into two components. The reflected portion becomes the probe beam (red) and the transmitted component becomes the probe beam (blue). We start by following the pump beam, which immediately passes through a polarizing beam splitter (PS) oriented so that on the first pass the light is fully transmitted. It then enters the delay line, which consists of a retroreflector mounted to a cart which moves along a high-precision guide rail. Light travels down the rail and is reflected back, offset by a small amount such that on the return trip it misses the polarizing beam splitter. It then passes through a quarter wave plate ($\lambda/4$), reflects off a mirror (M1) back along its path, and then passes through the quarter wave plate again. When the beam is reflected off M1 its helicity is reversed, so that after the second pass through the quarter wave plate it is traveling back down the delay line with a polarization orthogonal to its original polarization if the quarter wave plate is properly oriented with respect to the incident polarization. It hits the retroreflector again, and then the polarizing beam splitter. Since the beam travels the full length of the delay line twice, this is referred to as a double-pass delay line. The position of the retroreflector can be moved by about 70 cm, so that the total optical path length changes by 2.8 m. We can therefore adjust the time it takes the pump pulse to travel to the sample by about 9 ns. Now, the beam is fully reflected by the polarizing beam splitter. The fact that we have intentionally sent the beam back along its original path can sometimes lead to difficulty maintaining mode locking, as the reflected beam can upset the mode-locking process if it is coupled back into

the laser cavity. The pump beam then passes through a photo-elastic modulator (PEM). This component modulates the incoming beam so that the transmitted beam oscillates from left to right circular polarization at 50 kHz. The PEM serves two purposes in our experiment; first, it allows for lock-in detection methods to be used. Second, by modulating the helicity of the probe beam, the time-averaged injected spin polarization is zero. This prevents the inadvertent introduction of a nuclear polarization due to direct optical pumping. The beam is then filtered to limit the incident pump power. The beam then reflects off a computer-controlled steering mirror which is used to systematically adjust the overlap of the pump and probe beams on the sample. The pump and probe beams are then recombined, pass through a set of manual steering mirrors, and are focused by an objective lens (OL) onto the sample.

When compared to the pump beam path, the probe beam path is relatively simple. After being split off at the first beam splitter (BS), it is reflected off a set of mirrors which are there to roughly equalize the optical path lengths of the probe beam and the pump beam when it is near its maximum path length. The length of this compensating path determines the range of pump-probe delay times Δt that can be obtained. We typically set this so that the delay range can be adjusted over the range $\Delta t = -1$ to 8 ns. Here, negative delays indicate that the probe beam arrives before the pump. The probe beam is then focused onto an optical chopper used for lock-in detection. It is then filtered, passes through the same set of steering mirrors as the probe, and is focused by the objective lens onto the sample. In Fig. 3.1, the transmitted component of the probe beam is collected, however in some situations it is advantageous to collect the reflected portion of the probe beam instead. The latter case is termed Kerr rotation, while the former is known as Faraday rotation. The collected probe beam is then focused on a pin hole which is used to filter out as much of the scattered pump beam as possible. It then is rotated in a half-wave plate and hits a polarizing beam splitter. The half wave plate is used to adjust the polarization of the probe beam so that it is evenly split at (PS2). A photodiode bridge is then used to measure the difference between

the intensities reflected in each direction. The difference in intensities in each arm can be related to the Faraday rotation which results from electron spin polarization by:

$$\sin(2\theta_f) = \frac{I_A - I_B}{I_A + I_B} \tag{3.1}$$

In most situations, the exact magnitude of the Faraday rotation angle is not required. In this case, we measure only $I_A - I_B$. Also, since the Faraday rotation we typically measure is very small (10-100 μRad), it is sufficient to use the small angle approximation $\sin(2\theta_f) \approx 2\theta_f$. We then report the measured signal in arbitrary units. The internal circuitry of the photodiode bridge results in a gain factor of 2 on the $I_A - I_B$ output relative to the I_A and I_B outputs which must be included if exact rotation angles are desired.

3.1.3 Lock-in measurements

As previously mentioned, we take advantage of lock-in techniques to improve the signal to noise ratio in these measurements. At its most basic level, a lock-in amplifier is used to isolate the component of the input signal that is modulated at a known reference frequency. For instance, the probe beam is chopped at a frequency of 1157 Hz, while the pump beam and room lights are not. By isolating the component of the measured signal which is modulated at the chopper frequency, we can effectively reject noise due to pump scatter and room lights. This allows for the small but notable creature comfort of working with the lights on. In our setup, we use two cascaded lock-in amplification steps which isolate the component of the measured signal which is modulated at both the PEM frequency *and* the chopper frequency. We typically see a large improvement in the SNR when using this cascaded technique. Care must be used when selecting the lock-in time constants. This time constant (or rather, its inverse) is used to set the cutoff frequency for a high-order Butterworth low-pass filter which is applied to the fast-x output. Accordingly, the time constant on the first lock-in must be less than the inverse of the reference frequency used in the second lock-in. Further details of

lock-in measurement techniques are presented in Ref. [28].

3.2 Time-resolved Faraday rotation data

In this section, typical TRFR measurement data will be presented. We start by consider Eqn. 2.46, reproduced here:

$$\frac{d\mathbf{s}}{dt} = \mathbf{\Omega} \times \mathbf{s} - \overleftrightarrow{\Gamma} \cdot \mathbf{s} + \frac{s_0}{T_1}\hat{\mathbf{z}} + \boldsymbol{\gamma} \tag{3.2}$$

We now make the following simplifications:

1. Omit CISP, so that $\boldsymbol{\gamma} = 0$.
2. Set the external magnetic field to be parallel to $\hat{\mathbf{x}}$, so that $\mathbf{B} = B_0\hat{\mathbf{x}}$ and $\mathbf{\Omega} = \Omega\hat{\mathbf{x}}$.
3. Assume the spin depolarization tensor $\overleftrightarrow{\Gamma}$ is isotropic, so that $\overleftrightarrow{\Gamma} = \frac{1}{T_2^*}\,\mathbb{1}$ where $\mathbb{1}$ is the identity matrix.
4. Assume that the equilibrium electron spin polarization s_0 is zero.
5. Take the inital spin polarization to be $\mathbf{s}(0) = s_0\hat{\mathbf{z}}$.

Only the third simplification requires justification. In general, we do expect the decay to be anisotropic. However, if the precession frequency Ω is much faster than the decay rates and the precession occurs around one of the principle axes of the decay tensor, we can account for the anisotropic decay by using the average of the decay times along the $\hat{\mathbf{x}}$ and $\hat{\mathbf{y}}$ axes [51]:

$$\frac{1}{\Gamma_{\text{eff}}} = \frac{1}{2}\left(\frac{1}{\Gamma_{xx}} + \frac{1}{\Gamma_{yy}}\right) \tag{3.3}$$

At the lowest field (50 mT) and highest temperature (50 K) used in these experiments, the precession frequency exceeds the decay rate by an order of magnitude. This is sufficient

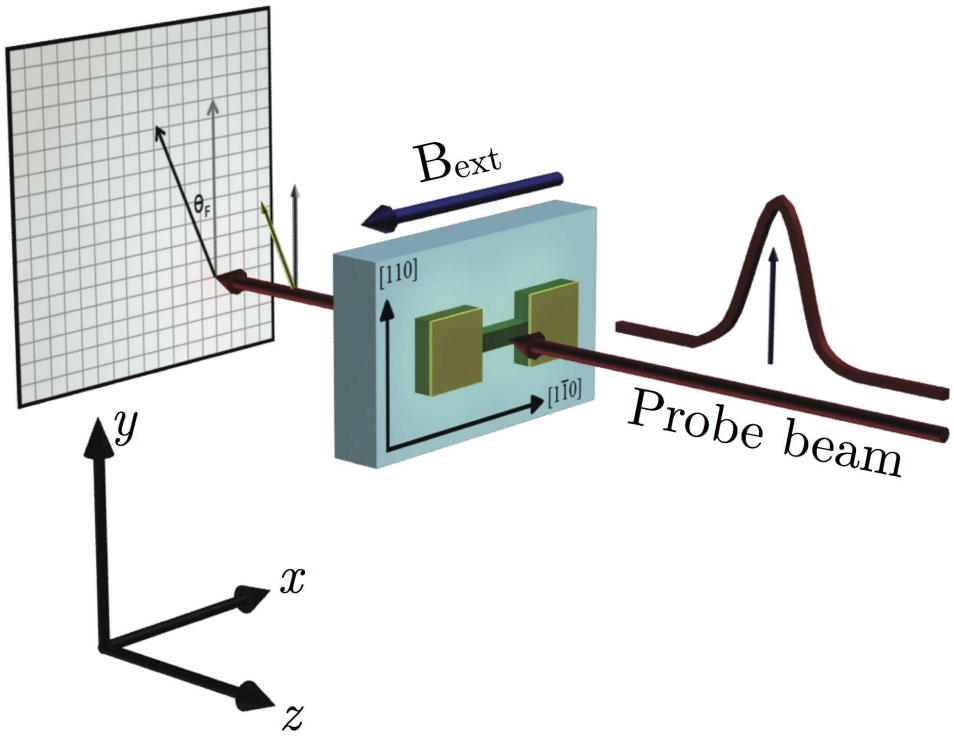

Figure 3.2: Geometry of a typical TRFR measurement.

to justify using this simplification. If the precession frequency is not parallel to any eigenvectors of the decay tensor there can exist some spin polarization along $\hat{\mathbf{x}}$, but the TRFR measurements used cannot detect this polarization.

With the above simplifications, assumptions, and initial conditions, Eqn. 3.2 can be expressed as two first-order coupled differential equations:

$$\frac{ds_z}{dt} = s_y\Omega - s_z\Omega - \frac{1}{T_2^*}s_z \tag{3.4}$$

$$\frac{ds_y}{dt} = s_z\Omega - s_y\Omega - \frac{1}{T_2^*}s_y \tag{3.5}$$

The solutions to these equations are:

$$s_y(t) = s_0 \sin(\Omega t)e^{-t/T_2^*} \tag{3.6}$$

$$s_z(t) = s_0 \cos(\Omega t)e^{-t/T_2^*} \tag{3.7}$$

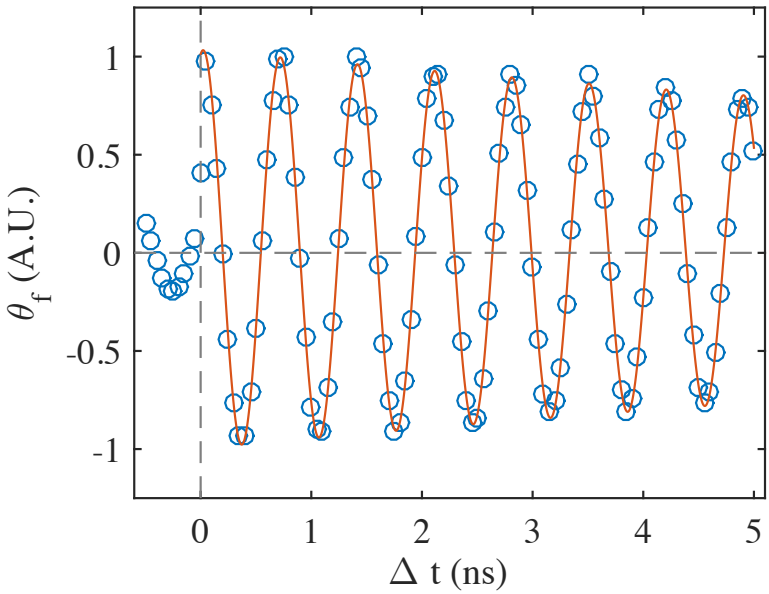

Figure 3.3: Normalized Faraday rotation (A.U.) versus pump-probe delay time Δt. Experimental data (blue circles) taken on sample 050331B3-4A at 30 K with external magnetic field of 200 mT. Data are fit to Eq. 3.8, which gives $T_2^* = 12$ ns and $g = 0.5029(3)$ (red line).

Consider the experimental geometry shown in Fig. 3.2. At time $t = 0$, a circularly polarized probe pulse traveling in the $-\hat{\mathbf{z}}$ direction is incident on the sample, which excites a spin polarization $\pm s_0$ along $\hat{\mathbf{z}}$ with the sign set by the helicity of the beam, as discussed in Sec. 2.4.2. The Faraday rotation signal observed will be proportional to the $s_z(t)$, whose solution is given above. We therefore expect to see a time-resolved Faraday rotation signal of:

$$\theta_f = A\cos\left(\frac{g\mu_B B_0}{\hbar}\Delta t\right)\exp[-\Delta t/T_2^*] \tag{3.8}$$

where A is a constant of proportionality which relates the spin polarization to the Faraday rotation angle. Data taken on sample 050331B3-4A at 30 K with an external magnetic field of 200 mT is shown in Fig. 3.3 (blue circles) along with results of a fit to Equation 3.8[1] The sample used consists of a 500 nm layer of $In_{0.04}Ga_{0.96}As$ which is silicon doped at a concentration of $n = 3 \times 10^{16}$ cm^{-3} grown atop a semi-insulating GaAs substrate. Results of the fit give a g factor of -0.5029(3) and lifetime $T_2^* = 12$ ns. These fits tend to give very

[1] A constant term has been added to the fitting equation to account for a small offset typically seen in our measurements, and the fit has been restricted to data at $\Delta t \geq 150$ ps to avoid contributions from remaining optical carriers at short delay times.

good measures of the g factor, but can exhibit large uncertainty in the fit to the lifetime when it is long compared to the accessible delay range. For spin lifetimes which are long compared to the laser repetition time, the technique of resonant spin amplification (RSA) is frequently used [51, 52, 53]. In RSA measurements, Δt is fixed to a small negative value and the magnetic field is swept.

When the lifetime is comparable to the repetition rate of the laser (13.158 ns in our case), the spin polarization from the previous pulse has not completely decayed by the time the next pulse arrives. This is the case in Fig. 3.3, as evidenced by the Faraday rotation signal at negative delays. In this situation, we must take into account the contribution to the Faraday rotation from all previous pulses. The resulting sum over all previous pulses becomes:

$$s_{\hat{z}} = \sum_{n \geq 0} S_0 \cos\left(\Omega_L(\Delta t + nT_{\text{rep}})\right) \exp\left[-\frac{(\Delta t + nT_{\text{rep}})}{T_2^*}\right] \tag{3.9}$$

Chapter V is devoted to understanding the effects on the expected TRFR signal when the lifetime is on the order of, or larger than, the laser repetition rate. This correction has important implications with regard to measurements of dynamic nuclear polarization, which are presented in the following chapter.

CHAPTER IV

Current-induced dynamic nuclear polarization

4.1 Introduction

In addition to the electron spin system, the lattice nuclei in the materials with which we work possess spin angular momentum and a concomitant magnetic dipole moment. These nuclear spins, though they carry a dipole moment which is only 5 parts in 10,000 that of the electrons, and are generally considered to be well isolated from the environment, nevertheless interact with the electron spin system through the hyperfine mechanism. This interaction leads to a rich set of static and dynamical effects.

The static effect of the hyperfine coupling was first experimentally demonstrated by Knight in 1949, where a shift in the nuclear magnetic resonance (NMR) frequency in metals was observed which resulted from paramagnetic polarization of the conduction electron spins [54].

In 1953, Overhauser proposed that, through the hyperfine coupling, electron spins which are held out of thermodynamic equilibrium through some means of pumping should result in a hyper-polarization[1] of nuclei as the electrons attempt to thermalize through their coupling to the nuclear spin system [55]. Overhauser predicted that in experimental conditions which support a paramagnetic electron spin polarization due to the Zeeman splitting, depolarizing

[1] A condition of hyperpolarization is said to occur when the polarization of the nuclei is much larger than the paramagnetic susceptibility would predict given the experimental conditions

the electrons by saturating the electron spin resonance would result in a strong nuclear polarization. This effect was quickly experimentally verified by Carver and Slichter [56]. In fact, the experimental verification, performed by colleagues of Overhauser at the University of Illinois in Urbana, was performed so quickly that its publication preceded by two weeks the publication of the theory upon which it was based.

Rather surprisingly, the first demonstration of optical orientation of electron spins in a semiconductor was performed in silicon, whose indirect band gap significantly complicates the use of the optical detection methods which are typically relied upon [57]. Instead, the presence of an electron spin polarization was determined by its effect on the nuclear spin system, and in particular by detecting shifts in the nuclear magnetic resonance frequency.

In the late 1960's and early 1970's, optical spin pumping in GaAs was pioneered, where the direct band gap and favorable selection rules allowed spin polarization to be detected by monitoring the polarization of photoluminescence [21, 22, 58]. In these early measurements the role of the nuclei was ignored. Ekimov and Safarov performed the first optical measurements which showed behavior originating from nuclear spin polarization [22]. Further measurements showed that the polarized nuclei result in a magnetic field about which the electron spins precess [59, 60, 61]. These experiments were placed on a firm theoretical footing by Paget in 1977, where the effect of the nuclear magnetic field on the Hanle depolarization of the electron spin polarization was predicted and measured [62].

Since this pioneering work, dynamic nuclear polarization has been demonstrated by generating a non-equilibrium electron spin polarization by optical pumping [57, 62, 63, 64], ferromagnetic imprinting [65], electrical spin injection from a ferromagnet [66, 67], and in a spin-polarized Landau level [68, 69].

The nuclear spin system in semiconductors has attracted interest for potential applications in classical and quantum spin-based computation schemes [66, 70, 71]. Its isolation from the surrounding environment yields exceptionally long coherence times, which can be as much as nine orders of magnitude longer than electron spin coherence times [63], and

suggests use as an intermediate timescale data storage mechanism [72].

In this chapter, I will explore the role of the nuclear spin system in the context of current-induced electron spin polarization (CISP), discussed in the previous chapter. Previous measurements of DNP resulting from CISP have been performed in GaAs, where nuclear polarization was detected by means of NMR spectroscopy [73, 74]. These experiments are complicated by their chosen detection method; in order for NMR measurements to be carried out, a relatively large sample is required. Because of this, the current density which drives CISP must be severely limited to prevent ohmic heating within the samples. These measurements were performed with current densities up to 4 A·cm^{-}2. Additionally, these measurements fail to account for the anisotropic nature of CISP due to the direction of current flow with respect to the crystal structure.

In contrast, the optical detection methods utilized here allow for current densities which are 3 orders of magnitude larger with minimal heating. Also, through the use of devices fabricated with patterned channels and contacts, the directionality of CISP and the resulting DNP can be studied in detail for current in the plane normal to the [001] crystal axis.

This chapter will start with an overview of the salient features of the nuclear spin system in GaAs and its coupling to the electron spin system. Measurements of DNP resulting from CISP which are carried out by direct detection of the nuclear magnetic field by Larmor magnetometry are then presented. Through these measurements, we find competing alignment mechanisms which depend on the magnitude of the in-plane electric field but not its direction. Our results are broadly consistent with previous experimental and theoretical work. These measurements lead us to the discovery of a previously undescribed phase shift in TRFR scans, detailed in the next chapter, which complicate matters. The implications of this complication are discussed, and found to leave the major results unchanged. Finally, further measurements are suggested which would clarify aspects of the results presented here. This chapter is broadly based on work first published in Ref. [75].

4.2 Nuclear spin system in GaAs

Because nuclei are composite particles made up of numerous spin-1/2 nucleons, the total spin, typically given the symbol I, will vary from species to species. In general, it is not readily apparent what the total spin of the nucleus should be since the usual process of determining the spin of composite particles yields many possibilities. Determining the total spin of a nuclear species is generally a matter left to experiment, but rules have been empirically discovered which allow for some knowledge of what to expect. Of course, since all nucleons are spin-1/2, if there are an odd number of nucleons the nuclei must have a half-integer spin, while an even number of nucleons must yield a nucleus with integer spin. It has additionally been discovered that if both the total number of protons and neutrons are individually even, then the nucleus will have spin 0. Beyond these guidelines, nuclear spins are determined experimentally.

In quantum theory, we treat the angular momentum $\mathbf{L}$, and its dimensionless operator $\mathbf{I}$ defined by $\mathbf{L} = \hbar\mathbf{I}$, as vector operators which act on the spin state of the nucleus. In the usual way, the eigenvalue of $\mathbf{I}^2$ for a particular species is $\mathbf{I}^2|\psi\rangle = \hbar^2 I(I+1)|\psi\rangle$. The projection of the angular momentum onto the chosen axis of quantization, taken to be $\hat{z}$, commutes with the total angular momentum operator $\mathbf{I}^2$, so that both may be known simultaneously, and takes on eigenvalues $\mathbf{I}_z|\psi\rangle = m\hbar|\psi\rangle$ where m is any of the $2I+1$ integer or half-integer values contained within I, $I-1$, $I-2$, ..., $-I$.

Associated with the spin angular momentum is a magnetic dipole moment, given by:

$$\boldsymbol{\mu} = \gamma\hbar\mathbf{I} \tag{4.1}$$

where γ is known as the gyromagnetic ratio. For nuclear spins, the gyromagnetic ratio is

typically quoted in terms of the nuclear magneton, which is defined by:[2]

$$\mu_N = \frac{e\hbar}{2m_P} \approx 3.152\ 451\ 2605(22) \times 10^{-8}\text{eV T}^{-1} \tag{4.2}$$

The large mass of the proton when compared to that of the electron means that the nuclear dipole moments are smaller than the electron moment by a factor of roughly $m_e/m_p \approx 5 \times 10^{-4}$

Neglecting impurities and the low concentration of silicon dopants present in the $In_{0.04}Ga_{0.96}As$ samples we focus on here, there are 5 principal nuclear species present, corresponding to the isotopes of indium, gallium, and arsenic which have appreciable natural abundances. The spins, natural abundances, relative dipole moment, and resonance frequency per Tesla of these species are shown in Table 4.1.

Nuclear Species	Isotopic NA	I	μ/μ_N	ν/B (MHz·T^{-1})
^{69}Ga	60.11%	$\frac{3}{2}$	2.01659	10.248
^{71}Ga	39.89%	$\frac{3}{2}$	2.56227	13.021
^{75}As	100%	$\frac{3}{2}$	1.43947	7.315
^{113}In	4.3%	$\frac{9}{2}$	5.5289	9.365
^{115}In	95.7%	$\frac{9}{2}$	5.5408	9.386

Table 4.1: Properties of the primary constituent nuclei present in the $In_{0.04}Ga_{0.96}As$ considered in this chapter [76].

In general, the nuclear spin system is remarkably well isolated from the environment, which leads to longitudinal relaxation times that can be on the order of seconds to days [26]. This long relaxation time complicates measurements of nuclear spins, but suggests that the nuclear spin system might be useful as a means of storing classical information, recorded in the spin orientation of an ensemble of nuclear spins, as mentioned in the introduction to this

[2]Value obtained in CODATA recommended values of the fundamental physics constants: 2010 published by NIST

chapter.

4.2.1 Dipole-dipole coupling

We first consider the contribution to the total nuclear spin Hamiltonian resulting from the dipole-dipole coupling of nuclear spins. For two spins with magnetic moments $\boldsymbol{\mu}_1 = \gamma_1 \hbar \mathbf{I}_1$ and $\boldsymbol{\mu}_2 = \gamma_2 \hbar \mathbf{I}_2$, the contribution to the Hamiltonian of spin 2 due to the field resulting from spin 1 is found to be:

$$\mathscr{H}_{12} = -\boldsymbol{\mu}_2 \cdot \mathbf{H}_{12} \tag{4.3}$$

where $\mathbf{H}_{12}$ is the field at spin 2 due to the dipole moment of spin 1, and is given by the familiar equation:

$$\mathbf{H}_{12} = \frac{1}{r_{12}^3} \left\{ \frac{3\mathbf{r}_{12}(\boldsymbol{\mu}_1 \cdot \mathbf{r}_{12})}{r_{12}^2} - \boldsymbol{\mu}_1 \right\} \tag{4.4}$$

Here, $\mathbf{r}_{12}$ is the displacement vector between nuclei 1 and 2 and r_{12} is its magnitude. The spin precession time of spin 2 in the field due to spin 1 sets the time-scale for relaxation within the nuclear spin system. In the InGaAs material on which we focus, this local field is of the order of a few Gauss, corresponding to a transverse dephasing time T_2 on the order of 10^{-3} to 10^{-4} seconds in the absence of an external magnetic field.

In the presence of an external field, the role of the dipole-dipole coupling becomes somewhat more complicated. Consider first the behavior of spin 1 neglecting any dipole-dipole couplings. Its dipole moment will precess around the external magnetic field, so that the component of the dipole moment that is longitudinal to the external field will remain constant while the transverse component rotates at the Larmor frequency. This can result in a component of $\mathbf{H}_{12}$ at the location of spin 2 that is rotating at the Larmor frequency of spin 1. Both the static and rotating components of $\mathbf{H}_{12}$ result in relaxation. However, if these spin species are the same, the rotating portion of the field will be resonant with spin 1 and can therefore have a large effect on the magnetization of spin 1 even if the coupling is weak. This interaction is suppressed when the species are different because of the lack of a

resonance condition [26].

If the external field is significantly stronger than the dipole-dipole coupling fields, relaxation due to the coupling becomes suppressed [62]. This leads to much longer T_2 times which can, in some circumstances, exceed T_1.

4.2.2 Spin temperature

The timescale T_2 established by the dipole-dipole coupling between nuclei is also the timescale at which the nuclear spin system comes to thermodynamic equilibrium. Since this timescale is much faster than the longitudinal relaxation time in the presence of an external field which is larger than the local field, the nuclear spin system can be characterized by a single parameter. This parameter is the spin temperature [26]. The spin temperature, as distinct from the lattice temperature, is arrived at by assuming that the occupation of the spin states should follow a Boltzmann distribution, and then calculating the temperature required for the observed occupation levels. This is straight forward in spin 1/2 systems, but can become more complicated for systems with nuclei of higher spin and when more than a single species is present [26]. Nevertheless, the concept of a spin temperature is frequently encountered in the literature. Because of the small splitting between nuclear spin states, even small nuclear polarizations lead to strong cooling of the nuclear spin system. In our experiments, nuclear spin temperatures on the order of 10^{-4} to 10^{-5} K are observed, despite an average nuclear spin of only a few parts in 10^4. Depolarization of the nuclei leads to a heating of the spin system, so that when the spins are fully depolarized in an external field (for instance, by saturation of the NMR frequency), the spin temperature is infinite. If the nuclei are polarized *against* the external field the spin temperature is understood to be negative. If these negative temperature spins are brought into contact with a spin bath at finite temperature, they would transfer energy to the spin bath until equilibrium is reached, thereby heating the bath. Accordingly, a negative temperature is, in essence, hotter than any system with a positive finite temperature.

4.2.3 Zeeman interaction

In the presence of an external magnetic field $\mathbf{B} = B_0\hat{z}$, the nuclear dipole moments give rise to a Zeeman-like term in the total nuclear spin Hamiltonian, given by:

$$\mathscr{H}_Z = -\boldsymbol{\mu} \cdot \mathbf{B} = -\gamma\hbar B_0 \mathbf{I}_z \tag{4.5}$$

The eigenvalues of $\mathscr{H}_Z$, corresponding to the Zeeman energies, are given by $E_m = -\gamma\hbar B_0 m$ where m is the projection of the total nuclear spin onto the $\hat{z}$ axis. Given the small magnetic moment of the nuclear spins, the energy splitting between adjacent states $|m\rangle$ and $|m+1\rangle$ is correspondingly small. For the largest nuclear moment present in our sample, ^{115}In, this splitting is found to be 5.38×10^{-8} eV $\cdot$ T^{-1}. At the largest magnetic field used in our study (200 mT), this has a corresponding thermal energy at a temperature of 125 μK.

When the external field is large compared to the field due to dipolar coupling discussed in the previous section, we can treat the nuclear spins as isolated systems which will collectively obey Maxwell-Boltzmann statistics. We may therefore calculate the fraction of nuclei in a particular state $|m\rangle$ from:

$$n_m = \frac{e^{-E_m/\beta}}{\sum_{m=-I}^{I} e^{-E_m/\beta}} \tag{4.6}$$

In this expression, β is the thermal energy $k_B T$ where k_B is the Boltzmann constant and T is the lattice temperature. The denominator is known as the partition function, usually given the symbol Z. The net magnetization M of a sample consisting of N nuclei can be found from:

$$M = N\gamma\hbar \frac{\sum_{m=-I}^{I} m e^{-E_m/k_B T}}{\sum_{m=-I}^{I} e^{-E_m/k_B T}} \tag{4.7}$$

If the energy splittings $\gamma\hbar B_0$ are small compared to the thermal energy $k_B T$, so that the argument within the exponential functions is small, it is useful to replace the exponentials

in this expression with their Taylor series expansions[3]. With $\gamma\hbar B_0/k_BT \ll 1$, we need only keep up to the linear term. Doing so yields:

$$m = N\gamma\hbar \frac{\sum_{m=-I}^{I} m(1 + m\gamma\hbar B_0/\beta)}{\sum_{m=-I}^{I} (1 + m\gamma\hbar B_0/\beta)} \tag{4.8}$$

The sum over symmetric limits means any terms that are odd in m sum to zero, leaving us with:

$$\begin{aligned} M &= \frac{N\gamma^2\hbar^2 B_0}{\beta} \left[\frac{\sum_{m=-I}^{I} m^2}{\sum_{m=-I}^{I} 1} \right] \\ M &= \frac{N\gamma^2\hbar^2 B_0}{\beta} \left[\frac{\frac{1}{3}I(I+1)(2I+1)}{2I+1} \right] \\ M &= \frac{N\gamma^2\hbar^2 B_0 I(I+1)}{3k_BT} \end{aligned} \tag{4.9}$$

Accordingly, the magnetization in the sample is proportional to the magnetic field B_0. This proportionality constant is called the static susceptibility:

$$\chi_0 = \frac{N\gamma^2\hbar^2 I(I+1)}{3k_BT} \tag{4.10}$$

That the susceptibility of the material is proportional to $1/T$ is known as Curie's law.

When a non-magnetized sample is first placed in a magnetic field each spin will precess around the field independently. The time-averaged magnetization will therefore remain zero. It is only through relaxation that a magnetization builds in the sample, and this occurs with characteristic time T_1, the longitudinal relaxation time. This relaxation happens through

[3]This is always true in our experiments; the small nuclear dipole moment means that in the fields accessible to our experiment, $\gamma\hbar B_0/k_B$ will remain in the μK range, much colder than liquid helium temperatures accessible to our experiment.

coupling to the lattice. Since this coupling is particularly weak in the nuclear spin system, relaxation is slow and, as mentioned above, T_1 times can be as long as days.

4.2.4 Quadrupolar moment

Because the nucleus is a composite particle, it will generally have a non-zero electric quadrupole moment, which in its most general form is expressed as a rank-two tensor given by[11]:

$$Q_{ij} = \int [3r_i r_j - (r)^2 \delta_{ij}] \rho(\mathbf{r}) d\tau \tag{4.11}$$

The electric potential due to this qaudrupole moment is given by:

$$V_D(\mathbf{x}) = \frac{1}{8\pi\epsilon_0} \sum_{i,j} Q_{ij} \frac{x_i x_j}{r^5} \tag{4.12}$$

In an area with an inhomogeneous electric field, that is where $\nabla\mathbf{E}$, given by[4]:

$$\nabla E_{ij} = \frac{\partial^2 V}{\partial x_i \partial x_j} \tag{4.13}$$

is nonzero, the classical interaction energy due to the dipole moment is given by:

$$E_Q = \frac{1}{6} \sum_{i,j} \nabla E_{ij} Q_{ij} \tag{4.14}$$

This interaction term can give rise to a torque on the nucleus, which behaves as if it were a fictitious magnetic field acting on the nuclear spin. It has been shown that in situations engineered to maximize $\nabla\mathbf{E}$, this quadrupolar interaction can be sufficient to overwhelm the nuclear dipole-dipole coupling and extend the longitudinal relaxation time T_1 [77]. Additionally, the quadrupolar moment can lead to $\Delta m = \pm 2$ transitions in systems which lack cubic symmetry, which are otherwise forbidden[63]. The quadrupolar moment

[4]Note that this is not the divergence, $\nabla \cdot \mathbf{E}$, but rather the rank 2 tensor defined by the outer product of the gradient operator ∇ with $\mathbf{E}$.

can couple to lattice phonons, which generate oscillating local field gradients, and lead to relaxation of the nuclear polarization. This effect is expected to dominate relaxation due to coupling to the electrons at temperatures above 30 K in GaAs [74], and should result in T_1 times which scale as T^{-2}. Further details of the role of the nuclear quadrupolar moment can be found in Chapter 6 of Ref. [26].

4.3 Hyperfine electron-nuclear spin coupling

Hyperfine coupling, which results from interactions between the electron and nuclear spin magnetic moments, plays a crucial role in the combined electron-nuclear spin system. The Hamiltonian for this interaction is given by:

$$\mathscr{H} = \gamma_e \gamma_n \hbar^2 \left[\frac{8\pi}{3} \delta(\mathbf{r}_I)(\mathbf{I} \cdot \mathbf{S}) + \frac{3(\mathbf{I} \cdot \mathbf{r})(\mathbf{S} \cdot \mathbf{r})}{r^5} - \frac{\mathbf{I} \cdot \mathbf{S}}{r^3} \right] \tag{4.15}$$

where $\gamma_{e(n)}$ is the electron (nuclear) gyromagnetic ratio, $\mathbf{S}$ is the electron spin vector operator, and, when integrated, the term $\delta(\mathbf{r}_I)$ is an instruction to evaluate the electron wave function at the position of the nucleus. The first term within the brackets corresponds to the so-called "contact" hyperfine interaction due to the dependence on the overlap of the electron wave function at the location of the nucleus. This dependence means that this interaction is strongest for electrons in s-like orbitals, or where the orbital angular momentum l is zero. This means that the conduction band electrons bound to shallow impurities (which have s-like orbitals) lead to strong hyperfine interactions. The remaining terms result from the dipolar interaction between electrons and the nucleus. We will focus on the contact hyperfine interaction, as the dipolar hyperfine interaction is considerably weaker [26]. It should be mentioned, however, that the dipolar portion of the hyperfine coupling does not conserve angular momentum, and can lead to depolarization of the nuclei.

The term $\mathbf{I} \cdot \mathbf{S}$ in the above Hamiltonian can be expanded as:

$$\mathbf{I} \cdot \mathbf{S} = I_x S_x + I_y S_y + I_z S_z \tag{4.16}$$

$$= I_z S_z + \frac{1}{2}(I_+ S_- + I_- S_+) \tag{4.17}$$

where $S_\pm$ and $I_\pm$ are the electron and nuclear spin raising and lowering operators, given by $S_\pm = S_x \pm i S_y$ and $I_\pm = I_x \pm i I_y$.

4.3.1 Static effects

The first term in Eq. 4.17 gives rise to the so-called static effects of the hyperfine mechanism. Namely, the nuclear spin gives rise to an effective magnetic field experienced by the electron, and vice versa. In the case of the magnetic field felt by the i^{th} nucleus due to the polarization of the electrons, we find:

$$\mathbf{B}_e^i = -\frac{2\mu_0}{3} g_0 \mu_B \sum_q \vec{S}_q |\psi_q(\vec{r}_i)|^2 \tag{4.18}$$

Here, the sum is performed over the occupied electron states. This field is known as the Knight field and results in the Knight shift in the nuclear magnetic resonance frequency.

Conversely, a net nuclear polarization leads to a magnetic field felt by the electrons. It is this magnetic field, which contributes to the precession of electrons polarized perpendicular to the field, that will be used to measure a nuclear spin polarization in upcoming sections. Since the electrons simultaneously interact with a large number of nuclei, an effective magnetic field can be found which is proportional to the average nuclear polarization. This magnetic field is known as the Overhauser field and is given by:

$$\mathbf{B}_n^q = \frac{2\mu_0}{3} \frac{g_0}{g^*} \hbar \sum_{i,\alpha} \gamma_i^\alpha \mathbf{I}_i^\alpha |\psi_q(r_i^\alpha)|^2 \tag{4.19}$$

where the sum is performed over the the i nuclei of species α. If the polarization of the

nuclei of each species is uniform with average value $\langle I_\alpha \rangle$, this field can be written as:

$$\mathbf{B}_\alpha = b_N^\alpha \langle \mathbf{I}_\alpha \rangle \tag{4.20}$$

where b_N^α is the field due to species α that would exist if the nuclei were completely polarized, given by.

$$b_N^\alpha = \frac{2\mu_0}{3}\frac{g_0}{g^*}\hbar \sum_i \gamma_\alpha |\psi_q(r_i^\alpha)|^2 \tag{4.21}$$

The values of b_N^α for GaAs were calculated in Ref. [62], and are summarized in Table 4.2. Despite the small moment of the nuclei, the large density of the nuclei leads to large fields at full polarization.

Nuclear Species	b_N^α
^{69}Ga	-910 mT
^{71}Ga	-780 mT
^{75}As	-1840 mT

Table 4.2: Magnetic field experienced by electrons in GaAs due to complete polarization of the most common species present in samples used in this study.

4.3.2 Dynamic nuclear polarization

The second part of Eq. 4.17, $\frac{1}{2}(I_+S_- + I_-S_+)$, gives rise to the dynamical effects of the hyperfine coupling. In particular, this term leads to mutual spin flips between the electron and nuclear spin systems which conserve angular momentum. It is this term that leads to so-called dynamic nuclear polarization (DNP).

DNP occurs when the electron spin system is out of thermodynamic equilibrium. That is, when the Fermi energies of the two conduction band spin sub-bands are unequal. When this is the case, electrons in the spin state with the higher Fermi energy can minimize their energy by undergoing a mutual spin flip with a nucleus in the lattice, thereby transitioning to the lower energy spin sub-band, and then relaxing via scattering to available states near the

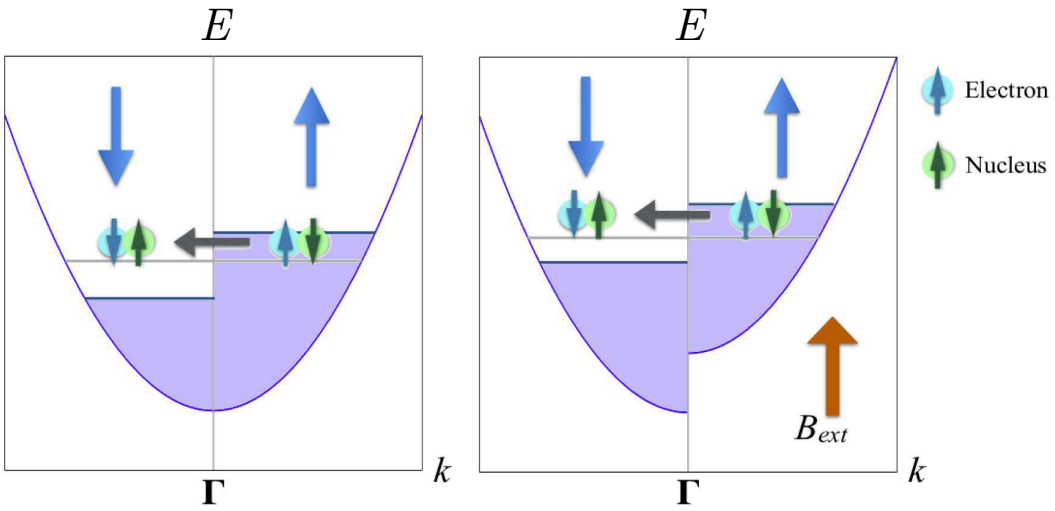

Figure 4.1: Diagrams showing the process of DNP resulting from polarizing electrons which would otherwise be unpolarized (left) and the depolarization of electrons which would be polarized at equilibrium due to Zeeman splitting in an external field (right).

Fermi energy. Because the energy gained by the nucleus is much smaller than that lost by the electron due to the much smaller dipole moment, this spin flip is energetically favorable overall. The reverse process is suppressed because of the unavailability of open states in the spin sub-band with a higher Fermi energy.

The process of dynamic nuclear polarization is represented diagrammatically in Fig. 4.1, which shows two situations which lead to DNP. In this diagram, filled states in the conduction band are indicated by blue shading. In the first situation, shown in panel a), the electron spin system is directly pumped, generating a spin polarization that is out of thermodynamic equilibrium. This is the type of DNP we seek to generate here, where the electron spin pumping is achieved via CISP.

Rather less intuitively, DNP can also be driven by *depolarizing* electrons which would otherwise be polarized at equilibrium due to Zeeman splitting in the presence of an external magnetic field. This is the type of DNP first demonstrated by Overhauser, where electrons in a large external field were continuously depolarized via saturation of the electron spin resonance [55]. This process is shown diagrammatically in Fig. 4.1 b). In this case, the maximum degree of nuclear polarization depends on the equilibrium electron spin polarization,

and the degree to which the electrons are effectively depolarized from this value.

4.3.3 Equilibrium nuclear spin polarization

Here, we seek an expression for the average nuclear polarization at equilibrium, which is related to the nuclear magnetic field at saturation through Eqn. 4.20. The analysis here is adapted primarily from Chapter 2 in Ref. [15] and Chapters 8 and 9 in Ref. [26]. Other sources arrive at similar expressions using arguments based on equilibration of electron and nuclear spin temperatures in the high temperature limit [26, 27, 62, 78, 79].

At equilibrium, the total number of nuclei transitioning between the two adjacent spin states $|m\rangle|\uparrow\rangle$ and $|m+1\rangle|\downarrow\rangle$ [5] in each direction will be equal. That is:

$$W_{(m,\uparrow)\rightarrow(m+1,\downarrow)} n_m^N n_\uparrow^e = W_{(m+1,\downarrow)\rightarrow(m,\uparrow)} n_{m+1}^N n_\downarrow^e \tag{4.22}$$

where the W's are transition probabilities linking the two states, $n_\uparrow^e(n_\downarrow^e)$ is the fraction of electrons in state $|\uparrow\rangle(|\downarrow\rangle)$, and $n_m^N(n_{m+1}^N)$ is the fraction of nuclei in state $|m\rangle(|m+1\rangle)$. The transition probabilities are thermodynamically related by:

$$W_{(m,\uparrow)\rightarrow(m+1,\downarrow)} = \exp\left(\frac{g\mu_B B}{\hbar}\frac{1}{k_B T}\right) W_{(m+1,\downarrow)\rightarrow(m,\uparrow)} \tag{4.23}$$

where the first factor within the exponential is the energy difference between the two states due to the Zeeman splitting of the electrons in an external field B[6] and the second term is the inverse of the thermal energy, where T is taken to be the lattice temperature. Combining Eqns. 4.22 and 4.23, we arrive at:

$$\frac{n_{m+1}^N}{n_m^N} = \exp\left(\frac{g\mu_B B}{\hbar k_B T}\right)\frac{n_\uparrow^e}{n_\downarrow^e} \tag{4.24}$$

[5] Here, the kets $|m\rangle$ and $|m+1\rangle$ refer to the nuclear spin state and the kets $|\uparrow\rangle$ and $|\downarrow\rangle$ refer to the state of an electron in the conduction band which undergoes a mutual spin flip via the dynamic part of the contact hyperfine Hamiltonian with the nucleus in question

[6] The Zeeman energy of the nuclei is neglected because of its small dipole moment as compared to the electron

Since the electron spin system can be described using Maxwell-Boltzmann statistics, the exponential term can be rewritten in terms of the equilibrium electron spin polarization as:

$$\frac{n_{\downarrow}^{e,T}}{n_{\uparrow}^{e,T}} = \exp\left(\frac{g\mu_B B}{\hbar k_B T}\right) \tag{4.25}$$

where the superscript T indicates that this is the average spin at thermal equilibrium. We now make use of the expressions:

$$S = \frac{1}{2}(n_{\uparrow} - n_{\downarrow}) \tag{4.26}$$

$$n_{\uparrow} + n_{\downarrow} = 1 \tag{4.27}$$

Equation 4.25 can then be rewritten as:

$$\frac{n_{\downarrow}^{e,T}}{n_{\uparrow}^{e,T}} = \frac{(1 - 2S_T)}{(1 + 2S_T)} \tag{4.28}$$

with:

$$S_T = -\frac{1}{2}\tanh\left(\frac{g\mu_B B}{2\hbar k_B T}\right) \tag{4.29}$$

Finally, equations 4.24 and 4.25 can then be rewritten as:

$$\frac{n_{m+1}^{N}}{n_{m}^{N}} = \frac{(1 + 2S)}{(1 - 2S)}\frac{(1 - 2S_T)}{(1 + 2S_T)} \tag{4.30}$$

With this equation, the average nuclear polarization I_{av} in the sample can be expressed in terms of the Brillouin functions [7], so that the average nuclear polarization is given by:

$$I_{av} = IB_I\left[I\ln\left(\frac{(1 + 2S)(1 - 2S_T)}{(1 - 2S)(1 + 2S_T)}\right)\right] \tag{4.31}$$

Here, $B_I(x)$ is the Brillouin function defined by:

$$B_I(x) = \frac{2I+1}{2I}\coth\left(\frac{2I+1}{2I}x\right) - \frac{1}{2I}\coth\left(\frac{1}{2I}x\right) \tag{4.32}$$

As expected, when the electron spins are in equilibrium ($S = S_T$), the average nuclear polarization goes to zero. The fact that it does not go to its own thermodynamic equilibrium value is a result of the fact that in the derivation of these equations we neglected the Zeeman energy of the nuclear spin in Eqn. 4.23. If the electron spin polarization is small, and the equilibrium thermal electron spin polarization S_T is neglected, the Brillouin function can be expanded, so that $\mathbf{I}_{av}$ can be approximated to first order in vector form as:

$$\mathbf{I}_{av} = \frac{4}{3}I(I+1)\frac{(\mathbf{S}\cdot\mathbf{B})\mathbf{B}}{B^2} \tag{4.33}$$

In this approximation, $\mathbf{I}_{av}$ will be proportional to the projection of the electron spin polarization onto the direction of the external magnetic field, and will lie along the external magnetic field, but will not depend on its magnitude.

All of the above analysis assumes that the nuclei relax only through their coupling to the electron spins through the hyperfine interaction. In reality, nuclei are weakly coupled to the environment through interactions with paramagnetic impurities, electron orbital angular moment, the dipolar component of the hyperfine interaction, and in the case of nuclei with a non-zero quadrupole moment, to phonons. These couplings are weaker than the coupling to the electron spins at low temperature. Measurements of spin-lattice relaxation times for ^{69}Ga and ^{75}As in GaAs with an 8 T external magnetic field with similar doping levels to those used here show that at temperatures below 30 K nuclear relaxation is dominated by coupling to the electrons, while at higher temperatures the effects of two-phonon quadrupolar relaxation becomes important [74]. The effect of other relaxation mechanisms on the equilibrium nuclear

spin polarization can be included by the introduction of a "leakage factor" f, given by:

$$f = \frac{T_1}{T_1 + T_{1e}} \tag{4.34}$$

where T_1 is the inverse of the nuclear polarization population decay rate due to all channels except through hyperfine coupling to the electrons.

4.3.4 Polarization timescale

The timescale over which nuclear polarization resulting from DNP builds is, of course, the same as the decay rate of the nuclear spin polarization due to hyperfine coupling to the electrons. This rate can be approximated from the following equation [80]:

$$\frac{1}{T_{1e}} = \frac{\tilde{\omega}^2 \tau_e}{1 + \Omega^2 \tau_e^2} \tag{4.35}$$

where $\tilde{\omega}$ is the Larmor precession frequency of the nuclei in the fluctuating effective field resulting from the electrons, τ_e is the correlation time of those fluctuations, and Ω is the nuclear Larmor frequency in the external magnetic field. When the external field is strong compared to the fluctuating field, the decay time T_{1e} is extended.

In our samples, there are two types of electrons present which lead to DNP; itinerant electrons in the conduction band, and electrons which are bound to shallow donor states. In GaAs, the donor binding energy of Si donors which substitute for Ga lattice sites is 5.84 meV [9]. The binding energy divided by the Boltzmann constant gives a temperature scale of 68 K. Accordingly, the donor occupation will vary over the 10-50 K temperature range used here, with higher occupation at lower temperatures. At all times, both types of electrons can be considered to be characterized by the same spin polarization, as they equilibrate at a rate that is much faster than they lose polarization due to the coupling to the nuclear spin system. The effects of these two types of electrons on T_{1e} will be discussed separately.

We start with itinerant electrons. These electrons move around the lattice with a velocity

near the Fermi momentum, given by $v_F = \hbar k_F / m^*$ where m^* is the electron effective mass. The correlation time is then assumed to be roughly the time an electron with this momentum is localized in a particular nuclear volume. This time will scale as the inverse of the electron velocity, and by extension $T^{-1/2}$ where T is the lattice temperature. An accurate calculation of this decay time is found in Ref. [81]. There, it is confirmed that the relaxation rate should scale as $1/\sqrt{T}$. Numerical estimates from these calculations are performed in [15], and suggest that T_{1e} should be on the order of 300 s at 10 K in our samples.

Electrons trapped on shallow donors behave in much the same way as a paramagnetic impurity within the lattice [15, 57, 81, 82]. Because the electron is localized, the correlation time for fluctuations in the magnetic field seen by the nucleus is longer, and set either by the electron polarization lifetime or, if it occurs more quickly, the length of time electrons are bound to a particular donor before they become ionized or hop to other donors. This long correlation time means that the relaxation due to bound electrons is much faster for nuclei within a Bohr radius of the donor. Quantitative calculations of this lifetime give:

$$\frac{1}{T_{1e}(r)} = \frac{A^2 v_0^2 n \tau_e}{2\pi^2 N_D a_B^6 \hbar^2} \exp\left(-\frac{4r}{a_B}\right) \tag{4.36}$$

where A is a measure of the strength of the hyperfine interaction, N_D is the donor occupation, and a_B is the Bohr radius. Estimates suggest that for electrons within a Bohr radius, T_{1e} should be on the order of 0.1 s in our sample [15]. However, T_{1e} increases rapidly as the distance from the donor increases.

The samples used in this study have a doping density of 3×10^{16} cm^{-3} so that if the volume per dopant is assumed to be spherical, it would have a radius of 20 nm. The volumetric average distance from the center of a spherical region is $\langle r \rangle = 3r/4$, so that the average distance to the nearest donor is roughly 15 nm, which is more than 280 times the Bohr radius. For the vast majority of electrons, then, the relaxation due directly to bound electrons is negligible due to the exponential term in Eqn. 4.36. However, nuclear

polarization which occurs within a donor's region of influence will spread via nuclear spin diffusion. The time it takes a polarization to diffuse a distance r can be approximated as $T_D \approx r^2/D$, where D is the diffusion constant. In GaAs, D has been measured to be on the order of 10^{-13} cm^{2}s^{-1} [83]. Accordingly, the polarization time for nuclei with the average distance from a donor is found to be on the order of 30 s. This diffusion constant is not expected to vary strongly with lattice temperature, so that the temperature dependence of T_{1e} from bound electrons will be determined primarily by the change in occupation of the donors.

The above calculations for the various relaxation times T_{1e} should be considered to be, at best, estimates of the order of magnitude of relaxation time resulting from each mechanism. In both cases, parameters which go into the calculations are only known to within an order of magnitude. Generally, determining T_{1e} is a matter to be settled by experiment. As discussed below, we find values of T_{1e} of about 3 minutes at 10 K, and that T_{1e} scales as $T^{-0.8}$. These results are broadly consistent with the mechanisms presented here, though the precise details of the contribution of the various mechanisms is, at this point, undetermined.

4.4 Experiment

In this section, I will discuss a series of experiments carried out in which we have attempted to elucidate the process of dynamic nuclear polarization in InGaAs which occurs due to pumping of the electron spin system via current-induced spin polarization, discussed in section 2.7, and to arrive at some quantitative measurements of the achievable nuclear polarization and the timescale at which these polarizations are built up. Nuclear polarization is detected by way of the static effects of the hyperfine coupling to conduction band electrons. The magnetic field seen by electrons due to the polarization of the nuclei is detected by its effect on the electron Larmor precession frequency. The precession frequency is measured via time-resolved Faraday rotation, which is discussed in III.

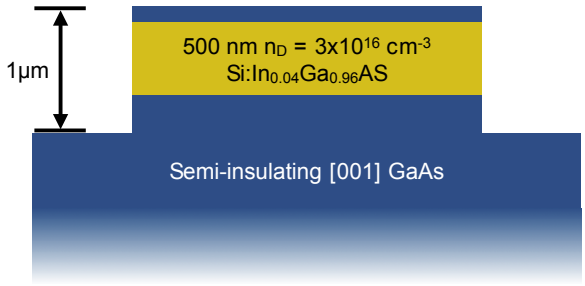

Figure 4.2: Cross-section of samples used in all measurements. Mesa etches are performed to a depth of 1 μm to ensure doped regions are fully removed in regions other than the defined channels.

4.4.1 Materials and sample design

All samples used in this study consist of a 500 nm thick layer of Si-doped $n = 3 \times 10^{16}$ cm^{-3} $In_{.04}Ga_{.96}As$ grown by molecular beam epitaxy atop semi-insulating [001] GaAs substrate, and capped with 100 nm of GaAs. The sample cross-section is shown in Fig. 4.2. The samples are then patterned into one of two device designs using standard photo-lithographic fabrication techniques and an isotropic wet etch process. Ohmic contacts, consisting of alternating layers of nickel, germanium, and gold, are deposited and annealed at 420 C in forming gas for 60 seconds to drive in-plane current. The first sample design, which will be referred to as the cross channel design, has four contacts around a square mesa-etched region designed so that a current can be driven in any in-plane direction [8, 17, 84], as shown in Fig. 4.3. Numerical calculations find a region of electric field uniformity with a radius of 35 μm in which the amplitude deviates by less than 5% and its direction by less than 5° [8]. The pump and probe beam radii were measured to be approximately 15 μm. Errors placing the beam at the center of the sample could introduce errors in the electric field amplitude and direction. The second sample design used, known henceforth as the L channel design,

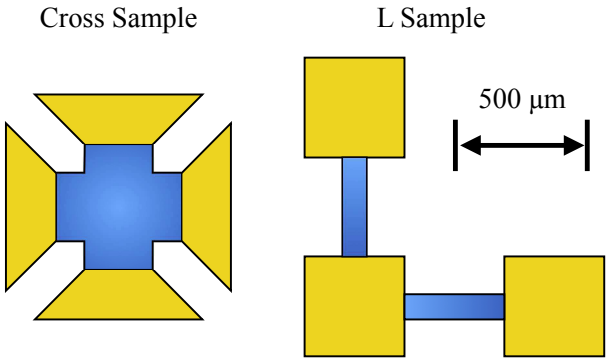

Figure 4.3: Device designs used in these measurements. The cross sample allows for an arbitrary current direction at the center of the sample, while the L sample suppresses errors due to inhomogeneous electric field and allows for higher current densities at a particular ohmic power dissipation.

consists of 400 μm long by 100 μm wide channels etched along the [110] and [1$\bar{1}$0] crystal directions, as shown in Fig. 4.3. This sample design allows for a higher electric field than the cross channel design for a given power dissipation. Additionally, errors in electric field direction and magnitude due to beam placement are eliminated. However, measurements for different crystal directions are performed on different channels, and previous measurements have shown that the spin-orbit field and CISP magnitudes vary strongly with position, perhaps as a result of inhomogeneous uniaxial strain [8, 85]. Accordingly, though we expect stronger CISP with current along [1$\bar{1}$0], comparisons between the DNP observed on the two channels are hindered by the effects of the local strain field.

In all samples and device designs, we will focus on current which flows along the [110] and [1$\bar{1}$0] directions only. Doing so allows us to make two simplifying assumptions. First, for current in these directions, both the Rashba and Dresselhaus spin-orbit fields, and the associated generation of CISP, are perpendicular to the direction of electron current. Second, since the electron decay tensor $\overleftrightarrow{\Gamma}$ is expected to be diagonalized in the [110] [1$\bar{1}$0] [001] basis,

the steady state electron spin polarization due to CISP will also remain perpendicular to the direction of electron current. We therefore expect no contribution to DNP from CISP when the sample is oriented so that current flows parallel to the external magnetic field.

4.4.2 Experimental procedure

The sample is placed in a helium flow cryostat which is held between the poles of an electromagnet. A magnetic field is applied in the sample plane along the $\hat{x}$ direction as defined in Fig. 4.4, both to suppress nuclear spin relaxation by magnetic dipole-dipole interactions [26] and to facilitate optical Larmor magnetometry [63, 65, 86]. In Larmor magnetometry, test electron spins are optically injected along $\pm\hat{z}$ using a circularly polarized pump pulse and their precession about the total magnetic field, which occurs at the Larmor precession frequency $\Omega_L = g\mu_B B_{tot}/\hbar$, is monitored by time resolved Faraday rotation. If the electron g factor is known, a measurement of the precession frequency can be used to determine the associated magnetic field. The circularly polarized pump beam is modulated between left and right circular polarization at 50 kHz by a photo-elastic modulator for lock-in detection. Additionally, this modulation ensures that the optical injection of polarized carriers does not directly lead to nuclear polarization. The external magnetic field causes the test electron spins to precess at a high enough frequency that many rotations can be measured over the time delays accessible to the mechanical delay line. This allows for measurement of the total magnetic field about which the electrons precess to be measured to a precision of approximately 100 μT in the 40 seconds it takes to complete a scan of the pump-probe delay time over the range $\Delta t = 3000 \rightarrow 5000$ or $\Delta t = 5000 \rightarrow 7000$ ps with 50 ps steps.

Figures 4.5 and 4.7 show a measurement performed on device A (sample 050331B2-J, cross channel design) with current along $[1\bar{1}0]$ and at a temperature of 10 K. Figure 4.5 contains a plot of the Faraday rotation signal observed due to the test electron spin packet as a function of pump-probe time delay (horizontal axis) and lab time (vertical axis). At lab time 0, a voltage is applied across the sample. A rapid shift in the precession frequency,

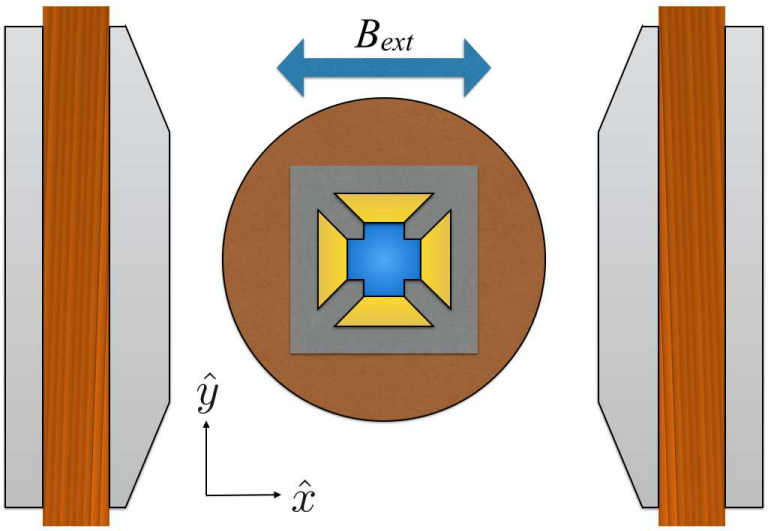

Figure 4.4: Schematic of measurement geometry and definition of the local coordinate system referred to throughout this chapter.

corresponding to a change in field of a few millitesla, occurs due to the spin-orbit field [84]. A slow shift in the precession rate follows, which we attribute to nuclear polarization. After 10 minutes, the voltage is switched off and the nuclear spin polarization decays.

Each time delay scan is fit to extract the electron Larmor precession frequency and the total field about which the electrons precessed is calculated. Experimental data and the corresponding fit for one such delay scan is plotted in Fig. 4.6 This data corresponds to the first delay scan shown in Fig. 4.5. The data is fit to the following equation:

$$V_{LI2} = A\cos\left(\frac{g\mu_B B}{\hbar}\Delta t\right)\exp\left[-\frac{\Delta t}{T_2^*}\right] + c \tag{4.37}$$

where the free parameters are the amplitude A, magnetic field B, electron spin lifetime T_2^*, and a constant offset c. Here, we find A = 0.2036 V, B = 200.3 mT, T_2^* = 6473 ps, and c = -4 mV.

The results of fits to the magnetic field for all delay scans shown in Fig. 4.5 are plotted in Fig. 4.7, along with a fit to the equation $B(t_L) = \Delta B_N(1 - \exp[-t_L/T_{1e}]) + B_0$ where t_L is lab time and B_0 is the sum of the external and spin-orbit fields. The saturation change in

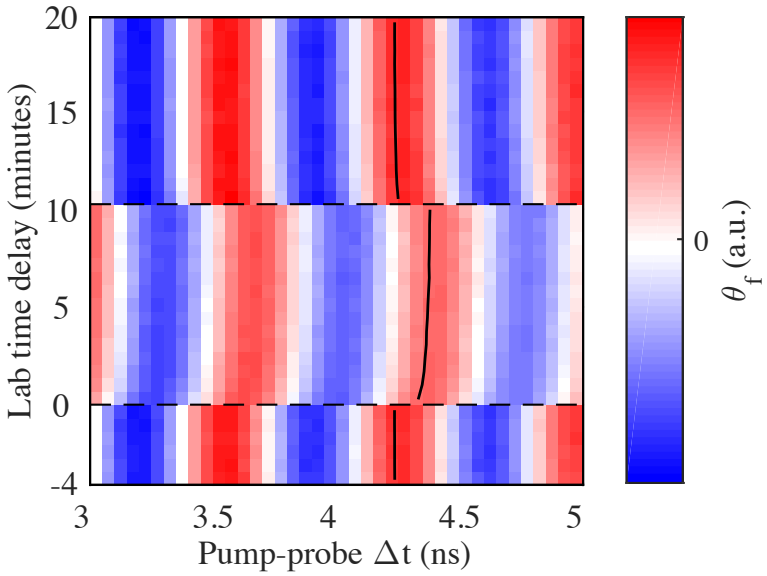

Figure 4.5: Series of Faraday rotation time delay scans showing a transition from $V_{DC} = 0$ V to 2 V at lab time 0 and back to 0 V after 10 minutes . Data were taken on sample A with current flowing along $[1\bar{1}0]$ at 10 K with 200 mT external field applied. Solid black line indicates position of local maximum from fits to Faraday rotation signal.

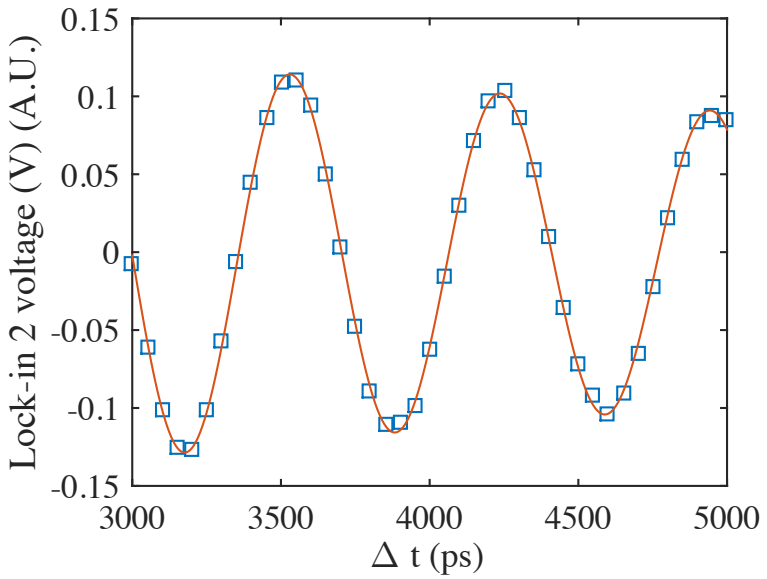

Figure 4.6: Raw TRFR Data (blue squares) and a fit to the data (red line) using Eqn. 4.37

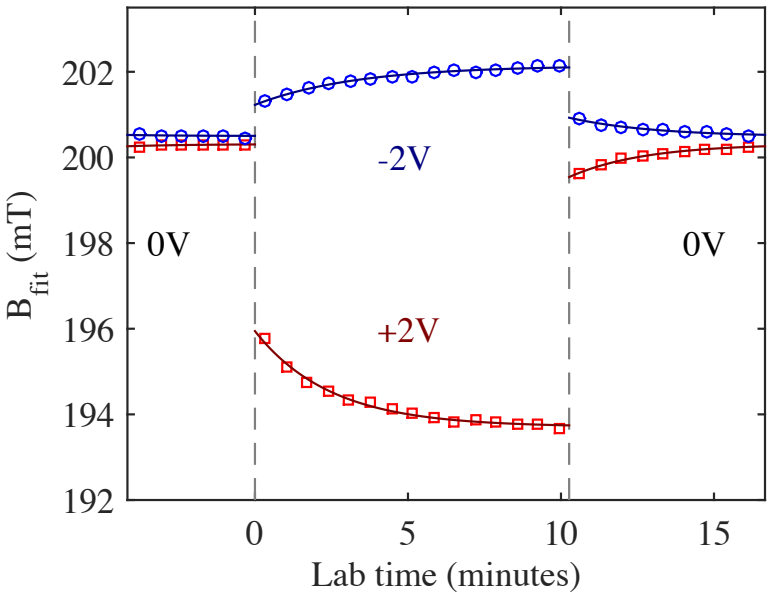

Figure 4.7: Total magnetic field as measured from fits to delay scans shown in 4.5 (red squares) along with another similar transition to $V_{DC} = -2$ V (blue circles). Lines show exponential fits to magnetic field data. Fits allow extraction of saturation nuclear field B_N and saturation time T_{1e}.

nuclear field ΔB_N and the polarization time T_{1e} are extracted from the fit. The transition from $V_{DC} = 0 \rightarrow 2$ V shows $\Delta B_N = -2.2$ mT and $T_{1e} = 148$ s, while the transition from $V_{DC} = 0 \rightarrow -2$ V shows $\Delta B_N = 1.0$ mT and $T_{1e} = 198$ s.

By comparing the absolute Faraday rotation angle under optical versus current-induced spin polarization, measurements published in Ref. [47] have shown that the degree of polarization at the temperature and electric field used here is expected to be on the order of 10^{-4} to 10^{-3}. Using this degree of polarization in conjunction with Eqn. 4.33 suggests that the change in nuclear polarization due to CISP in these measurements should be on the order of 2-20 mT. This is in good qualitative agreement with the experimental data, and suggests that our assumption that the leakage factor should be small at 10 K is a reasonable one. Deviation from this value may be caused by other mechanisms which affect the electron spin polarization, which are discussed in the following section.

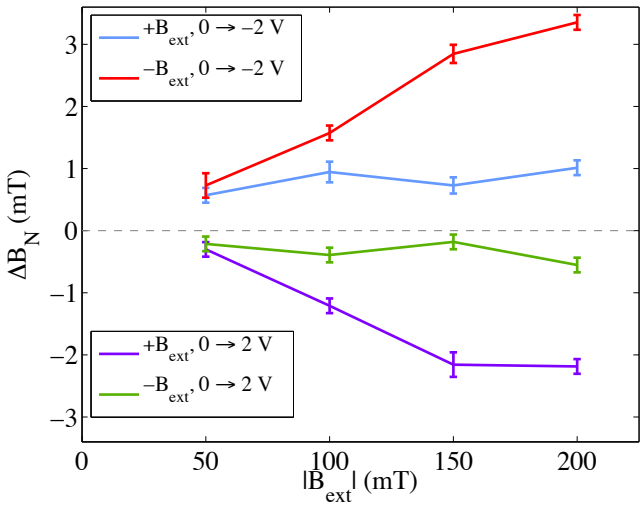

Figure 4.8: Saturation nuclear field versus applied magnetic field for four different types of voltage transitions (described in figure legend), showing asymmetry of unipolar transition saturation amplitudes. Measurements were taken on sample A with current along $[1\bar{1}0]$ at 10 K. Red and purple data sets show strong dependence on external field and correspond to a geometry in which the nuclear alignment and external magnetic field are antiparallel. Blue and green data sets correspond to nuclear alignment parallel to external field.

4.4.3 Voltage reversal asymmetry

There is a readily apparent asymmetry shown in Fig. 4.7; the transition to +2 V shows a larger shift in nuclear field than the transition to -2 V. Though it is not expected to be the case, we first confirm that this asymmetry is not due to material properties, sample fabrication anomalies, or previously unrecognized details of CISP by ensuring that the asymmetry is reversed when the external magnetic field direction is flipped. Confirmation of this is shown in Fig. 4.8. With B_{ext} along $+\hat{x}$, the a larger ΔB_N is seen in transitions from $V_{DC} = 0 \rightarrow 2$ V (purple trace) than $0 \rightarrow -2$ V (blue trace). When the magnetic field is flipped to $-\hat{x}$, ΔB_N is larger for transitions of $V_{DC} = 0 \rightarrow -2$ V (red trace) than $0 \rightarrow +2$(green trace). This asymmetry remains consistent with a reversal of the external magnetic field direction. In each case, the transition in which the nuclear field is changing so that it opposes the external magnetic field results in a larger ΔB_N. Reported error bars represent the standard error of a set of 6 measurements at each point.

The origin of this asymmetry is investigated in Fig. 4.9, in which transitions in two

different geometries are shown. Measurements are again taken on sample A at 10 K with a 200 mT external magnetic field and current along $[1\bar{1}0]$. Here, light red and light blue shading indicates that the applied voltage $V_{DC} = 2$ or -2 V, respectively, and the inset text shows the measured values of ΔB_N for each labeled transition. Plot a) shows a set of transitions in which current was flowing along $\pm\hat{y}$, resulting in CISP oriented parallel to the external magnetic field B_{ext}. Here, we expect dynamic nuclear polarization to occur, resulting in a polarization given by Eqn. 4.33. In plot b), we rotate the sample by 90° so that the current is aligned along $\pm\hat{x}$, generating a CISP which is perpendicular to B_{ext}. With CISP perpendicular to B_{ext}, the $(\vec{B} \cdot \vec{S})$ term in Eqn. 4.33 suggests that there should be no observable DNP, however a non-zero ΔB_N is measured. Here, the direction of the current does not significantly alter the observed ΔB_N, as seen in Fig. 4.9. This rules out the possibility that there could be an inadvertent polarization due to a component of CISP that is not perpendicular to the electron drift velocity, as that would be expected to reverse sign with the voltage. However, CISP could still contribute. Electrons that are aligned by CISP will be out of thermodynamic equilibrium, and could cause isotropic DNP accordingly. This would not, however, be sufficient to explain the asymmetry observed with CISP parallel to B_{ext}. Instead, there must be another source of DNP which is isotropic with respect to electron drift velocity.

The observed ΔB_N with CISP perpendicular to B_{ext} can be explained as resulting from one of two possible effects: the hot electron effect, [87] and/or an effect linked to the presence of the pump and probe beams [63]. The hot electron effect results in a heating of the electron spin system which varies with the magnitude of current in the sample but not its direction. This heating of the spin system results in electrons which are depolarized compared to their thermal equilibrium, driving DNP.

Additionally, the pump and probe beams, which are tuned just below the absorption edge, result in photo-excited carriers which are nominally unpolarized in the axis of quantization defined by the external magnetic field in the Voigt geometry. These optically injected spins

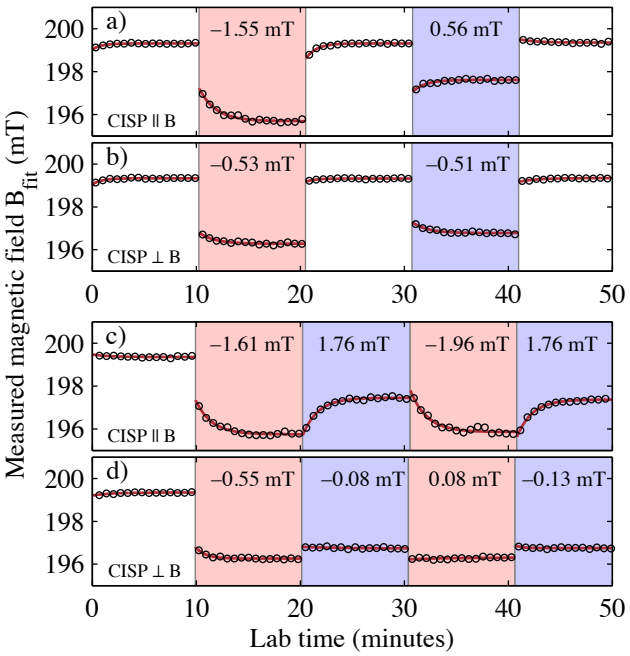

Figure 4.9: Total magnetic field measured via Larmor magnetometry following voltage transitions with CISP parallel (parts a) and c)) or perpendicular (parts b) and d)) to the external magnetic field. All data taken at 10 K with $B_{ext} = 200$ mT. Light red and light blue shading indicate $V_{DC} = 2$ V and -2 V, respectively. Inset text indicates field geometry and total change in nuclear field ΔB_N in the labelled transition. Plots a) and b) show transitions of the form $V_{DC} = 0 \rightarrow \pm 2$ V; the observed asymmetry with CISP parallel to B_{ext} in a) results from current direction-independent DNP mechanisms, which are seen in b) when CISP is perpendicular to B_{ext}. By considering transitions of the form $V_{DC} = \pm 2 \rightarrow \mp 2$ V (plots c) and d)), contributions to ΔB_N from current direction-independent mechanisms are suppressed, isolating DNP due to CISP and highlighting the strong directional dependence of ΔB_N due to CISP on current direction.

result in heating of the electron spin system where they are present. In Ref. [63], changes in nuclear field due to this optical effect were observed by monitoring changes in electron spin precession after the pump and probe beams were displaced on the sample, therefore generating a nuclear polarization where there previously was none. The presence of this effect was verified at much lower external magnetic field strengths in our experiment by monitoring electron precession frequency following a displacement of the sample of approximately 100 μm at 10 K. At saturation, the shift in nuclear polarization was found to be on the order of 10 mT with a combined pump-probe power of approximately 150 μW and with the laser tuned to an energy just above the absorption edge. There is typically no displacement of the beam in measurements of DNP resulting from CISP. However, when a voltage is applied, photo-excited carriers will be driven out of the region of interrogation due to electron drift, giving rise to a voltage-dependent change in nuclear spin polarization which depends on the voltage magnitude and absorbed pump and probe power.

The asymmetry between transitions to +2 V versus -2 V seen in Fig. 4.9 (a) can then be explained as the result of an interplay between DNP due to CISP and DNP due to isotropic mechanisms outlined above. If contributions to DNP due to the various sources discussed here are assumed to behave linearly[7], we may subtract the values of ΔB_N observed in transitions with CISP perpendicular to B_{ext} (panel a) from those with CISP parallel to B_{ext} (panel b), the contribution to ΔB_N from CISP is isolated, and the asymmetry disappears.

We now consider transitions of the type $V_{DC} = \pm\text{V} \rightarrow \mp\text{V}$ after saturation at V. In these measurements, contributions to changes in nuclear field caused by mechanisms that do not depend on the direction of current are suppressed. This allows current direction-dependent alignment mechanisms to be studied in isolation. Figure 4.9 parts c) and d) show measurements where these transitions are performed with CISP parallel and perpendicular to B_{ext}, respectively, at lab times of about 20, 30, and 40 minutes. These measurements highlight the strong dependence of ΔB_N on the orientation of the current in the sample;

[7]This is a reasonable assumption so long as the nuclear polarization remains small and far from saturation

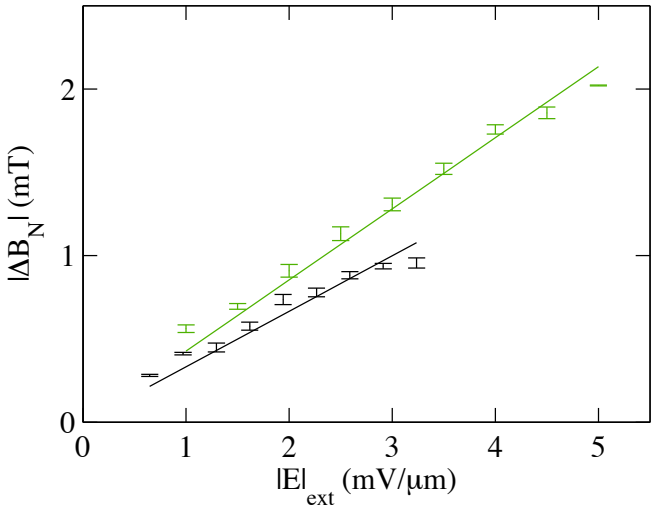

Figure 4.10: ΔB_N for transitions of the form $V_{DC} = \pm 2 \rightarrow \mp 2$ V taken in Sample A with current along $[1\bar{1}0]$ (black) and sample B with current along [110] (green). Lines represent linear fits to the data

ΔB_N with CISP parallel to B_{ext} is an order of magnitude larger than ΔB_N with CISP perpendicular to B_{ext}.

4.4.4 DNP scaling with electric field

Figure 4.10 shows the saturated nuclear field strength at 30 K with $B_{ext} = 200$ mT for sample A with current along $[1\bar{1}0]$ (black) and sample B with current along [110] (green) as a function of the applied electric field. The design of Sample B allows for higher applied electric fields at a given thermal power dissipation. The linear scaling of the saturated nuclear field with applied electric field is consistent with previous measurements of the degree of electron spin polarization due to CISP in these samples [8, 33, 47]. This result was found to be consistent on all samples and with current in both orientations used in this study. These measurements were repeated on samples A, B, and C with current in both the [110] and $[1\bar{1}0]$ directions. The slope of the saturation change in nuclear field ΔB_N versus applied electric field was obtained from a fit to the data, and the resulting values are found in Table 4.3. In addition, the slopes were generally found to be consistent with independent measurements

Sample	Orientation[8]	$B_{N,sat}/E_{ext}$[9]	T_{1e} (s)	η[10]
A (cross)	[110]	9.2 ± 2.5	70 ± 8	–
A (cross)	$[1\bar{1}0]$	33.0 ± 2.5	61 ± 1	0.515
B (L)	[110]	42.7 ± 1.8	72 ± 1	0.548
B (L)	$[1\bar{1}0]$	40.7 ± 2.5	71 ± 2	0.616
C (cross)	[110]	6.8 ± 1.4	97 ± 7	–
C (cross)	$[1\bar{1}0]$	36.1 ± 4.7	85 ± 3	–

Table 4.3: Results from measurements at 30K for all samples and orientations used in this study. $B_{N,s}/E_{ext}$ is found by fitting data shown in Fig. 3 a) to a straight line with y intercept set at 0. CISP efficiencies η, as defined in Sec. 2.7, are reported where available.

of CISP efficiency η, as defined in Sec. 2.7. That is, samples and orientations which showed strong CISP also show strong DNP. Values of η where available are included in Table 4.3. The available data does not span the range of measured DNP efficiencies, but does indicate that samples with similar values of η exhibit similar DNP efficiencies, hinting at a possible trend. Further systematic data showing the relationship between CISP polarization efficiency and DNP is unavailable due to the degradation of samples on which nuclear polarization data has been collected. Despite efforts to ensure the samples remain clean throughout the process of mounting and removing samples from the cryostat cold finger using either solvent-based silver paint or vacuum grease, after a few (typically 3 to 5) cycles, the observed Faraday rotation signal to noise ratio increases dramatically and precludes further measurement. Degraded samples appear clean under visual inspection, and channel resistances remain unchanged. The exact mechanism of sample degradation is currently unknown. Future work should include measurements designed to verify the relationship between CISP efficiency and DNP efficiency.

[8]Crystal axis along which current flows. CISP will be perpendicular to this direction, but parallel to the external magnetic field in all cases

[9]Reported in units of $mT \cdot \mu m \cdot V^{-1}$, $(\times 10^{-2})$

[10]Reported in units of μrad/μm.

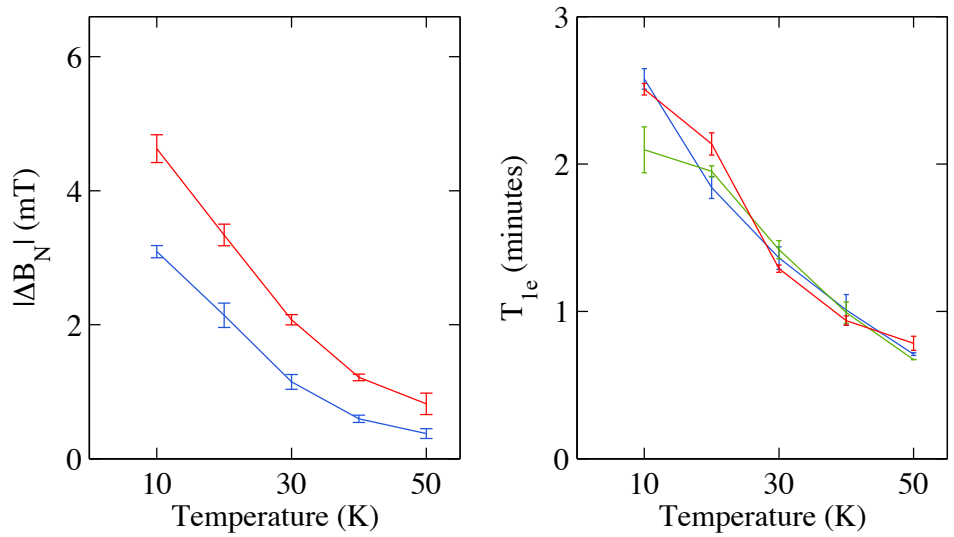

Figure 4.11: (Left) ΔB_N vs. sample temperature for transitions of $V_{DC} = \pm 1 \leftrightarrow \mp 1$ V (blue) and $V_{DC} = \pm 2 \leftrightarrow \mp 2$ V (red). (Right) T_{1e} (right) vs. sample temperature for transitions $V_{DC} = 0 \rightarrow +2$ V (blue), $V_{DC} = \pm 2 \leftrightarrow \mp 2$ V (red), and $V_{DC} = +2 \rightarrow 0$ V (green). The polarization times agree across all transition types.

4.4.5 Behavior of DNP with sample temperature

Measurements of ΔB_N and T_{1e} as a function of sample temperature are shown in Figure 4.11. Data here were taken on Sample A with an external magnetic field of 200 mT. The left plot shows the saturated change in magnetic field ΔB_N for transitions of $V_{DC} = \pm 1 \leftrightarrow \mp 1$ V (blue) and $V_{DC} = \pm 2 \leftrightarrow \mp 2$ V (red). Error bars indicated the standard error found in a set of 12 measurements at each temperature setting. At temperatures 30 K and above, doubling the change in voltage roughly doubles ΔB_N. At 10 K and 20 K, however, this is no longer the case. We attribute this to the onset of sample heating due to the current in the channel. For a given change in temperature ΔT, at lower temperatures the fractional change $\Delta T/T$ becomes larger, leading to a larger impact on ΔB_N. Also, at low temperatures, the thermal conductivity of the GaAs substrate decreases substantially, further exacerbating the effects of ohmic heating [88]. Measurements were attempted at 60 K; while the precession of the test electron spins was clearly observable, no nuclear polarization was found. This is broadly consistent with previous measurements [63].

The right-hand plot in Fig. 4.11 shows the behavior of T_{1e} as the sample temperature

is changed. In this figure, the blue line corresponds to transitions of $V_{DC} = 0 \rightarrow +2$ V, the red line to transitions of $V_{DC} = \pm 2 \leftrightarrow \mp 2$ V, and green to the depolarizing transitions of $V_{DC} = +2 \rightarrow 0$ V. The physical basis for this temperature-dependent behavior is complicated by the possibility of contributions from two mechanism by which electrons and nuclei undergo dynamic nuclear polarization. As discussed in Sec. 4.3.4, the Si donor binding energy of 5.84 meV is on the same order as the thermal energy $k_B T$, so that as the temperature is changed the donor occupation changes as well. Electrons which are bound to donors will efficiently polarize the nuclei within a small radius, and the nuclear polarization is then spread by diffusion, so that the timescale is set primarily by the diffusion constant. At higher temperatures, donor states become ionized, so that DNP occurs through coupling to itinerant electrons in the conduction band. Through this mechanism, T_{1e} is expected to be proportional to $T^{-\frac{1}{2}}$. Which mechanism dominates will depend on the occupation of the donor states. Fits to the data in Fig. 4.11 b) find that T_{1e} scales as $T^{-0.8}$ in these measurements. This may be complicated by the presence of ohmic heating within the samples, which has not been accounted for.

4.5 Polarization/depolarization asymmetry

Further inspection of Fig. 4.7 reveals another unexpected asymmetry; the saturation change in nuclear polarization ΔB_N for the polarizing transition $V_{DC} = 0 \rightarrow 2$ V does not match the value for the reverse transition, $V_{DC} = 2 \rightarrow 0$ V. However, as shown in Fig. 4.11, the relaxation time T_{1e} for both processes are identical to within the typical error of the measurement. Since the time scales match, our first suspicion was that there was a rapid process which occurred when the voltage is shut off that causes a loss of some fraction of the nuclear polarization, and the remaining polarization decays at T_{1e}. In order to address this possibility, we set out to develop a measurement which would be substantially faster than the Larmor magnetometry technique used here. The result of this effort was the development of the servo loop measurement technique which follows a zero crossing of the Faraday rotation

discussed in depth in Chapter 5.4.2.

The development of the Faraday rotation zero-crossing measurement technique led us to the discovery of the previously unrecognized phase shift which occurs in TRFR measurements due to the presence of previous pulses, which is the primary focus of the next chapter. Through a somewhat subtle mechanism, the polarization/depolarization asymmetry can be explained as resulting from this phase shift.

In order to improve the speed of measurements of the local magnetic field, we have used TRFR scans over a limited delay range, as shown in Fig. 4.6. By design, this measurement does not include more than a few precessions of the electron spin polarization. Fits to the precession frequency alone therefore contain a potentially large error. With only a narrow range of delay times, changes in magnetic field are difficult to distinguish from shifts in the phase of the TRFR signal. Having not recognized that a phase shift would be present, the fits of all TRFR scans were performed under the assumption that the signal should be purely cosinusoidal; that is, we assume zero phase shift. To ensure that this was the case, we carefully measure the delay line zero delay position. Fits to the limited range of delay times therefore contain a systematic error as a result of the phase shift introduced by previous pulses. Numerical calculations showing this are presented in Figure 4.12. Here, we plot the magnetic field measured by our experimental technique in Cross channel samples versus the set magnetic field using data for the spin lifetimes at 10 K at a range of voltages.

Fortunately, this invalid assumption introduces only a small error when the in-plane electric field is large. As will be shown in the next chapter, this is a result of the fact that spins from previous pulses are dragged out of the region of interrogation by the electron drift velocity. Errors in the magnetic field measurements at high voltage are only a few percent. At zero electric field, however, the correction will be larger. The errors are largest at low temperatures when the electron spin lifetime is long. At temperatures of 30 K and higher, the error due to phase shift is again only a few percent. Despite this effect, we expect the lifetime measured to be accurate, as the measured fields will differ from the real field by a

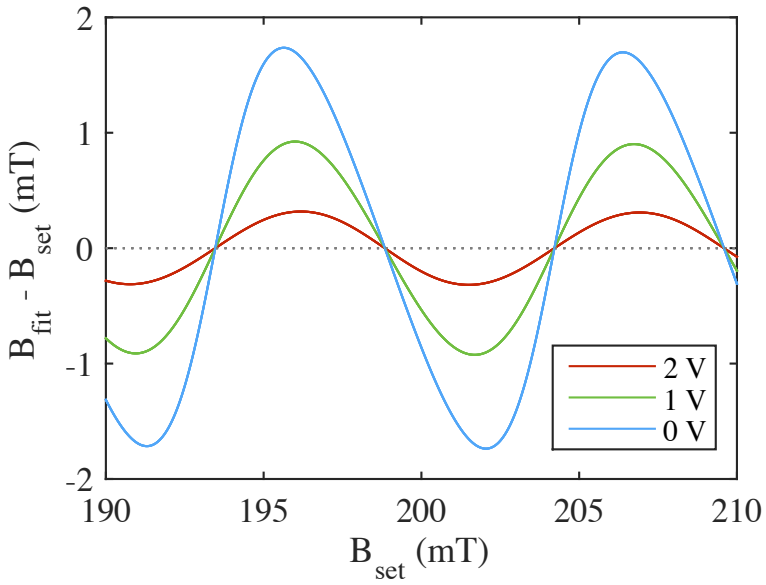

Figure 4.12: Results of fits to synthetically generated data using a limited delay range of 3–5 ns with 50 ps steps with no phase shift. Introduced error is minimal at high voltages due to the in-plane motion of optically injected spins and the decreased electron spin lifetime. The lifetimes used are 10, 8, and 6 ns for Voltages of 0, 1, and 2 V respectively. These values reflect typical measured values. The mobility is set to 5500 $\mathrm{cm^2V^{-1}s^{-1}}$, and pump and probe spot sizes are assumed to have a diameter of 30 μm.

slowly varying factor over the small changes in nuclear polarization. This is reflected in the close agreement of the measured T_{1e} polarization times.

Our understanding of this asymmetry was stymied by a peculiar fact about the measurements performed to attempt to characterize the asymmetry. Measurements of ΔB_N for transitions of $V_{DC} = 2 \rightarrow 0$ V were taken as a function of the applied magnetic field, with data collected at 50, 100, 150, and 200 mT. The results showed a roughly linear scaling of ΔB_N which was consistent for data at 50, 100, and 200 mT, but appeared anomalously large at 150 mT, as shown in Fig. 4.13. We now recognize this to be a result of the fact that the precession frequency of the electrons differs by precisely an octave as the field is increased from 50 to 100 mT and 100 to 200 mT. Accordingly, the error introduced by the phase shift is the same at these magnetic fields. At 150 mT the precession frequency does not differ by an integer number of octaves from the other measurements, so the introduced error is different than at the other magnetic field values used, which lead to the anomalously large

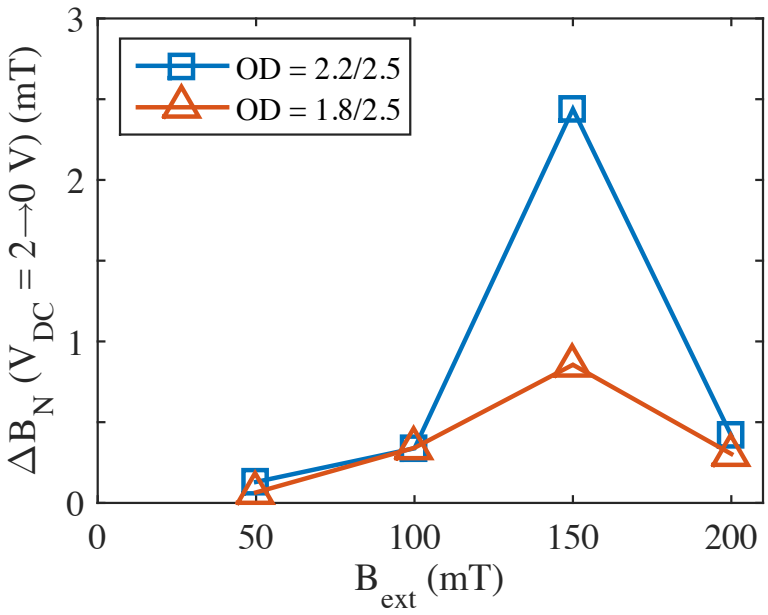

Figure 4.13: ΔB_N measured in transitions of $V_{DC} = 2 \rightarrow 0$ V vs. applied magnetic field at two different total beam powers. Optical densities (OD) in the legend refer to the pump and probe neutral density filters, respectively. The total beam power at OD 2.2/2.5 is approximately 600 μW and increases to approximately 1.35 mW at OD 1.8/2.5.

measured ΔB_N at that field value. Measurements were repeated with an increased pump and probe power by adjusting the pump neutral density filters to an optical density of 1.8 instead of 2.2, which increases its intensity by a factor of 2.5. As discussed in the following chapter, at higher optical intensity, the phase shift should be diminished due to the loss of spin polarization due to previous pulses from recombination following the arrival of the next pulse. The data taken at 150 mt is consistent with that process if the phase shift is indeed responsible for the anomalously high value of ΔB_N obtained.

Due to the error introduced by the phase shift, future measurements should use a more advantageous selection of delay time set points. Monte Carlo calculations have been performed which show that it is possible to remove this source of error without significantly increasing the time it takes to perform a TRFR scan by choosing more widely spaced delay set points over a broader range. This will suppress errors due to the phase shift. Results of these calculations are shown in Fig. 4.14. Here, we plot a histogram of fit magnetic fields from a sample of 125,000 simulated delay scans which include Gaussian noise similar to that

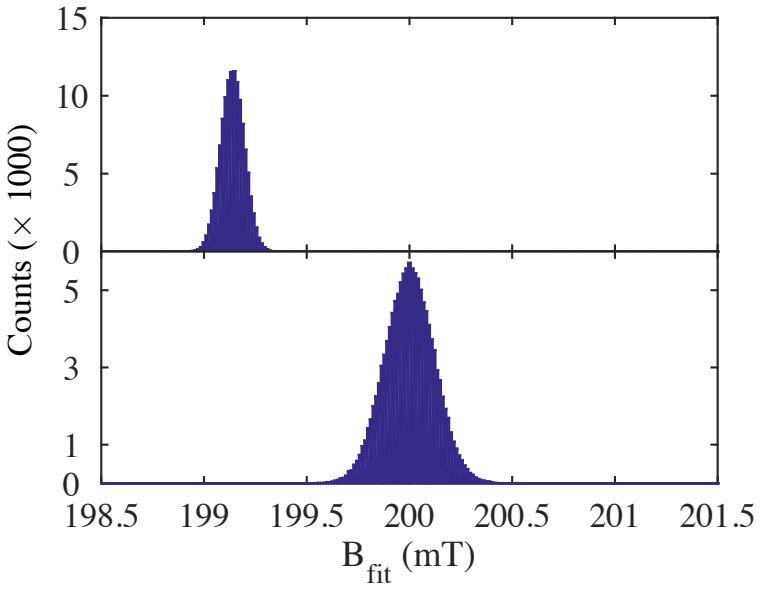

Figure 4.14: Monte Carlo simulations showing the results of fits to magnetic field using ΔT = 3000:50:5000 ps (top) and 150:150:6000 ps (bottom) with a set magnetic field of 200 mT. The extended range in delay set points used in the bottom delay scans removes the error introduced by the phase shift in TRFR measurements.

observed in the experimental setup. The upper panel shows data generated and fit using the delay set points used in the experimental data presented here; the delay is scanned in 50 ps steps from 3 ns to 5 ns. The lower panel uses delay steps of 150 ps scanning from 150 ps to 6 ns. These contain 41 and 40 measurements, respectively. Accordingly, they should not differ significantly in the length of time it takes to complete a delay scan. With the new delay set points, errors due to the phase shift are eliminated, and the standard deviation is comparable to the originally selected delay set points. Further optimization methods may be considered which improve the sensitivity and speed of these measurements.

4.6 Conclusion and future work

With the data presented here, we have demonstrated dynamic nuclear polarization resulting from current-induced electron spin polarization. We find that the observed saturation change in nuclear field ΔB_N is consistent with prior theoretical results, and that the nuclei relax primarily through the contact hyperfine interaction with the electron spin system. Fur-

thermore, the strength of the saturation magnetic field supports earlier measurements of the achievable polarization via CISP in this material. We also find that the nuclear polarization depends on the direction and magnitude of the current, mirroring prior measurements of CISP, and clarifying previous measurements of CISP-induced DNP in GaAs. The nuclear polarization time T_{1e} is found to be broadly consistent with theoretical estimates, though details of its temperature dependence are complicated by the various mechanisms which lead to relaxation.

We have additionally observed nuclear polarization mechanisms which depend on the magnitude of the applied electric field, but not its direction, through an asymmetry in ΔB_N when reversing the applied electric field. Two mechanisms are identified which would account for this asymmetry; depolarization due to the hot electron effect, and depolarization resulting from the generation of optical carriers by the pump and probe beams used to perform Larmor magnetometry.

Finally, we have discovered a previously unnoticed phase shift in TRFR measurements resulting from spins polarized by previous pump pulses. This discovery will be described in detail in the following chapter. While the phase shift complicates the interpretation of some results, a clear path towards removing this complication in future measurements is identified.

From the results presented here, three avenues for future measurements are suggested. Importantly, these measurements should be performed using techniques that account for the phase shift in TRFR. Using these techniques, measurements of transitions of the form $V_{DC} = 0 \rightarrow \pm$V and $V_{DC} = \pm V \rightarrow 0$ V should be performed to confirm that the observed asymmetry in ΔB_N for these transitions does in fact result from the TRFR phase shift, and that this is not a real effect.

Second, measurements of ΔB_N for transitions with CISP perpendicular to the applied magnetic field should be performed as a function of the total pump and probe beam powers and electric field strength . These measurements should allow for the contribution to DNP in this geometry from the hot electron effect and optically injected carriers to be isolated.

Finally, an attempt could be made to perform all-electrical NMR using the cross channels. This could be done by using current along $\hat{y}$ to generate a nuclear polarization, and an alternating current along $\hat{x}$ to excite an alternating current-induced spin polarization perpendicular to the nuclear polarization. When the AC current frequency is in resonance with a nuclear spin transition, the Knight field resulting from the electrons may be able to resonantly depolarize a single nuclear species. This measurement would share features with the all-optical nuclear magnetic resonance measurements performed in Refs. [63] and [65].

CHAPTER V

Phase effects due to previous pulses

5.1 Introduction

In Chapter III, it was shown that when the electron spin lifetime is on the order of, or longer than, the repetition rate of the laser, the contribution to the Faraday rotation angle of the probe pulse due to previous pump pulses must be included. This fact has lead to the development of measurements based on resonant spin amplification (RSA)[51, 52, 53]. In RSA measurements, the pump-probe delay time Δt is held constant, typically at a small negative[1] value, and the Faraday rotation is monitored as the external magnetic field is swept.

In addition to modifying the field-dependent Faraday rotation angle, previous pulses can also modify time-resolved Faraday rotation (TRFR) measurements. In TRFR scans, the previous pulses modify the amplitude of the observed Faraday rotation, as well as introduce an effective phase shift of the signal. In this chapter, I will discuss this phase shift, which is present when the electron spin polarization lifetime T_2^* is comparable to or larger than the repetition time of the laser. First, analytic expressions for the phase shift are derived from previous expressions used in resonant spin amplification (RSA). The implications of this phase shift are explored numerically and in experimental data. Measurements designed to make use of this effect are then introduced and discussed in numerical simulations. Finally,

[1] Negative here indicates that the probe pulse arrives before the pump pulse

situations in which assumptions made in the derivation of the analytical expressions fail will be explored, and steps required to make sense of TRFR data in those cases are outlined. The contents of this chapter are largely based upon work first published in Ref. [89].

5.2 Derivation

We start with the result of chapter III, where it was shown that once initialized, a spin polarization initially along $\hat{z}$ will precess around the total magnetic field at the Larmor precession frequency $\Omega_L = g\mu_B B/\hbar$ where g is the electron g-factor, μ_B is the Bohr magneton, and $\hbar$ is the reduced Planck constant, and decay with a lifetime given by the inhomogeneous dephasing time T_2^*. This results in an out-of-plane spin polarization of the form:

$$s_{\hat{z}}(\Delta t) = S_0 \cos\left(\frac{g\mu_B B}{\hbar}\Delta t\right) e^{-\Delta t/T_2^*} \tag{5.1}$$

where S_0 is the degree of the initial spin polarization along $\hat{z}$. In this expression, we take Δt to be positive, which ensures causality. For long spin lifetimes, one must include the contribution of all previous pulses, each of which precesses at Ω_L and decays with lifetime T_2^*. This gives rise to the following expression for the total $\hat{z}$ component of the spin polarization:

$$s_{\hat{z}} = \sum_{n\geq 0} S_0 \cos\left(\Omega_L(\Delta t + nT_{\text{rep}})\right) \exp\left[-\frac{(\Delta t + nT_{\text{rep}})}{T_2^*}\right] \tag{5.2}$$

where T_{rep} is the laser repetition time.

For the following analysis, it is helpful to introduce a complex spin phasor $\underline{\text{s}}$ in place of the vector quantity $\vec{s}$ or the $\hat{z}$ component $s_{\hat{z}}$ used previously. Here, we take $s_{\hat{z}}$ to be the real part of $\underline{\text{s}}$, $\text{Re}(\underline{\text{s}})$, and $s_{\hat{y}}$ to be the imaginary part $\text{Im}(\underline{\text{s}})$. Within this framework, the signal due to a single pump pulse as a function of delay time is given by:

$$\underline{\text{s}}(\Delta t) = S_0 \exp\left[(i\Omega_L - 1/T_2^*)\Delta t\right] \tag{5.3}$$

When the sum found in Eq. 5.2 is rewritten in phasor notation, it becomes:

$$\underline{s}(\Delta t) = \sum_{n\geq 0} S_0 \exp\left[(i\Omega_L - 1/T_2^*)(\Delta t + nT_{rep})\right] \tag{5.4}$$

While this expression is sufficient to fully describe the spin polarization, it can be simplified to a closed form which offers greater insight into the behavior of the system. First, we factor out of the sum all the terms which do not depend on n, giving:

$$\underline{s}(\Delta t) = S_0 \exp\left[(i\Omega_L - 1/T_2^*)\Delta t\right] \sum_{n\geq 0} \exp\left[(i\Omega_L - 1/T_2^*)nT_{\text{rep}}\right] \tag{5.5}$$

We can immediately identify some important results within this expression. All of the dependence on Δt has been factored out of the sum, which means that the value of the sum is constant in Δt. We define this constant, which is in general complex, to be:

$$\sum_{n\geq 0} \exp\left[(i\Omega_L - 1/T_2^*)nT_{rep}\right] = re^{i\phi} \tag{5.6}$$

where the modulus r and argument ϕ are functions of T_2^*, Ω_L, and T_{rep}. We also see that the total spin polarization behaves in the same way as that of an individual pulse; that is, it decays with lifetime T_2^* and precesses at Ω_L.

The contribution from previous pulses results in a constant multiplicative factor, $re^{i\phi}$, in the expression. Inserting Eq. 5.6 into Eq. 5.4, we arrive at the following simple form for the total spin phasor:

$$\underline{s}(\Delta t) = rS_0 \exp\left[(i\Omega_L - 1/T_2^*)\Delta t + i\phi\right] \tag{5.7}$$

Taking the real part of this to find $s_{\hat{z}}$, we get:

$$s_{\hat{z}}(\Delta t) = rS_0 \cos(\Omega_l \Delta t + \phi) e^{-\Delta t/T_2^*} \tag{5.8}$$

From this it can be seen that previous pulses have two effects – they modify the apparent

amplitude of the spin polarization and contribute a phase shift to the precessing term.

We now seek to find closed-form expressions for r and ϕ, as defined in Eq. 5.6. Fortunately, the sum is in the form of a geometric series, the value of which is given by:

$$\sum_{n\geq 0} \rho^n = \frac{1}{1-\rho} \leftrightarrow |\rho| < 1 \tag{5.9}$$

Here, ρ is referred to as the common ratio. Rewriting the sum in this form, we arrive at:

$$\sum_{n\geq 0} \Big(\exp\left[(i\Omega_L - 1/T_2^*)T_{rep}\right] \Big)^n \tag{5.10}$$

where the common ratio is easily identifiable as:

$$\rho = \exp[(i\Omega_L - 1/T_2^*)T_{rep}] \tag{5.11}$$

At this point, for the sake of readability, we introduce two substitutions:

$$\Theta = \Omega_L T_{rep} \tag{5.12}$$

$$x = T_{rep}/T_2^* \tag{5.13}$$

so that $\rho = e^{i\Theta - x}$. The geometric sum converges only if $|\rho| < 1$,which is satisfied so long as T_2^* is positive and finite, which is the case in experimental systems. Using Eq. 5.9, we have:

$$\sum_{n\geq 0} \exp(i\Theta - x)^n = \frac{1}{1-e^{i\Theta - x}} \equiv \underline{\mathrm{C}} \tag{5.14}$$

We now look for r and ϕ which satisfy:

$$re^{i\phi} = \frac{1}{1-e^{i\Theta - x}} = \underline{\mathrm{C}} \tag{5.15}$$

The complex number $\underline{\mathrm{C}}$ can be expressed in the polar coordinates r and ϕ using the following

equations:

$$r = \sqrt{\mathrm{Re}(\underline{\mathrm{C}})^2 + \mathrm{Im}(\underline{\mathrm{C}})^2} \tag{5.16}$$

$$\phi = \tan^{-1}\left(\frac{\mathrm{Im}(\underline{\mathrm{C}})}{\mathrm{Re}(\underline{\mathrm{C}}}\right) \tag{5.17}$$

We therefore begin by calculating the real and imaginary parts of the right-hand side of Eq. 5.15. These can be found from:

$$\mathrm{Re}(\underline{\mathrm{C}}) = \frac{\underline{\mathrm{C}} + \underline{\mathrm{C}}^*}{2} \tag{5.18}$$

$$\mathrm{Im}(\underline{\mathrm{C}}) = \frac{\underline{\mathrm{C}} - \underline{\mathrm{C}}^*}{2i} \tag{5.19}$$

Starting with the real part:

$$\begin{aligned}
\mathrm{Re}(\underline{\mathrm{C}}) &= \frac{1}{2}\left(\frac{1}{1 - e^{i\Theta - x}} + \frac{1}{1 - e^{-i\Theta - x}}\right) && (5.20)\\
&= \frac{1}{2}\left[\frac{(1 - e^{-i\Theta - x}) + (1 - e^{i\Theta - x})}{1 - e^{-x}(e^{i\Theta} + e^{-i\Theta}) + e^{-2x}}\right] && (5.21)\\
&= \frac{1}{2}\left[\frac{2 - e^{-x}(e^{i\Theta} + e^{-i\Theta})}{1 - e^{-x}(e^{i\Theta} + e^{-i\Theta}) + e^{-2x}}\right] && (5.22)
\end{aligned}$$

From the Euler equation, we have:

$$\begin{aligned}
\frac{e^{i\theta} + e^{-i\theta}}{2} &= \cos\theta && (5.23)\\
\frac{e^{i\theta} - e^{-i\theta}}{2i} &= \sin\theta && (5.24)
\end{aligned}$$

Substituting in these definitions for sine and cosine, we find:

$$\mathrm{Re}(\underline{\mathrm{C}}) = \frac{1 - e^{-x}\cos\Theta}{1 - 2e^{-x}\cos\Theta + e^{-2x}} \tag{5.25}$$

Repeating the above steps to find the imaginary part, we arrive at:

$$\mathrm{Im}(\underline{\mathrm{C}}) = \frac{e^{-x}\sin\Theta}{1 - 2e^{-x}\cos\Theta + e^{-2x}} \tag{5.26}$$

Using Eqns. 5.26 and 5.25, in conjunction with Eq. 5.16, the analytic closed-form expression for r is found to be:

$$r = \sqrt{\left[\frac{1 - e^{-x}\cos\Theta}{1 - 2e^{-x}\cos\Theta + e^{-2x}}\right]^2 + \left[\frac{e^{-x}\sin\Theta}{1 - 2e^{-x}\cos\Theta + e^{-2x}}\right]^2} \tag{5.27}$$

$$r = \frac{1}{1 - 2e^{-x}\cos\Theta + e^{-2x}}\sqrt{1 - 2e^{-x}\cos\Theta + e^{-2x}(\cos^2\Theta + \sin^2\Theta)} \tag{5.28}$$

$$r = (1 - 2e^{-x}\cos\Theta + e^{-2x})^{-\frac{1}{2}} \tag{5.29}$$

We see that r is maximized for a given lifetime (corresponding to a particular value of x) when $\cos\Theta$ is maximized, *i.e.* when $\Omega_L T_{rep} = 2n\pi$ where n is an integer. This condition corresponds to the case when an integer number of full precessions of the spin polarization occur within the laser repetition time. Conversely, r is minimized when $\Omega_L T_{rep} = (2n{+}1)\pi/2$, corresponding to half-integer precession within the laser repetition time. As expected from the canonical geometric series results, in the limit of infinite spin lifetime ($x \to 0$), we find $r|_{\Theta=2n\pi} = \infty$ and $r|_{\Theta=(2n+1)\pi/2} = 1/2$.

Figure 5.1 panels (a) and (b) summarize the behavior of r throughout parameter space. The traces in panel (b) correspond to line cuts of the surface plot in panel (a) at particular values of x. Note that x is inversely proportional to T_2^* so that as T_2^* goes to infinity x approaches zero.

We now move on to consider the closed-form expression for ϕ. Combining Eqns 5.25,5.26, and 5.17, we immediately arrive at:

$$\phi = \tan^{-1}\left[\frac{e^{-x}\sin\Theta}{1 - e^{-x}\cos\Theta}\right] \tag{5.30}$$

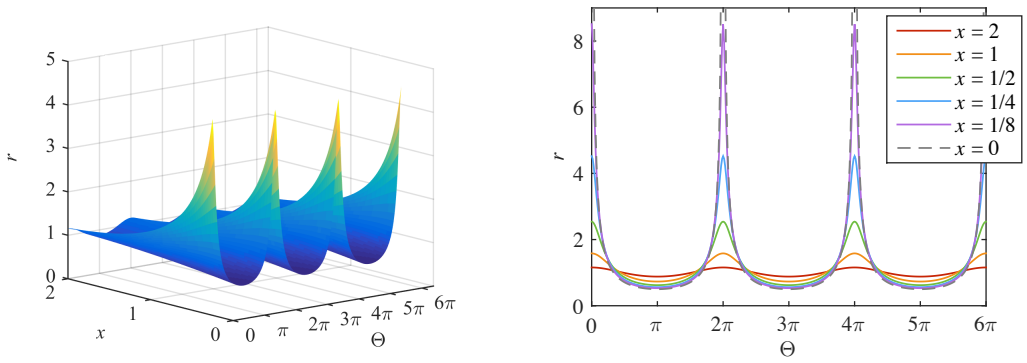

(a) r vs. x and Θ (b) r vs. Θ for various values of x

Figure 5.1: (a) Surface plot of amplitude r as a function of x and Θ. As the ratio of the spin lifetime to the laser repetition time grows (corresponding to a decrease in x), resonance peaks grow larger and sharper. (b) Line cuts of the surface plot in (a) taken at a logarithmic range of values of x. The maximum value of r diverges as x goes to zero, and its minimum value converges to 1/2.

The first thing that this expression tells us is that the phase shift ϕ is limited to be within the range $[-\pi/2, \pi/2]$, and that these extremal values are only obtained at infinite lifetime. Also, this function exhibits odd symmetry, so that $\phi(-\Theta) = -\phi(\Theta)$. This will become important later when experimental data is considered, since the materials considered within this study exhibit a negative electron g factor. Further intuition into this expression can be gained by considering plots of ϕ throughout parameter space. These plots are found in Fig. 5.2 panels (a) and (b). Again, the traces in panel (b) correspond to line cuts across the surface plotted in panel (a) at particular values of x. As expected, the maximum and minimum values of ϕ increase with T_2^*, and reach their limiting values of $\pm\pi/2$ at $x = 0$. Rather less intuitively, we find that at large T_2^*, ϕ shifts slowly as Θ is swept between peaks of r, and then flips rapidly as the peak is passed. Correspondingly, the values of Θ at which ϕ is extremized move closer to resonance peaks.

Combining Eqn.5.8 with the analytic expressions for r and ϕ in Eqns. 5.29 and 5.30, we have now arrived at a closed-form expression for $s_z(\Delta t)$. We note that this is not the first derivation of a closed form expression for Eqn. 5.2. For instance, the following equation is

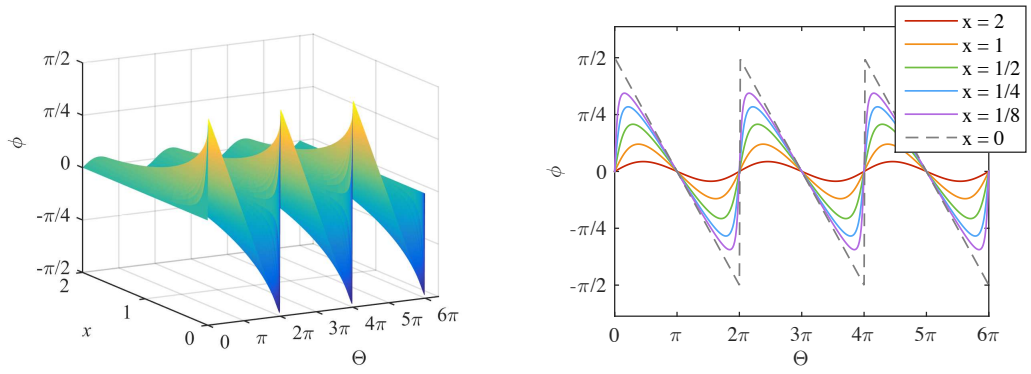

(a) ϕ vs. x and Θ (b) ϕ vs. Θ for various values of x

Figure 5.2: (a) Surface plot showing ϕ as a function of x and Θ, showing the transition from sinusoidal to sawtooth behavior as the value of x decreases. (b) Line cuts of the surface plot in (a) taken over a logarithmic range of values of x. As x decreases, the phase shift across RSA peaks (corresponding to $\Theta = 2n\pi$) occurs increasingly rapidly and the maximum phase shift approaches $\pm\pi/2$.

adapted into the notation used in this dissertation from Ref. [90]:

$$s_z(\Delta t) = \frac{s_0}{2}\exp\left[-\frac{\Delta t + T_{rep}}{T_2^*}\right]\frac{\cos(\Omega_L \Delta t) - e^{T_{rep}/T_2^*}\cos\left[\Omega_L(\Delta t + T_{rep})\right]}{\cos(\Omega_L T_{rep}) - \cosh(T_{rep}/T_2^*)} \tag{5.31}$$

However, this expression, which is derived in the context of RSA measurements which are usually done at small negative time delays, is only valid over the interval $\Delta t \in [-T_{rep}; 0)$. Under a suitable variable substitution, Equations 5.31 and 5.8 are functionally identical. Eqn. 5.8, however, has a simpler form that provides greater intuition, makes the presence of the phase shift explicit, and allows for the immediate calculation of the in-plane spin polarization for free by taking the imaginary part of Eqn. 5.7 instead of the real part.

Next, we seek to find an expression for the maximum magnitude of the phase angle ϕ versus x, as well as the values of Θ at which the extrema occur. We start by finding critical points in $\phi(\Theta, x)$. However, since $\tan^{-1}(\alpha)$ increases monotonically with α, we can search for extrema of the argument of the $\tan^{-1}$ function instead of the full expression for ϕ. The equation for the critical points becomes:

$$\frac{d}{d\Theta}\frac{e^{-x}\sin\Theta}{1 - e^{-x}\cos\Theta} = \frac{e^{-x}\cos\Theta}{1 - e^{-x}\cos\Theta} - \frac{e^{-2x}\sin^2\Theta}{(1 - e^{-x}\cos\Theta)^2} = 0 \tag{5.32}$$

Simplifying the equality on the right hand side of the above expression, we get:

$$\begin{aligned}\cos\Theta &= \frac{e^{-x}\sin^2\Theta}{1-e^{-x}\cos\Theta} \\ \cos\Theta &= e^{-x}(\sin^2\Theta+\cos^2\Theta) \\ \cos\Theta &= e^{-x} \end{aligned} \tag{5.33}$$

Since $\cos\Theta$ is 2π-periodic in Θ and exhibits even symmetry, we find the equation for the locations of the critical points to be:

$$\Theta_{extr} = 2n\pi \pm \cos^{-1}(e^{-x}) \tag{5.34}$$

This confirms the observations from Fig. 5.2, which is that as T_2^* increases, the value of Θ at which ϕ is extremized moves closer to the resonance peaks at $\Theta = 2n\pi$.

Now we seek an expression for the maximum phase angle as a function of x, which requires that we plug the result in Eq. 5.34 into Eq. 5.30. For simplicity, we pick $n = 0$ and the positive solution but the result we find will be general to all values of n up to the sign of the phase shift. We have:

$$\phi_{extr} = \tan^{-1}\left[\frac{e^{-x}\sin(\cos^{-1}e^{-x})}{1-e^{-x}\cos(\cos^{-1}e^{-x})}\right] \tag{5.35}$$

We now apply the trigonometric identity:

$$\sin(\cos^{-1}\alpha) = \sqrt{1-\alpha^2} \tag{5.36}$$

Plugging this in and simplifying Eq. 5.35, we find:

$$\phi_{extr} = \tan^{-1}\left[\frac{e^{-x}}{\sqrt{1-e^{-2x}}}\right] \tag{5.37}$$

The result in Eq. 5.37 is plotted as a function of $1/x$ in Fig. 5.3. ϕ_{extr} is plotted versus $1/x$ so that the independent variable is proportional to T_2^* instead of its inverse.

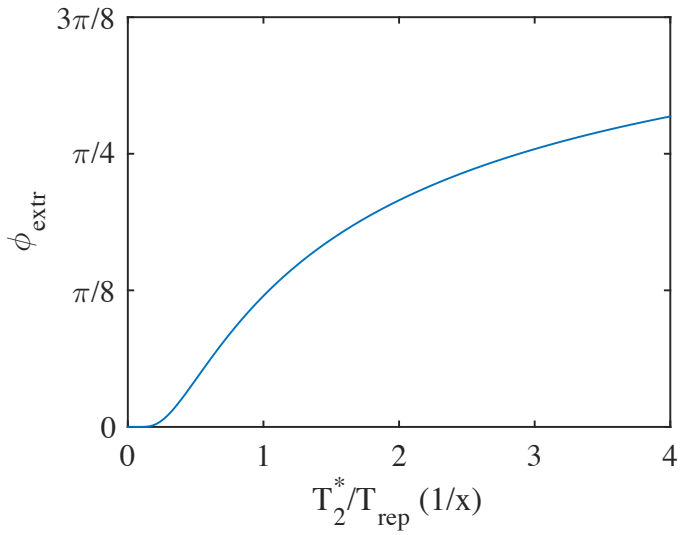

Figure 5.3: Extremal value of the apparent phase shift ϕ_{extr} as a function of $1/x$. By inverting this relationship, a measurement of the maximum phase angle can be used to determine the spin lifetime.

5.3 Experimental data

In order to verify the analysis up to this point, an experimental data set was collected. Data were taken on a commercially purchased sample consisting of a 2 μm layer of n-GaAs doped at 1×10^{17} cm^{-3} atop a semi-insulating GaAs substrate. Measurements were performed at 10 K as a function of external magnetic field B_{ext} and pump-probe delay time Δt. The laser was tuned to $\lambda = 818.2$ nm, and has a repetition time of 13158 ps. For this data, the pump and probe beam powers were measured to be 500 μW and 75 μW, respectively, and the beam diameters were found to be approximately 35 μm each. These data were generated by collecting the reflected probe beam, and are therefore considered to be Kerr rotation measurements.

Results are plotted in Fig. 5.4. In this figure the magnitude of the signal shown is in millivolts as measured on a lock-in amplifier, which is taken to be an arbitrary unit proportional to the Kerr rotation angle. The data set was then fit to extract the electron g factor and spin lifetime. The fit used simultaneously fits to the entire data set; that is, the entire 2-dimensional data set is fit at once to the real part of 5.4 with a term added which

takes into account the contribution from optically excited carriers before recombination, which decays rapidly. In total, the fit equation used is:

$$\theta_f = \mathrm{Re}\left\{\sum_{n\geq 0} S_0 \exp[(i\Omega_L - 1/T_2^*)(\Delta t + nT_{rep})]\right\} + A_O \cos(\Omega_L \Delta t)\exp[\Delta t/T_O] \times \Theta(\Delta t) \tag{5.38}$$

The fit finds $g = -0.3788$ [2], $T_2^* = 10.2$ ns, and optical spin lifetime $T_O = 87$ ps. The ratio of Faraday rotation from long-lived spins to spins from optical carriers, A/A_O, is found to be 2.0. Figure 5.4 (b) shows computed data using the results of the fit. Both plates in Fig. 5.4 have been normalized using the same normalization factor. The close agreement between the experimental and model data is clearly shown in this figure; aside from the presence of some small noise in the experiment, the model is virtually indistinguishable from the experimental data.

The primary challenge faced when attempting to use a simultaneous fit is maintaining the stability of the experimental setup over the roughly 2 hours it takes to collect this data. Temperature and humidity fluctuations in the lab must be minimized, and the cryostat and optics must be allowed to equilibrate for a considerable amount of time, typically about 2 hours, after turning on the laser and electronics. Changes in pump-probe overlap, laser power, and motion of the sample relative to the optical beams must be constant throughout the experiment to avoid a time-dependent amplitude factor, which complicates and corrupts the result of fits to the data. The ability to maintain stability over this long a time is thanks to the diligent work of everyone in the lab in building a stable and robust experiment.

In order to test the validity of the above analysis, the data is fit again as a series of delay scans. At each value of the external magnetic field, a delay scan is performed and the resulting data is fit to the functional form found in Eq. 5.8, and the values of r, ϕ, Ω_L, and T_2^* are extracted. The results of these fits are plotted in Fig. 5.5, along with the expected values

[2]The sign is assumed to be negative in accordance with literature values, as this measurement cannot fix the sign of the g factor

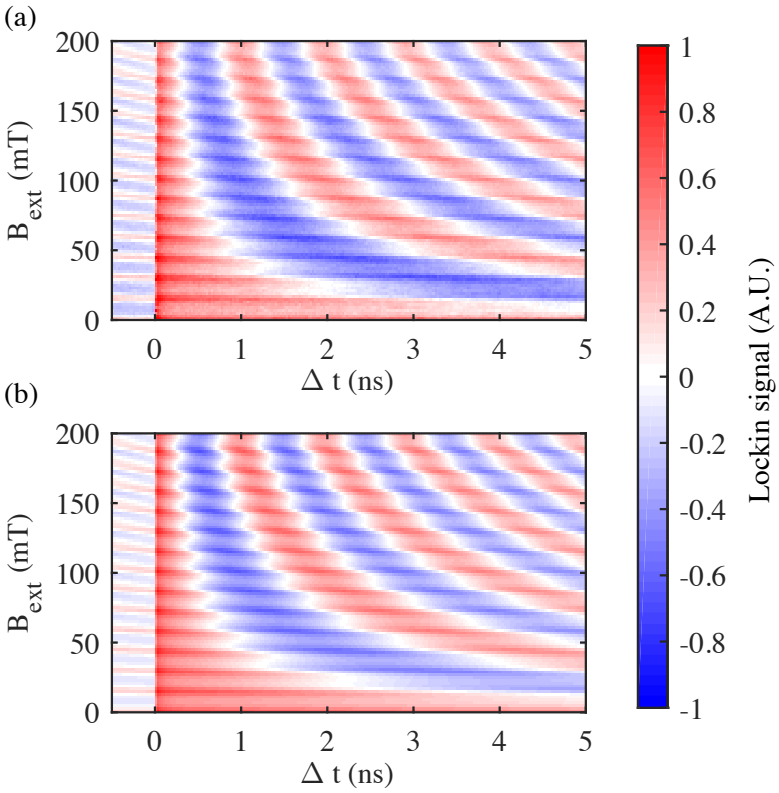

Figure 5.4: Normalized lock-in signal (proportional to Faraday rotation angle θ_f) as a function of delay time Δt (horizontal axis) and external magnetic field B_{ext} (vertical axis) for experimental data (a) and data generated using Eq. 5.38 with fit parameters from experimental data (b).

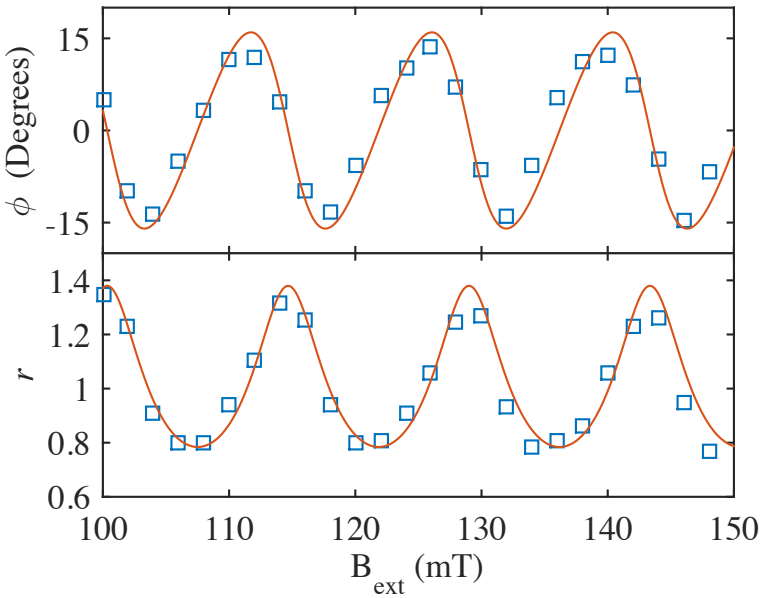

Figure 5.5: Phase shift ϕ (top) and amplitude r (bottom) versus magnetic field for experimental data (blue squares) and model (red traces). The experimental data shows close agreement with the model, which has only two free parameters, T_2^* and g.

for r and ϕ given the values of g and T_2^* determined from the simultaneous fit above. The experimental data agrees closely with the theoretical values within this range of magnetic fields. At lower magnetic fields, the slow Larmor precession frequency adversely affects the accuracy of the fits. Within the plotted range (corresponding to external magnetic fields of 100 to 150 mT) the maximum observed phase angle is 16.4°.

5.4 Measurements using resonant phase shift

5.4.1 Measuring spin lifetime

Thanks to its monotonic behavior, equation 5.37 can be inverted, so that knowledge of the maximum phase shift can be used to calculate a corresponding value of x, and by extension, T_2^*. Inverting Eq. 5.37, we find the following:

$$x = \ln\left[\frac{\sqrt{1+\tan^2\phi_{extr}}}{\tan\phi_{extr}}\right] \tag{5.39}$$

The maximum observed phase angle in the preceding section of 16.4°, used in conjunction with Eq. 5.39, can be used to calculate T_2^*, which gives a value of 10.4 ns. This is in good agreement with the value found in the simultaneous fit discussed above, which was 10.2 ns. In this calculation, we have simply taken the largest observed phase angle measured within the data set collected. Because of the duration of data collection for such a large data set, this is not an efficient way to measure T_2^*, especially when compared to the other available techniques including TRFR and RSA measurements.

Fortunately, it is possible to systematically find a value of the magnetic field which produces a condition of maximum phase without resorting to performing numerous delay scans. This can be done because, as we will show, at a condition of maximum phase, the sum of all previous pulses lies in the sample plane when the next pulse arrives. That is, $s_z(\Delta t = 0^-) = 0$. Since Eq. 5.8 is valid over the interval $\Delta t \in (0, T_{rep})$, we must use the fact that, since each pulse contributes a spin polarization S_0, $s_z(0^+) - s_z(0^-) = S_0$.

Equation 5.37 gives the condition at which a maximum phase angle is reached for a given value of x;

$$\Theta_{extr} = 2n\pi \pm \cos^{-1}(e^{-x})$$

Since the sine and cosine functions in which Θ appears are 2π periodic, we can again pick $\Theta_{extr} = \pm\cos^{-1}(e^{-x})$ without loss of generality.

Evaluating Eq. 5.8 at $\Delta t = 0^+$ yields:

$$s_z(\Delta t = 0^+) = rS_0\cos(\phi) \tag{5.40}$$

Substituting $\Theta_{extr} = \pm\cos^{-1}(e^{-x})$ into Equations 5.29 and 5.30 above, we find:

$$r = \frac{1}{\sqrt{1 - e^{-2x}}} \tag{5.41}$$

$$\cos(\phi) = \sqrt{1 - e^{-2x}} \tag{5.42}$$

Inserting these into Eq. 5.40 gives:

$$s_z(\Delta t = 0^+)|_{\phi_{extr}} = S_0 \tag{5.43}$$

Since, as is discussed above, $s_z(0^+) - s_z(0^-) = S_0$, we arrive at:

$$s_z(\Delta t = 0^-)|_{\phi_{extr}} = 0 \tag{5.44}$$

Accordingly, the sum of the previous pulses must lay in the sample plane, as it has no component along $\hat{z}$. This situation is shown schematically in Fig. 5.6, which shows spin polarization immediately following the arrival of a pump pulse ($\Delta t = 0^+$) at a condition of extremized phase. Here, the contribution to the total spin polarization from the 7 most recent pump pulses is shown in blue, while the total spin polarization is shown in red. All vectors are normalized to the initial spin polarization S_0. Accordingly, the most recent pulse is shown by the vector of length 1 pointing along $\hat{z}$. The green arrow shows the sum of previous pulses but excluding the most recent pulse. This is equal to the spin polarization immediately preceding the arrival of the pump pulse, $\vec{s}(\Delta t = 0^-)$, and confirms that this polarization lies in the sample plane and that $s_{\hat{z}} = 0$. This data has been generated using $x = 1/2$, or $T_2^* = 2T_{rep}$.

With the fact that $s_{\hat{z}}(\Delta t = 0^-)|_{\phi_{extr}} = 0$ in mind, we can systematically find the maximum phase angle using the following steps:

1. Set the pump-probe delay time to a small negative value.

2. Tune the magnetic field so that the Faraday or Kerr rotation signal is midway between its maximum and minimum values. Doing this instead of finding the zero point removes any DC offset in the Faraday rotation signal.

3. Perform a delay scan and fit it to extract the phase angle ϕ

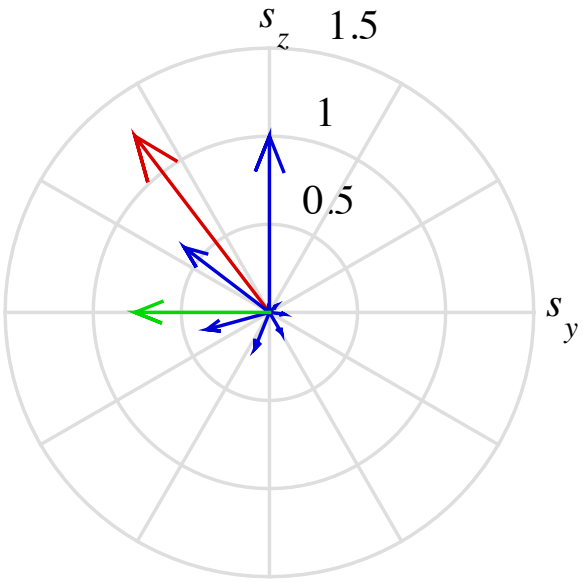

Figure 5.6: Diagram representing the orientation of the total spin polarization (red), the contribution from the first 7 terms in the sum found in Eq. [needed] (blue), and the sum excluding the most recent pulse (green).

4. Use this maximum phase angle in conjunction with Eq. 5.39 to calculate the lifetime T_2^*.

The sensitivity of such a measurement to the lifetime will depend on the ratio of T_2^* to T_{rep}. This is readily apparent when considering Fig. 5.6. For low values of this ratio below 1/3, the phase remains near zero, making a measurement of ϕ_{extr} useless as a means to determine T_2^*. Fortunately, this is the range in which fits to TRFR data are most useful. As T_2^*/T_{rep} increases past about 1/3, ϕ_{extr} begins to increase rapidly, yielding the highest sensitivity measurement, before eventually leveling off as it approaches its maximum value. It is within the region where the derivative of ϕ_{extr} with respect to T_2^* is large that this measurement is most useful. If T_{rep} can be chosen (for instance, by using a pulse picker) then the repetition rate should be chosen accordingly. Within this range, the chief difficulty lies in effectively choosing a magnetic field which maximizes ϕ. Once this magnetic field is settled upon, so long as a sufficient number of precessions of the electron spin polarization can be measured within the range of the delay line, fitting ϕ is straightforward.

5.4.2 Phase effects in Larmor magnetometry

Time-resolved Faraday/Kerr rotation can be used to measure the local magnetic field in which a spin polarization is found through a process dubbed Larmor Magnetometry [63]. In a typical Larmor magnetometric measurement, a time-resolved Faraday rotation measurement is performed and the electron precession frequency is extracted from a fit to the data. Since the Larmor precession frequency Ω_L is proportional to the magnetic field about which the electrons precess, if the g-factor is known the magnetic field can be calculated. This technique is used extensively in the study of dynamic nuclear polarization found in Chapter IV

While this technique allows for precise localized measurements of one component of a magnetic field, it has some limitations in practice. First, each time the magnetic field is measured a delay scan must be completed. This generally requires on the order of 10-100 seconds, which limits the temporal resolution for measuring fields which change more quickly. Second, since at least a few full precessions of the electron spin polarization must occur within the delay scan for a successful fit to the precession frequency, this technique is of limited use when the field is too small.

If all that is required of the measurement is to determine that a magnetic field has changed instead of determining a precise value (such as in the detection of a resonance condition), the first of these drawbacks can be avoided. Such a measurement is performed in Ref. [65] by simply monitoring the Faraday rotation signal continuously. A shift in magnetic field will result in a shift in precession frequency, changing the observed Faraday rotation. This technique is not ideal for uniquely determining the magnetic field for two reasons. First, when θ_F is at a local maximum with respect to B, the derivative goes to zero, which means small changes in the magnetic field around that point cannot be detected. Related to this fact, Θ_F does not exhibit a one-to-one relationship with the magnetic field, so that a particular measurement of θ_F cannot be related back to the local magnetic field by itself. The second major drawback is that this measurement cannot differentiate drift in laser power or pump-probe overlap from a change in magnetic field. For these reasons, this measurement is used

in Ref. [65] only to detect the presence of a resonance condition, and not the magnitude of the concomitant change in magnetic field.

The first problem discussed in the preceding paragraph can be avoided if only small changes in magnetic field around a zero crossing of known order of the Faraday rotation signal are considered. Near a zero crossing, $d\theta_F/dB$ is maximized and changes slowly, and drifts in overlap or power result in a proportionally smaller error in the magnetic field measurement. In fact, if the Faraday rotation signal is at a zero crossing of known order, the field is uniquely determined and variations in laser power and pump-probe overlap are eliminated entirely. This fact suggests a new approach: instead of continuously monitoring θ_F at a fixed delay time, continuously adjust the time delay such that the Faraday rotation is held as close to zero as possible. Then, if the g-factor and crossing order are known, the magnetic field can be calculated from the delay time at which the zero crossing occurs, and measurements can be taken as quickly as the delay line can be moved and a few lock-in time constants elapse.

A Faraday rotation zero-crossing will occur when $s_{\hat{z}} = 0$. That is,

$$s_{\hat{z}} = rS_0 \cos(\Omega_L \Delta t + \phi) \exp[-\Delta t/T_2^*] = 0 \tag{5.45}$$

This will occur when the cosine term goes to zero, which occurs when the following is satisfied:

$$\Omega_L \Delta t + \phi = \frac{(2n+1)\pi}{2} \tag{5.46}$$

The presence of ϕ in this equation complicates matters, and more so at longer lifetimes. This is most easily seen in Fig. 5.7, which plots the delay time of the 15th (left) and 6th (right) zero-crossings versus magnetic field for a number of lifetimes. As the lifetime increases, the behavior of the zero crossing delay time becomes dominated by the rapid shift in phase when an RSA peak is crossed. In fact, as is visible in the $n = 6$ plot, at long lifetimes the zero crossing delay time ceases to have a one-to-one correspondence to the associated magnetic

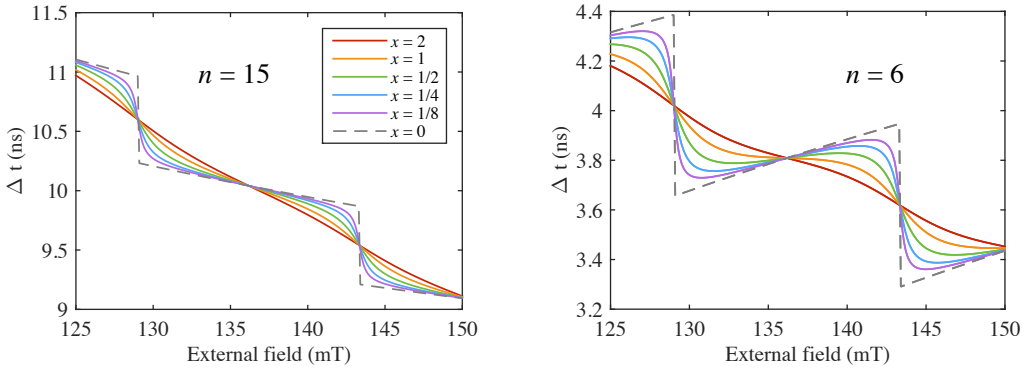

(a) 15^{th} crossing (b) 6^{th} crossing

Figure 5.7: Delay times corresponding to the 15th (left) and 6th (right) zero crossing of the Faraday rotation signal versus external magnetic field for a range of values of x. Even at infinite lifetime (corresponding to $x = 0$), zero crossing time exhibits a monotonic dependence on external magnetic field for $n = 15$ and other crossings where $\Delta t\, T_{rep}/2$. As the lifetime grows, monotonic dependence is lost for zero crossings which occur at delay times less than half the laser repetition time, such as the $n = 6$ crossing.

field. This behavior is not, however, present in the $n = 15$ plot. This is due to the fact that the 15^{th} zero crossing occurs at a much larger pump-probe delay time than the 6^{th} crossing at the experimental parameters used in generating this data.

Here, we will show that for all values of x, so long as the zero crossing being followed occurs at a delay time greater than half the laser repetition time, a one-to-one correspondence between zero crossing delay time and external magnetic field is maintained. To show this, we consider how the two terms in the argument of the cosine in Eq. 5.45, given by $\Omega_L \Delta t + \phi$, change with magnetic field. In the worst-case scenario of $x = 0$, we see from Fig. 5.2 panel (b) that between RSA peaks (at $\Theta = 2n\pi$), the derivative of ϕ with respect to Θ is constant:

$$\frac{d\phi}{d\Theta} = \frac{\Delta\phi}{\Delta\Theta} = -\frac{1}{2} \tag{5.47}$$

We can relate this to a derivative with respect to B via:

$$\frac{d\phi}{dB} = \frac{d\phi}{d\Theta}\frac{d\Theta}{dB} = -\frac{1}{2}\frac{g\mu_B}{\hbar}T_{rep} \tag{5.48}$$

Between RSA peaks as B is increased, ϕ decreases. Now we look at the derivative of the

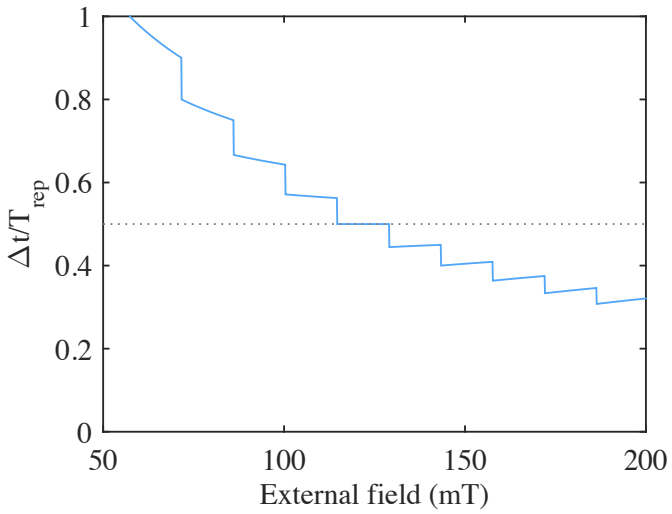

Figure 5.8: Delay time at which the 9$^{\text{th}}$ zero crossing occurs with infinite lifetime ($x = 0$). This figure shows the transition from monotonic behavior when $\Delta t > T_{rep}/2$ to non-invertable dependence below $\Delta t = T_{rep}/2$.

first term:

$$\frac{d}{dB}\Omega_L \Delta t = \Delta t \frac{d\Omega_L}{dB} = \frac{g\mu_B}{\hbar}\Delta t \tag{5.49}$$

Regardless of the delay time, this term increases with increasing external magnetic field. Adding these two terms together, in the case of infinite T_2^* and looking only between RSA peaks, we arrive at:

$$\frac{d}{dB}[\Omega_L \Delta t + \phi] = \frac{g\mu_B}{\hbar}\left(\Delta t - \frac{T_{rep}}{2}\right) \tag{5.50}$$

The delay time at which a zero crossing occurs will decrease with increasing magnetic field as long as this derivative is positive. When an RSA peak is crossed, ϕ increases rapidly with an increase in magnetic field. The limiting factor becomes ensuring that this derivative remains positive when ϕ is decreasing between resonance peaks. This condition is always satisfied in the case of infinite T_2^* as long as $\Delta t > T_{rep}/2$. As the lifetime is decreased, the corresponding minimum delay time for monotonic behavior decreases, and can be determined by finding the derivative of ϕ at its maximum negative value, which occurs at $\Theta = (2n+1)\pi/2$. However, the sensitivity of the measurement is always best when the zero crossing being followed is found at long time delays. This behavior is visible in Fig. 5.8, where the 9$^{\text{th}}$ zero

crossing delay time divided by the laser repetition time is plotted for a wide range of field values. Monotonic behavior disappears when the delay time drops below $T_{rep}/2$.

5.5 Pump-pump interactions

When the pump pulse arrives at the sample, optically generated majority carriers are created with a net spin polarization [15]. Minority carriers, in this case holes, are generated as well, but these holes dephase rapidly, as discussed in Chapter III. The dephasing of the holes leads to randomized recombination and photoemission, leaving only dopant electrons in the conduction band, which will have the same degree of polarization as the sum of the optically injected and dopant electrons before recombination. If the pump power is sufficient that the number of dopant and optically injected electrons in the conduction band after absorption of the pump pulse are comparable, then we must account for the loss of polarization of electrons from previous pump pulses when recombination occurs [91]. Here, we investigate this effect and discuss its implications on the above analysis.

When a pump pulse is incident on the sample, light is absorbed and optically generated carriers are created with densities n_O for both electrons and holes. In the materials used here, there are also dopant electrons present with density n_D, making the total majority carrier density $n_T = n_O + n_D$. Upon recombination, n_O carriers will recombine at random with optically generated holes and fall back to the valence band, emitting a photon. Accordingly, after recombination any spin polarization present before absorption is decreased by a factor ζ, given by:

$$\zeta = \frac{n_D}{n_O + n_D} \tag{5.51}$$

With this new factor added, the total spin phasor, originally found in 5.4, becomes:

$$\underline{\mathrm{s}}(\Delta t) = \sum_{n\geq 0} S_0 \zeta^n \exp\left[(i\Omega_L - 1/T_2^*)(\Delta t + nT_{rep})\right] \tag{5.52}$$

Repeating the above analysis, we find the following expressions for r and ϕ:

$$r = (1 - 2\zeta e^{-x}\cos\Theta + \zeta^2 e^{-2x})^{-\frac{1}{2}} \tag{5.53}$$

$$\phi = \tan^{-1}\left[\frac{\zeta e^{-x}\sin\Theta}{1 - \zeta e^{-x}\cos\Theta}\right] \tag{5.54}$$

Crucially, with these updated expressions for r and ϕ, the $\hat{z}$ component of the spin polarization will still precess at Ω_L and decay with lifetime T_2^*; that is, Eq. 5.8 still holds, and a fit to TRFR data will still report the correct values. However, measurements of the lifetime based on RSA or ϕ_{extr} will report an artificially low lifetime. The upshot of this is that by comparing the measured values of the lifetime found by TRFR and either resonance technique, it is possible to calculate the value of the factor ζ, and by extension the ratio of optically generated to dopant carriers in the system. The value of ζ increases to approach 1 as the number of optically injected carriers decreases. Accordingly, this effect can be suppressed by sufficiently lowering the total beam powers, as well as by tuning the laser to the maximum Faraday rotation wavelength on the low-energy side of the absorption edge.

In practice, this analysis is complicated by the fact that n_O is not uniform across the beam area, but instead will vary with the pump intensity distribution. Accordingly, the degree of spin polarization becomes positionally dependent, and the true signal must be calculated from integrals over this distribution. Additionally, accurate knowledge of the pump and probe beam profiles is required.

5.6 Effects of in-plane electron motion

In the preceding analysis, it was tacitly assumed that the motion of the electrons is negligible within the spin lifetime; that is, dephasing occurs more quickly than electrons leave the region of interrogation. Here, we investigate the implications to the above model in situations where this is not the case.

Motion of the electrons in our samples results from two primary mechanisms. When an

in-plane electric field is present, electrons will have a non-zero net drift velocity determined by:

$$\vec{v}_{\text{drift}} = \mu \vec{E} \tag{5.55}$$

where μ is the electron mobility in the sample. Even in the absence of an electric field, electrons will diffuse throughout the sample. Both of these mechanisms are described mathematically within the drift-diffusion equation, given by:

$$\frac{\partial c}{\partial t} = \nabla \cdot (D \nabla c) - \nabla \cdot (\vec{v}_{\text{drift}} c) + R \tag{5.56}$$

where c is the quantity of interest, D is the diffusion constant, and R a source term. We may assume here that D is spatially homogeneous and that the velocity field has zero divergence (corresponding to an incompressible flow), and that between pulses $R = 0$. Applying these simplifications, we arrive at:

$$\frac{\partial c}{\partial t} = D \nabla^2 c - \vec{v}_{\text{drift}} \cdot \nabla c \tag{5.57}$$

Here, we take c to represent the density of optically aligned spins in the conduction band. To proceed, I will make the simplifying assumption that the effective magnetic field seen by the electrons due to their diffusive velocity is small compared to the effective field due to their drift velocity and the externally applied magnetic field, and neglect it. The practical effect of this is that we can assume that the spin vector for the optically aligned electrons is uniform in space. Situations where this contribution cannot be neglected require use of the full spinor form of the semiclassical Boltzmann transport equation, and are discussed in detail in for example, references [92] and [93].

First, we consider diffusion in the absence of a net drift velocity. In this case, the partial differential equation governing the system dynamics is given by:

$$\frac{\partial c}{\partial t} = D \nabla^2 c \tag{5.58}$$

This can be solve using a Green's function method. The Green's function, whose derivation is shown in detail in Ref. [94], is found to be:

$$g(x|\xi,t) = \frac{1}{\sqrt{4\pi Dt}} \exp\left[\frac{-(x-\xi)^2}{4Dt}\right] \tag{5.59}$$

Convolving this Green's function with a Gaussian distribution of width σ at the origin, corresponding to the initial condition:

$$c(\vec{r}, t=0) = \frac{1}{\sqrt{2\pi\sigma_0^2}} \exp\left[\frac{-r^2}{2\sigma_0^2}\right] \tag{5.60}$$

the solution is found to be:

$$c(\vec{r}, t) = \frac{1}{\sqrt{2\pi(\sigma_0^2 + 2Dt)}} \exp\left[\frac{r^2}{2\sigma_0^2 + 4Dt}\right] \tag{5.61}$$

This corresponds to a Gaussian in $\vec{r}$ whose width is given by:

$$\sigma(t) = \sqrt{\sigma_0^2 + 2Dt} \tag{5.62}$$

The electron diffusion constant D here can be estimated using the Einstein-Smolouchowski relation[95, 96], $D = \mu k_B T/q$. Spin-drag measurements suggest a mobility of approximately 5500 $cm^2V^{-1}s^{-1}$[17] in our samples, which results in $D = 3.45 \times 10^{-2}$ $\mu m^2 ns^{-1}K^{-1}$. Figure 5.9 contains a plot of the beam FWHM as a function of elapsed time for a range of temperatures and assuming an initial FWHM of 30 μm. As the temperature increases, so too does the rate of expansion of the spot due to diffusion. At the same time, however, T_2^* decreases. At 10 K in the sample used in the collection of experimental data here, over the spin lifetime of 10 ns, the FWHM of the spin envelope function has increased by only a few percent. Despite the faster expansion due to diffusion, at higher temperatures the decreasing spin lifetime means that diffusion continues to be a small effect.

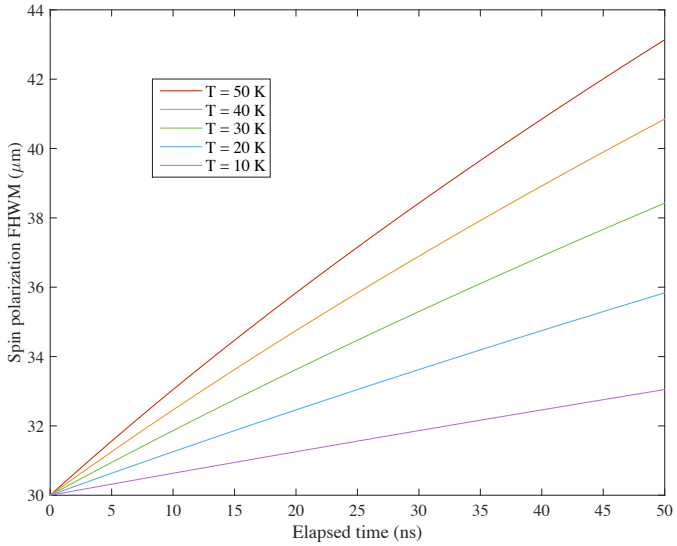

Figure 5.9: Electron spin packet FWHM size as a function of elapsed time for a range of temperatures assuming a constant mobility of 5500 $cm^2V^{-1}s^{-1}$ and FHWM of 30 μm at $t = 0$.

With diffusion having been accounted for, we now turn to the effect of a non-zero drift velocity, which gives rise to the second term on the right-hand side of Eq. 5.57. The simplest way to deal with this is to use the solution in the rest frame above and perform a Galilean transform, under which Eq. 5.57 is invariant, into the lab frame. Accordingly, the full solution may be written as:

$$c(\vec{r},t) = \frac{1}{\sqrt{2\pi(\sigma_0^2 + 2Dt)}} \exp\left[\frac{|\vec{r} - \vec{v}_{\text{drift}}t|^2}{2\sigma_0^2 + 4Dt}\right] \tag{5.63}$$

In the context of our experiments, this solution can be interpreted as a spatial envelope function for the spin polarization due to a particular pump pulse occurring at $t = 0$. As we have seen, the Faraday rotation of the probe beam is proportional to the out-of-plane component of the spin polarization within the sample. When the spin polarization is spatially dependent, the constant of proportionality (denoted here as F) will be determined by an integral over space of the product of the spin polarization and probe beam intensity profile:

$$F \propto \int dA\ I_{probe}(\vec{r}) s_{\hat{z}}(\vec{r},t) \tag{5.64}$$

When the spins are moving in the plane, $s_{\hat{z}}$ becomes a function of both position and time. Accordingly, F will vary from pulse to pulse and be a function of Δt as well, denoted by $F \to F_n(\Delta t)$. With this factor, the equation for the total spin phasor (Eq. 5.4) becomes:

$$\begin{aligned}\underline{\mathrm{s}}(\Delta t) &= \sum_{n\geq 0} S_0 F_n(\Delta t) \exp\left[(i\Omega_L - 1/T_2^*)(\Delta t + nT_{rep})\right] \\ &= S_0 \exp\left[(i\Omega_L - 1/T_2^*)\Delta t\right] \sum_{n\geq 0} F_n(\Delta t) \exp\left[(i\Omega_L - 1/T_2^*)nT_{\mathrm{rep}}\right] \end{aligned} \tag{5.65}$$

The presence of $F_n(\Delta t)$ within the sum means that we can no longer treat the sum as a constant as we did above. Accordingly, $\underline{\mathrm{s}}$ no longer precesses at Ω_L nor decays with characteristic time T_2^*. Its behavior now depends on many more variables, including the pump and probe beam profiles and relative positioning, the presence of an in-plane electric field, electron mobility, and so on. Care must be taken in these situations to account for all of these effects.

CHAPTER VI

Conclusion

This dissertation has focused on elucidating aspects of electron spin transport in GaAs and InGaAs. In particular, we have shown current-direction dependent dynamic nuclear polarization which results from current-induced electron spin polarization for the first time. The polarization timescale and saturated nuclear magnetic field were investigated throughout parameter space. An asymmetry in the saturation nuclear magnetic field between currents flowing in opposite directions was found and explained as resulting from DNP generated by other current-dependent mechanisms which do not depend on the direction of current but only its magnitude. An unexpected difference between the change in nuclear magnetic field for polarizing and depolarizing transitions was found, and ultimately determined to result from a previously uncharacterized phase effect in time-resolved Faraday rotation measurements that results from spins polarized by previous pulses. New closed-form expressions for the total Faraday rotation when the spin lifetime is on the order of, or greater than the laser repetition time are derived which include an analytic expression for the phase shift. These expressions are used to explore the phase shift throughout parameter space. A new measurement of spin lifetime which takes advantage of the phase shift was proposed. Finally, future measurements of DNP which will help to confirm some of the conclusions drawn within this dissertation and further explore the process of DNP resulting from CISP are suggested.

APPENDIX

APPENDIX A

Thorlabs 3-axis Stage Hardware and Software

Due to the inhomogeneous nature of the electric field and/or strain parameters in some of our samples, accurately positioning the pump and probe beams on the sample is necessary. This can be done manually in cases where the sample geometry and orientation allow, but this becomes difficult to do by eye for complicated samples and awkward orientations. In these situations, a systematic way to position both the pump and probe beams on the sample is required. Automated positioning also opens up the possibility of doing accurate spatially-dependent scans across a sample.

Two pieces of equipment allow us to steer the pump and probe beam positions on the sample independently. The pump beam position can be moved relative to the probe beam position by way of a motorized steering mirror. Because we intend to collect the reflected or transmitted light from the probe beam, steering it with a single mirror is not an option, as displacing the probe beam on the sample would corrupt the collection-path alignment. Instead, we leave the probe beam fixed in space and move the sample relative to it. The small size of the cold finger in the Janis ST-300 cryostat means we cannot fit a translation stage within the cryostat. Accordingly, we move the whole cryostat by way of heavy duty motorized stages which are capable of driving the approximately 8 kg load consisting of the cryostat and transfer line.

The 3-axis positioning system used here is based on Thorlabs TravelMax 2 inch linear

translation stages (part number LNR50S). These stages have a maximum load of 30 kg for horizontal motion and 10 kg for vertical motion, and a bidirectional positional repeatibility of 0.05 μm. The translation stage motion is generated via stepper motors which are driven by the Thorlabs BSC-203 3-axis stepper motor driver. While LabVIEW virtual instruments are included for interfacing with the stepper motor controller (hereafter referred to as BSC-203), communication with Matlab must occur through the Microsoft ActiveX software framework.

In this appendix, details of the Matlab control software written to ease interfacing with the BSC-203 Stepper Motor Controller are included. The augmenting circuits which implement external contact limit switches which protect the cryostat against inadvertently crashing into the electromagnet poles are described, along with the implementation of an external jog controller using a legacy Nintendo® gaming controller and PICAXE® microcontroller.

A.1 Matlab interfacing software

The Matlab code written to interface with the BSC-203 is based on object-oriented programming principles. System parameters, such as acceleration and maximum velocity, board serial numbers, etc., as well as methods which correspond to particular commands, are defined within the axis3eng classdef file. When this class is instantiated, a communications channel to the BSC-203 is opened through ActiveX, default parameters are set, and a GUI is generated with real-time readouts of the stage position and access to manually input commands and change system settings. This can all be done programatically as well, allowing for the scripting of experiments which make full use of the translation stage's capabilities.

A.2 External hardware limiting switch

In any motion control system, it is good practice to put safeguards into place which ensure inadvertent commands cannot cause damage to the system. To that end, the TravelMax stages contain two internal limit switches which prevent damage to the drive mechanism.

In an open-loop system such as this, a limit switch can also be used to generate a position calibrating data point; when the switch is activated, the stage position is known. While the internal limit switches work well for two axes in our setup, lateral motion between the electromagnet poles is constricted in a way that isn't accounted for. In this section, an augmenting circuit is described which acts as external limiting switches operating in conjunction with the internal limit switches, preventing damage to the cryostat and allowing calibration of the cryostat position in that direction.

As is generally the case, the limit switch input pins on the BSC-203 are active-low with 10 kΩ pull-up resistors. Accordingly, the internal limit switches are normally-closed, and when closed connect the limit switch pin to ground. This arrangement is chosen because faults present most frequently as an open circuit, which in this case prevents motion commands from being issued until the limit switches are functioning correctly. Unfortunately, the BSC-203 has no inputs for external limit switches. To overcome this, any external limit switches must make use of the pre-existing inputs. Since the signal is active-low, external limit switches must also be normally closed and in series with the internal limit switch.

To implement the external limit switch, electrically isolated contacts are first placed on the ends of the electromagnet poles. It is critical that these contacts do not interfere with the magnetic field. A metal with a small susceptibility must therefore be used. Copper, which is weakly diamagnetic with a volume magnetic susceptibility $\chi_V = -1.0 \times 10^{-6}$, was chosen for this purpose. The copper contact is electrically isolated from the electromagnet and is held high with a 10 kΩ pull-up resistor. When the cryostat, which is electrically grounded, makes contact with the copper, the voltage on it is pulled to ground. This active-low signal on the copper contact is then used as the input to the base of a 2N3904 NPN bipolar junction transistor. The collector of this transistor is connected to the limit switch input and the emitter is connected to the internal limit switch. When the voltage on the copper contact drops to zero, the conduction pathway between the collector and emitter in the transistor is broken, the limit switch input goes high, and the BSC-203 interprets this as an activated

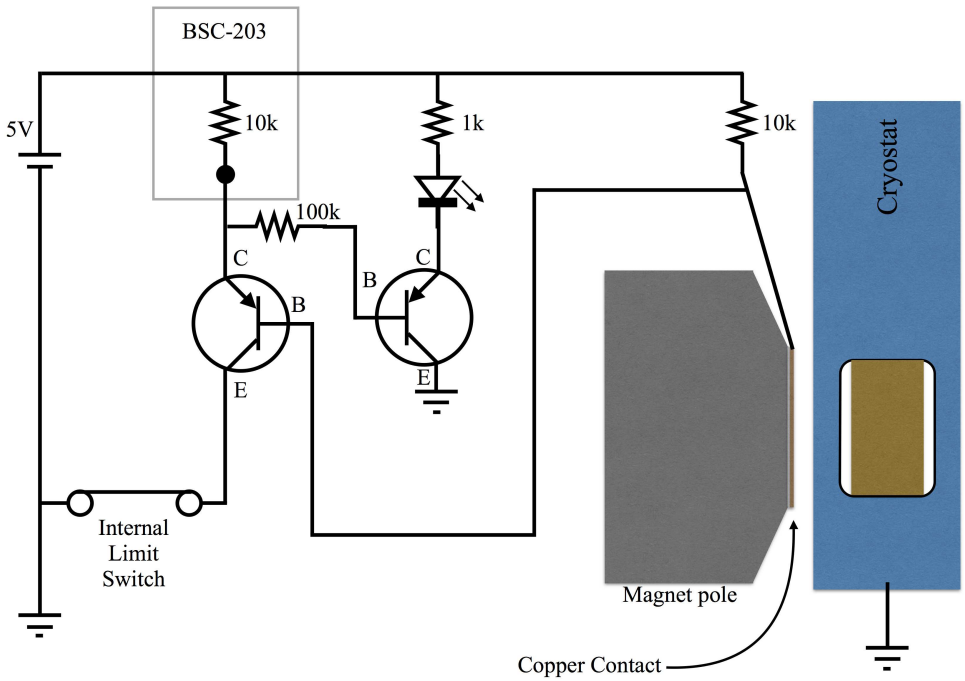

Figure A.1: Circuit diagram for one side of the external limit switch system designed to protect the cryostat against inadvertent collision with the electromagnet poles.

limit switch.

Two of these circuits are implemented, which limit the stage motion in both directions. Additionally, the circuit includes LEDs which light when a limit switch has been hit, alerting the user when the stage is being positioned manually. The circuit diagram for one side of this circuit is shown in Figure A.1.

A.3 External jog controller

In addition to accepting positional commands from the computer interface, the BSC-203 controller can also receive jog commands via a proprietary serial joystick, or low-level TTL inputs. In this section, I describe an implementation which allows a Nintendo Entertainment System controller (hereafter referred to as a Nintendo controller) to be interfaced to the TTL inputs for issuing jog commands directly from the optics bench.

Each of the 3 channels on the motion controller includes a 15-pin control port which allows low-level access to important I/O signals. Among these are inputs for clockwise and

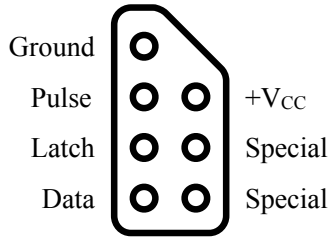

Figure A.2: Pinout for Nintendo Entertainment System controller used to implement the manual jog controller.

counter-clockwise jog commands. As with all signaling on the BSC-203, these inputs are based on 5-volt TTL signals and are active-low with 10 kΩ internal pull-up resistors. When these pins are driven low the controller drives the channel's stepper motor in the correct direction. Software settings allow for customization of how the jog signals are interpreted. Separate settings for jog motion acceleration and maximum velocity, and whether the jog occurs continuously while the signal is driven low or in discrete steps.

The Nintendo controller used in this circuit uses a serial transmission protocol to transmit the button state. This allows the button state to be transmitted over 3 wires, including in situations where more than one button is pressed at once. The controller pinout is shown in A.2. The serial protocol used by the Nintendo controller works as follows. At time $t = 0$, the console drives the latch pin on the controller high. This logs the current state of all the buttons, and the controller sets the data pin according to the state of the "A" button. This signal is active-low, so if the button is pressed the data pin is driven low. After 20 μs, the clock pin is driven with 8 square wave pulses with a pulse time of $10\mu s$ and 50% duty cycle. Each clock pulse instructs the controller to assert the data pin according to the state of the corresponding button when the latch pulse arrives. This sequence is repeated at a frequency of 100 Hz. Figure A.3 shows a timing diagram which describes this process.

The job of the PICAXE microcontroller in this circuit is to implement this serial trans-

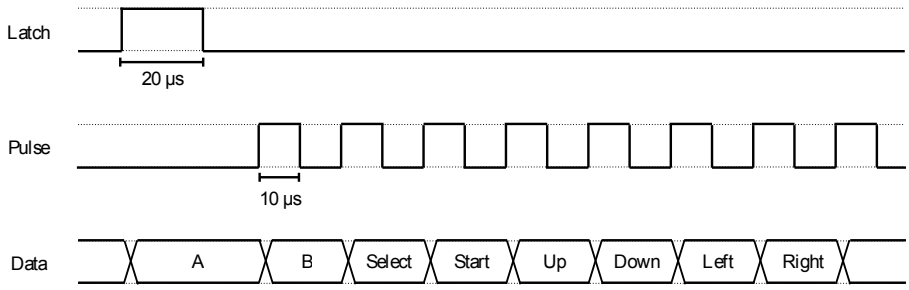

Figure A.3: Nintendo controller serial transmission protocol timing diagram.

mission protocol, and drive the jog inputs on the motion controller according to the button state of the nintendo controller. The D-pad (arrowed) buttons drive the axes corresponding to motion in the sample plane, and the A and B buttons jog the stage along the direction of laser propagation, adjusting the focus. The circuit diagram is shown in Fig. A.4. In addition to the components appearing on this circuit diagram, LEDs were added indicating power and the button state for the 6 buttons used in this implementation. They have been omitted for clarity.

The PICAXE 18M2+ microcontroller used here is based on the PIC microcontroller architecture with a serial bootloader preprogrammed into the program memory. This bootloader allows the microcontroller to be programmed from any device with a serial interface. A simple IDE is available from `www.picaxe.com`, which includes simulation capabilities and a compiler which allows programs written in BASIC to be uploaded on to the PICAXE chip.

The BASIC program used to perform the task of implementing the Nintendo controller serial protocol and driving the jog inputs accordingly is reproduced below. When the pro-

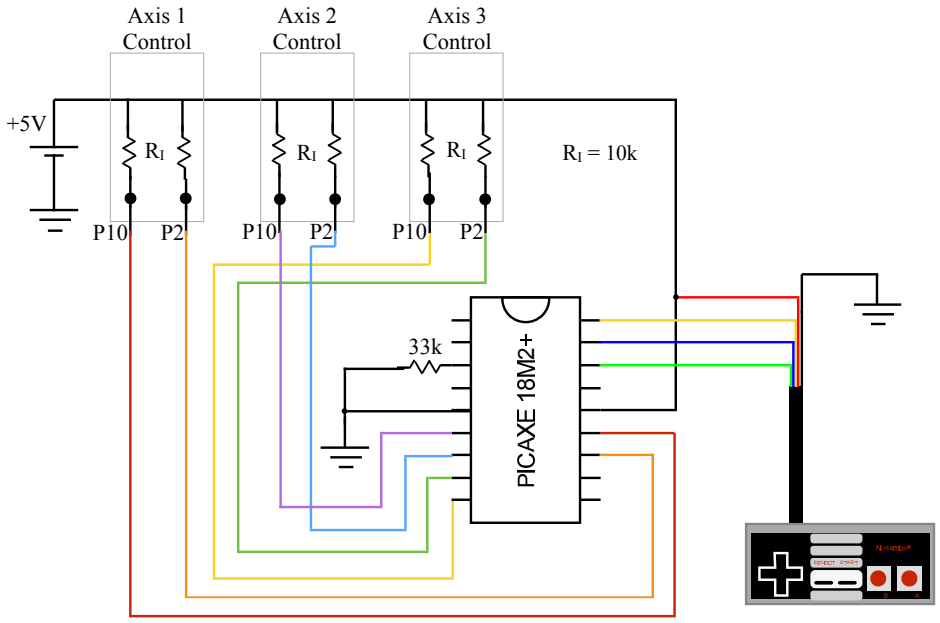

Figure A.4: Circuit diagram showing connections between the BSC-203 motion controller, PICAXE microprocessor, and Nintendo controller.

gram is first executed, the code contained in the `init` section is executed, and then the microcontroller enters the `main` infinite loop. Controller button state data is outputted to the output B pins, as described in the PICAXE data sheet. The pinout on the picaxe is contained in Table A.1.

```
symbol latch = C.1 ;pin 18
symbol pulse = C.0 ;pin 17
symbol datap = pinC.7 ;pin 16
symbol buttonstate = b0

init:
     setfreq m4  ;core freq = 4MHz, actual pause = 10*arg(pauseus)
     dirsb = %11111111
main:
     let buttonstate = %00000000
     high latch
     pauseus 2 ;Actually 20us
     low latch
     bit0 = datap
     buttonstate = buttonstate * 2
     for b1 = 0 to 5
          high pulse
          pauseus 1 ;Acutally 10us
          low pulse
          pauseus 1
          bit0 = datap
          buttonstate = buttonstate * 2
          next
     high pulse
     pauseus 1 ;
     low pulse
     pauseus 1
     bit0 = datap
     let pinsB = buttonstate
     pauseus 84 ;Actually 840, so loops each ~1ms
     goto main
```

Signal	Pin	Pin	Signal
–	Pin 1	Pin 18	Controller latch
–	Pin 2	Pin 17	Controller pulse
Serial Rx	Pin 3	Pin 16	Controller data
–	Pin 4	Pin 15	–
Ground	Pin 5	Pin 14	+5V
Right out	Pin 6	Pin 13	A out
Left out	Pin 7	Pin 12	B out
Down out	Pin 8	Pin 11	Select out
Up out	Pin 9	Pin 10	Start out

Table A.1: PICAXE 18M2+ pinout for Nintendo controller jog circuit.

BIBLIOGRAPHY

BIBLIOGRAPHY

[1] S. A. Wolf, D. D. Awschalom, R. A. Buhrman, J. M. Daughton, S. Von Molnar, M. L. Roukes, A. Yu Chtchelkanova, and D. M. Treger. Spintronics: a spin-based electronics vision for the future. Science, 294(5546):1488–1495, 2001.

[2] Gary A. Prinz. Spin-polarized transport. Physics Today, 48, 1995.

[3] G. Binasch, P. Grünberg, F. Saurenbach, and W. Zinn. Enhanced magnetoresistance in layered magnetic structures with antiferromagnetic interlayer exchange. Phys. Rev. B, 39:4828–4830, Mar 1989. doi: 10.1103/PhysRevB.39.4828. URL http://link.aps.org/doi/10.1103/PhysRevB.39.4828.

[4] M. N. Baibich, J. M. Broto, A. Fert, F. Nguyen Van Dau, F. Petroff, P. Etienne, G. Creuzet, A. Friederich, and J. Chazelas. Giant magnetoresistance of (001)fe/(001)cr magnetic superlattices. Phys. Rev. Lett., 61:2472–2475, Nov 1988. doi: 10.1103/PhysRevLett.61.2472. URL http://link.aps.org/doi/10.1103/PhysRevLett.61.2472.

[5] Supriyo Datta and Biswajit Das. Electronic analog of the electrooptic modulator. Applied Physics Letters, 56(7):665–667, 1990. doi: http://dx.doi.org/10.1063/1.102730. URL http://scitation.aip.org/content/aip/journal/apl/56/7/10.1063/1.102730.

[6] Pojen Chuang, Sheng-Chin Ho, LW Smith, F Sfigakis, M Pepper, Chin-Hung Chen, Ju-Chun Fan, JP Griffiths, I Farrer, HE Beere, et al. All-electric all-semiconductor spin field-effect transistors. Nature nanotechnology, 10(1):35–39, 2015.

[7] Charles Kittel. Introduction to Solid State Physics. John Wiley and Sons, Inc., 7th edition, 1996.

[8] B. M. Norman, C. J. Trowbridge, D. D. Awschalom, and V. Sih. Current-induced spin polarization in anisotropic spin-orbit fields. Phys. Rev. Lett., 112:056601, Feb 2014. doi: 10.1103/PhysRevLett.112.056601. URL http://link.aps.org/doi/10.1103/PhysRevLett.112.056601.

[9] P. Yu and M. Cardona. Fundamentals of Semiconductors. Springer-Verlag, 4th edition, 2010.

[10] I. Vurgaftman, J. R. Meyer, and L. R. Ram-Mohan. Band parameters for iiiv compound semiconductors and their alloys. Journal of Applied Physics, 89(11):5815–5875, 2001. doi: http://dx.doi.org/10.1063/1.1368156. URL http://scitation.aip.org/content/aip/journal/jap/89/11/10.1063/1.1368156.

[11] J. D. Jackson. Classical Electrodynamics. John Wiley and Sons, Inc., 3rd edition, 1999.

[12] J. J. Sakurai. Modern Quantum Mechanics. Addison-Wesley, 1994.

[13] G. Dresselhaus. Spin-orbit coupling effects in zinc blende structures. Phys. Rev., 100:580–586, Oct 1955. doi: 10.1103/PhysRev.100.580. URL http://link.aps.org/doi/10.1103/PhysRev.100.580.

[14] Yu. A. Bychkov and E. I. Rashba. Oscillatory effects and the magnetic susceptibility of carriers in inversion layers. Journal of Physics C: Solid State Physics, 17(33):6039, 1984. URL http://stacks.iop.org/0022-3719/17/i=33/a=015.

[15] Edited by F. Meier and B. P. Zakharchenya. Optical Orientation. Elsevier, 1984.

[16] G. C. La Rocca, Nammee Kim, and S. Rodriguez. Effect of uniaxial stress on the electron spin resonance in zinc-blende semiconductors. Phys. Rev. B, 38:7595–7601, Oct 1988. doi: 10.1103/PhysRevB.38.7595. URL http://link.aps.org/doi/10.1103/PhysRevB.38.7595.

[17] Benjamin M. Norman. Electrical generation of spin polarization in strained III-V semiconductors. PhD thesis, University of Michigan, 2014.

[18] Eugen Merzbacher. Quantum Mechanics. John Wiley & Sons, Inc., third edition, 1998.

[19] Jay A. Gupta. Coherence and Manipulation of Spin States in Semiconductor Nanostructures. PhD thesis, University of California Santa Barbara, 2002.

[20] K.A. Olive et al. Review of Particle Physics. Chin.Phys., C38:090001, 2014. doi: 10.1088/1674-1137/38/9/090001.

[21] R. R. Parsons. Band-to-band optical pumping in solids and polarized photoluminescence. Phys. Rev. Lett., 23:1152–1154, Nov 1969. doi: 10.1103/PhysRevLett.23.1152. URL http://link.aps.org/doi/10.1103/PhysRevLett.23.1152.

[22] A. I. Ekimov and V. I. Safarov. Optical orientation of carriers in interband transitions in semiconductors. J. Exp. Theor. Phys. Lett., 12, 1970.

[23] Wilhelm Hanle. Über magnetische beeinflussung der polarisation der resonanzfluoreszenz. Zeitschrift fr Physik, 30(1):93–105, 1924. ISSN 0044-3328. doi: 10.1007/BF01331827. URL http://dx.doi.org/10.1007/BF01331827.

[24] Ole Knudsen. The faraday effect and physical theory, 18451873. Archive for History of Exact Sciences, 15(3):235–281, 1976. ISSN 0003-9519. doi: 10.1007/BF00412258. URL http://dx.doi.org/10.1007/BF00412258.

[25] Franz Urbach. The long-wavelength edge of photographic sensitivity and of the electronic absorption of solids. Phys. Rev., 92:1324–1324, Dec 1953. doi: 10.1103/PhysRev.92.1324. URL http://link.aps.org/doi/10.1103/PhysRev.92.1324.

[26] A. Abragram. The Principles of Nuclear Magnetism. Oxford University Press, 1961.

[27] Charles P. Slichter. Principles of Magnetic Resonance. Springer-Verlag, 3rd edition, 1978.

[28] Yuichiro K. Kato. Electrical Manipulation of Electron Spin Coherence in Nonmagnetic Semiconductors. PhD thesis, University of California Santa Barbara, 2005.

[29] M. I. D'yakonov and V. I. Perel. Spin relaxation of conduction electrons in noncentrosymmetric semiconductros. Sov. Phys. Solid State, 13:3023–3026, 1971.

[30] J. Fabian and S. Das Sarma. Spin relaxation of conduction electrons. Journal of Vacuum Science & Technology B, 17(4): 1708–1715, 1999. doi: http://dx.doi.org/10.1116/1.590813. URL http://scitation.aip.org/content/avs/journal/jvstb/17/4/10.1116/1.590813.

[31] R. J. Elliott. Theory of the effect of spin-orbit coupling on magnetic resonance in some semiconductors. Phys. Rev., 96:266–279, Oct 1954. doi: 10.1103/PhysRev.96.266. URL http://link.aps.org/doi/10.1103/PhysRev.96.266.

[32] Y. Yafet. g factors and spin-lattice relaxation of conduction electrons*. volume 14 of Solid State Physics, pages 1 – 98. Academic Press, 1963. doi: http://dx.doi.org/10.1016/S0081-1947(08)60259-3. URL http://www.sciencedirect.com/science/article/pii/S0081194708602593.

[33] Y. K. Kato, R. C. Myers, A. C. Gossard, and D. D. Awschalom. Current-induced spin polarization in strained semiconductors. Phys. Rev. Lett., 93:176601, Oct 2004. doi: 10.1103/PhysRevLett.93.176601. URL http://link.aps.org/doi/10.1103/PhysRevLett.93.176601.

[34] N. P. Stern, S. Ghosh, G. Xiang, M. Zhu, N. Samarth, and D. D. Awschalom. Current-induced polarization and the spin hall effect at room temperature. Phys. Rev. Lett., 97:126603, Sep 2006. doi: 10.1103/PhysRevLett.97.126603. URL http://link.aps.org/doi/10.1103/PhysRevLett.97.126603.

[35] W. F. Koehl, M. H. Wong, C. Poblenz, B. Swenson, U. K. Mishra, J. S. Speck, and D. D. Awschalom. Current-induced spin polarization in gallium nitride. Applied Physics Letters, 95(7):072110, 2009. doi: http://dx.doi.org/10.1063/1.3194781. URL http://scitation.aip.org/content/aip/journal/apl/95/7/10.1063/1.3194781.

[36] V. Sih, R. C. Myers, Y. K. Kato, W. H. Lau, A. C. Gossard, and D. D. Awschalom. Spatial imaging of the spin hall effect and current-induced polarization in two-dimensional electron gases. Nature Physics, 1(1):31–35, 2005.

[37] A. G. Aronov, Yu. B. Lyanda-Geller, and G. E. Pikus. Spin polarization of electrons by an electric current. J. Exp. Theor. Phys., 73, 1991.

[38] Hans-Andreas Engel, Emmanuel I. Rashba, and Bertrand I. Halperin. Out-of-plane spin polarization from in-plane electric and magnetic fields. Phys. Rev. Lett., 98:036602, Jan 2007. doi: 10.1103/PhysRevLett.98.036602. URL http://link.aps.org/doi/10.1103/PhysRevLett.98.036602.

[39] Hiromasa Shimizu, Syunsuke Goto, and Toshiaki Mori. Optical isolation using nonreciprocal polarization rotation in feingaalas/inp semiconductor active waveguide optical isolators. Applied Physics Express, 3(7):072201, 2010. URL http://stacks.iop.org/1882-0786/3/i=7/a=072201.

[40] Xiaoyun Guo, Tauhid Zaman, and Rajeev J. Ram. Magneto-optical semiconductor waveguides for integrated isolators. Proc. SPIE, 5729:152–159, 2005. doi: 10.1117/12.589332. URL http://dx.doi.org/10.1117/12.589332.

[41] T. R. Zaman, Xiaoyun Guo, and R. J. Ram. Semiconductor waveguide isolators. Lightwave Technology, Journal of, 26(2):291–301, Jan 2008. ISSN 0733-8724. doi: 10.1109/JLT.2007.909859.

[42] N. Sugimoto, T. Shintaku, A. Tate, H. Terui, M. Shimokozono, E. Kubota, M. Ishii, and Y. Inoue. Waveguide polarization-independent optical circulator. Photonics Technology Letters, IEEE, 11(3):355–357, March 1999. ISSN 1041-1135. doi: 10.1109/68.748233.

[43] T. R. Zaman, X. Guo, and R. J. Ram. Faraday rotation in an inp waveguide. Applied Physics Letters, 90(2):023514, 2007. doi: http://dx.doi.org/10.1063/1.2430931. URL http://scitation.aip.org/content/aip/journal/apl/90/2/10.1063/1.2430931.

[44] Vadym Zayets, Mukul C. Debnath, and Koji Ando. Optical isolation in $cd_{1-x}mn_xte$ magneto-optical waveguide grown on gaas substrate. J. Opt. Soc. Am. B, 22(1):281–285, Jan 2005. doi: 10.1364/JOSAB.22.000281. URL http://josab.osa.org/abstract.cfm?URI=josab-22-1-281.

[45] T. R. Zaman, X. Guo, and R. J. Ram. Proposal for a polarization-independent integrated optical circulator. Photonics Technology Letters, IEEE, 18(12):1359–1361, June 2006. ISSN 1041-1135. doi: 10.1109/LPT.2006.877336.

[46] J. Fujita, M. Levy, R. M. Osgood, L. Wilkens, and H. Dtsch. Waveguide optical isolator based on machzehnder interferometer. Applied Physics Letters, 76(16):2158–2160, 2000. doi: http://dx.doi.org/10.1063/1.126284. URL http://scitation.aip.org/content/aip/journal/apl/76/16/10.1063/1.126284.

[47] Christopher J. Trowbridge, Benjamin M. Norman, Jason Stephens, Arthur C. Gossard, David D. Awschalom, and Vanessa Sih. Electron spin polarization-based integrated photonic devices. Opt. Express, 19(16):14845–14851, Aug 2011. doi: 10.1364/OE.19.014845. URL http://www.opticsexpress.org/abstract.cfm?URI=oe-19-16-14845.

[48] R. Giri, S. Cronenberger, M. Vladimirova, D. Scalbert, K. V. Kavokin, M. M. Glazov, M. Nawrocki, A. Lemaitre, and J. Bloch. Giant photoinduced faraday rotation due to the spin-polarized electron gas in an n-gaas microcavity. Phys. Rev. B, 85:195313, May 2012. doi: 10.1103/PhysRevB.85.195313. URL http://link.aps.org/doi/10.1103/PhysRevB.85.195313.

[49] Timothy W. Saucer, Caleb Zerger, Brennan Pursley, and Vanessa Sih. Amplifying optical rotation using a coupled waveguide and ring resonator. Opt. Express, 23(5):6050–6057, Mar 2015. doi: 10.1364/OE.23.006050. URL http://www.opticsexpress.org/abstract.cfm?URI=oe-23-5-6050.

[50] A. Yariv. Coupled-mode theory for guided-wave optics. Quantum Electronics, IEEE Journal of, 9(9):919–933, Sep 1973. ISSN 0018-9197. doi: 10.1109/JQE.1973.1077767.

[51] M. M. Glazov and E. L. Ivchenko. Resonant spin amplification in nanostructures with anisotropic spin relaxation and spread of the electronic g factor. Semiconductors, 42(8):951–957, 2008. ISSN 1063-7826. doi: 10.1134/S1063782608080137. URL http://dx.doi.org/10.1134/S1063782608080137.

[52] J. M. Kikkawa and D. D. Awschalom. Resonant spin amplification in n-type gaas. Phys. Rev. Lett., 80(19).

[53] I. A. Yugova, M. M. Glazov, D. R. Yakovlev, A. A. Sokolova, and M. Bayer. Coherent spin dynamics of electrons and holes in semiconductor quantum wells and quantum dots under periodical optical excitation: Resonant spin amplification versus spin mode locking. Phys. Rev. B, 85:125304, Mar 2012. doi: 10.1103/PhysRevB.85.125304. URL http://link.aps.org/doi/10.1103/PhysRevB.85.125304.

[54] W. D. Knight. Nuclear magnetic resonance shift in metals. Phys. Rev., 76:1259–1260, Oct 1949. doi: 10.1103/PhysRev.76.1259.2. URL http://link.aps.org/doi/10.1103/PhysRev.76.1259.2.

[55] Albert W. Overhauser. Polarization of nuclei in metals. Phys. Rev., 92:411–415, Oct 1953. doi: 10.1103/PhysRev.92.411. URL http://link.aps.org/doi/10.1103/PhysRev.92.411.

[56] T. R. Carver and C. P. Slichter. Polarization of nuclear spins in metals. Phys. Rev., 92:212–213, Oct 1953. doi: 10.1103/PhysRev.92.212.2. URL http://link.aps.org/doi/10.1103/PhysRev.92.212.2.

[57] Georges Lampel. Nuclear dynamic polarization by optical electronic saturation and optical pumping in semiconductors. Phys. Rev. Lett., 20:491–493, Mar 1968. doi: 10.1103/PhysRevLett.20.491. URL http://link.aps.org/doi/10.1103/PhysRevLett.20.491.

[58] B. I. Zakharchenya, V. G. Fleisher, R. I. Dzhioev, Yu. P. Veshchunov, and I. B. Rusanov. Effect of optical orientation of electron spins in a gaas crystal. J. Exp. Theor. Phys. Lett., 13, 1971.

[59] A. I. Ekimov and V. I Saforov. Optical electron-nuclear resonance in semiconductors. J. Exp. Theor. Phys. Lett., 15, 1972.

[60] V. L. Berkovits, A. I. Ekimov, and V. I. Safarov. Optical orientation in a system of electrons and lattice nuclei in semiconductors. experiment. J. Exp. Theor. Phys., 38, 1974.

[61] M. I. D'yakonov and V. I. Perel'. Optical orientation in a system of electrons and lattice nuclei in semiconductors. theory. J. Exp. Theor. Phys., 38, 1974.

[62] D. Paget, G. Lampel, B. Sapoval, and V. I. Safarov. Low field electron-nuclear spin coupling in gallium arsenide under optical pumping conditions. Phys. Rev. B, 15:5780–5796, Jun 1977. doi: 10.1103/PhysRevB.15.5780. URL http://link.aps.org/doi/10.1103/PhysRevB.15.5780.

[63] J. M. Kikkawa and D. D. Awschalom. All-optical magnetic resonance in semiconductors. Science, 287(5452):473–476, 2000. doi: 10.1126/science.287.5452.473. URL http://www.sciencemag.org/content/287/5452/473.abstract.

[64] D. R. McCamey, J. van Tol, G. W. Morley, and C. Boehme. Fast nuclear spin hyperpolarization of phosphorus in silicon. Phys. Rev. Lett., 102:027601, Jan 2009. doi: 10.1103/PhysRevLett.102.027601. URL http://link.aps.org/doi/10.1103/PhysRevLett.102.027601.

[65] R. K. Kawakami, Y. Kato, M. Hanson, I. Malajovich, J. M. Stephens, E. Johnston-Halperin, G. Salis, A. C. Gossard, and D. D. Awschalom. Ferromagnetic imprinting of nuclear spins in semiconductors. Science, 294(5540):131–134, 2001. doi: 10.1126/science.1063186. URL http://www.sciencemag.org/content/294/5540/131.abstract.

[66] R. J. Epstein, F. M. Mendoza, Y. K. Kato, and D. D. Awschalom. Anisotropic interactions of a single spin and dark-spin spectroscopy in diamond. Nature physics, 1(2): 94–98, 2005.

[67] J. Strand, B. D. Schultz, A. F. Isakovic, C. J. Palmstrøm, and P. A. Crowell. Dynamic nuclear polarization by electrical spin injection in ferromagnet-semiconductor heterostructures. Phys. Rev. Lett., 91:036602, Jul 2003. doi: 10.1103/PhysRevLett.91.036602. URL http://link.aps.org/doi/10.1103/PhysRevLett.91.036602.

[68] K. Hashimoto, K. Muraki, T. Saku, and Y. Hirayama. Electrically controlled nuclear spin polarization and relaxation by quantum-hall states. Phys. Rev. Lett., 88:176601, Apr 2002. doi: 10.1103/PhysRevLett.88.176601. URL http://link.aps.org/doi/10.1103/PhysRevLett.88.176601.

[69] Y. Q. Li, V. Umansky, K. von Klitzing, and J. H. Smet. Current-induced nuclear spin depolarization at landau level filling factor $\nu = 1/2$. Phys. Rev. B, 86:115421, Sep 2012. doi: 10.1103/PhysRevB.86.115421. URL http://link.aps.org/doi/10.1103/PhysRevB.86.115421.

[70] Jeffrey A. Reimer. Nuclear hyperpolarization in solids and the prospects for nuclear spintronics. Solid State Nuclear Magnetic Resonance, 37(12):3 – 12, 2010. ISSN 0926-2040. doi: http://dx.doi.org/10.1016/j.ssnmr.2010.04.001. URL http://www.sciencedirect.com/science/article/pii/S0926204010000081.

[71] Xiaodong Xu, Wang Yao, Bo Sun, Duncan G Steel, Allan S Bracker, Daniel Gammon, and LJ Sham. Optically controlled locking of the nuclear field via coherent dark-state spectroscopy. Nature, 459(7250):1105–1109, 2009.

[72] D. R. McCamey, J. Van Tol, G. W. Morley, and C. Boehme. Electronic spin storage in an electrically readable nuclear spin memory with a lifetime¿ 100 seconds. Science, 330 (6011):1652–1656, 2010.

[73] M. J. R. Hoch, J. Lu, P. L. Kuhns, W. G. Moulton, and A. P. Reyes. Current-induced dynamic nuclear polarization in GaAs. Phys. Rev. B, 72:233204, Dec 2005. doi: 10.1103/PhysRevB.72.233204. URL http://link.aps.org/doi/10.1103/PhysRevB.72.233204.

[74] Gurneet Kaur and G. Denninger. Dynamic nuclear polarization in iiiv semiconductors. Applied Magnetic Resonance, 39(1-2):185–204, 2010. ISSN 0937-9347. doi: 10.1007/s00723-010-0155-7. URL http://dx.doi.org/10.1007/s00723-010-0155-7.

[75] C. J. Trowbridge, B. M. Norman, Y. K. Kato, D. D. Awschalom, and V. Sih. Dynamic nuclear polarization from current-induced electron spin polarization. Phys. Rev. B, 90:085122, Aug 2014. doi: 10.1103/PhysRevB.90.085122. URL http://link.aps.org/doi/10.1103/PhysRevB.90.085122.

[76] Pramila Raghavan. Table of nuclear moments. Atomic Data and Nuclear Data Tables, 42(2):189 – 291, 1989. ISSN 0092-640X. doi: http://dx.doi.org/10.1016/0092-640X(89)90008-9. URL http://www.sciencedirect.com/science/article/pii/0092640X89900089.

[77] R. I. Dzhioev and V. L. Korenev. Stabilization of the electron-nuclear spin orientation in quantum dots by the nuclear quadrupole interaction. Phys. Rev. Lett., 99:037401, Jul 2007. doi: 10.1103/PhysRevLett.99.037401. URL http://link.aps.org/doi/10.1103/PhysRevLett.99.037401.

[78] A. Abragam and M. Goldman. Principles of dynamic nuclear polarisation. Reports on Progress in Physics, 41(3):395, 1978. URL http://stacks.iop.org/0034-4885/41/i=3/a=002.

[79] S. T. Goertz. The dynamic nuclear polarization process. Nuclear Instruments and Methods in Physics Research Section A: Accelerators, Spectrometers, Detectors and Associated Equipment, 526(12):28 – 42, 2004. ISSN 0168-9002. doi: http://dx.doi.org/10.1016/j.nima.2004.03.147. URL http://www.sciencedirect.com/science/article/pii/S0168900204005546. Proceedings of the ninth International Workshop on Polarized Solid Targets and Techniques.

[80] Mikhail I. Dyakonov, editor. Spin Physics in Semiconductors. Springer-Verlag, 2008.

[81] N. Bloembergen. Nuclear magnetic relaxation in semiconductors. Physica, 20(712):1130 – 1133, 1954. ISSN 0031-8914. doi: http://dx.doi.org/10.1016/S0031-8914(54)80253-9. URL http://www.sciencedirect.com/science/article/pii/S0031891454802539.

[82] N. Bloembergen, E. M. Purcell, and R. V. Pound. Relaxation effects in nuclear magnetic resonance absorption. Phys. Rev., 73:679–712, Apr 1948. doi: 10.1103/PhysRev.73.679. URL http://link.aps.org/doi/10.1103/PhysRev.73.679.

[83] Daniel Paget. Optical detection of nmr in high-purity gaas: Direct study of the relaxation of nuclei close to shallow donors. Phys. Rev. B, 25:4444–4451, Apr 1982. doi: 10.1103/PhysRevB.25.4444. URL http://link.aps.org/doi/10.1103/PhysRevB.25.4444.

[84] L. Meier, G. Salis, I. Shorubalko, E. Gini, S. Schön, and K. Enssling. Measurement of rashba and dresselhaus spin-orbit magnetic fields. Nat. Phys., 3:650–654, 2007.

[85] B. M. Norman, C. J. Trowbridge, J. Stephens, A. C. Gossard, D. D. Awschalom, and V. Sih. Mapping spin-orbit splitting in strained (in,ga)as epilayers. Phys. Rev. B, 82:081304, Aug 2010. doi: 10.1103/PhysRevB.82.081304. URL http://link.aps.org/doi/10.1103/PhysRevB.82.081304.

[86] G. Salis, D. T. Fuchs, J. M. Kikkawa, D. D. Awschalom, Y. Ohno, and H. Ohno. Optical manipulation of nuclear spin by a two-dimensional electron gas. Phys. Rev. Lett., 86:2677–2680, Mar 2001. doi: 10.1103/PhysRevLett.86.2677. URL http://link.aps.org/doi/10.1103/PhysRevLett.86.2677.

[87] G. Feher. Nuclear polarization via "hot" conduction electrons. Phys. Rev. Lett., 3:135–137, Aug 1959. doi: 10.1103/PhysRevLett.3.135. URL http://link.aps.org/doi/10.1103/PhysRevLett.3.135.

[88] R. O. Carlson, G. A. Slack, and S. J. Silverman. Thermal conductivity of gaas and gaas1xpx laser semiconductors. Journal of Applied Physics, 36(2):505–507, 1965. doi: http://dx.doi.org/10.1063/1.1714018. URL http://scitation.aip.org/content/aip/journal/jap/36/2/10.1063/1.1714018.

[89] Christopher J. Trowbridge and Vanessa Sih. Phase effects due to previous pulses in time-resolved faraday rotation measurements. Journal of Applied Physics, 117(6):063906, 2015. doi: http://dx.doi.org/10.1063/1.4907912. URL http://scitation.aip.org/content/aip/journal/jap/117/6/10.1063/1.4907912.

[90] Marcus Heidkamp. Spin-Coherence and -Dephasing of Donor and Free Conduction Band Electrons across the Metal-Insulator Transition in Si:GaAs. PhD thesis, Technischen Hochschule Aachen, 2004.

[91] Sebastian Kuhlen, Ralph Ledesch, Robin de Winter, Matthias Althammer, Sebastian T. B. Gnnenwein, Matthias Opel, Rudolf Gross, Thomas A. Wassner, Martin S.

Brandt, and Bernd Beschoten. Unambiguous determination of spin dephasing times in zno by time-resolved magneto-optical pumpprobe experiments. physica status solidi (b), 251(9):1861–1871, 2014. ISSN 1521-3951. doi: 10.1002/pssb.201350201. URL http://dx.doi.org/10.1002/pssb.201350201.

[92] Y. Qi and S. Zhang. Spin diffusion at finite electric and magnetic fields. Phys. Rev. B, 67:052407, Feb 2003. doi: 10.1103/PhysRevB.67.052407. URL http://link.aps.org/doi/10.1103/PhysRevB.67.052407.

[93] Z. G. Yu and M. E. Flatté. Electric-field dependent spin diffusion and spin injection into semiconductors. Phys. Rev. B, 66:201202, Nov 2002. doi: 10.1103/PhysRevB.66.201202. URL http://link.aps.org/doi/10.1103/PhysRevB.66.201202.

[94] Bruce R. Kusse and Erik A. Westwig. Mathematical Physics. Wiley-VCH Verlag, 2^{nd} edition, 2006.

[95] A. Einstein. Über die von der molekularkinetischen theorie der wärme geforderte bewegung von in ruhenden flüssigkeiten suspendierten teilchen. Annalen der Physik, 322(8):549–560, 1905. ISSN 1521-3889. doi: 10.1002/andp.19053220806. URL http://dx.doi.org/10.1002/andp.19053220806.

[96] M. von Smoluchowski. Zur kinetischen theorie der brownschen molekularbewegung und der suspensionen. Annalen der Physik, 326(14):756–780, 1906. ISSN 1521-3889. doi: 10.1002/andp.19063261405. URL http://dx.doi.org/10.1002/andp.19063261405.